# $\tau$ Leptons at HERA

**DISSERTATION**

zur Erlangung des Doktorgrades
des Fachbereichs Physik
der Universität Hamburg

vorgelegt von

**Damir Lelas**
aus Omiš

Hamburg
April 2004

| | |
|---|---|
| Gutachter der Dissertation: | Prof. Dr. P. Schleper<br>Prof. Dr. R. Klanner |
| Gutachter der Disputation: | Prof. Dr. R.-D. Heuer<br>Prof. Dr. P. Schleper |
| Datum der Disputation: | 11. Juni 2004 |
| Vorsitzender des Prüfungsausschusses: | Dr. H.-D. Rüter |
| Vorsitzender des Promotionsausschusses: | Prof. Dr. R. Wiesendanger |
| Dekan des Fachbereichs Physik: | Prof. Dr. G. Huber |

To my Family

## ACKNOWLEDGMENTS

A tremendous effort and dedication of thousands of people involved in the development, construction and maintenance of the HERA accelerator and the ZEUS experiment, made the analysis in this thesis possible. I would like to thank them. Specially, I would like to express my gratitude to all people I have had privilege to collaborate with.

I am thankful to Prof. Robert Klanner who gave me the opportunity to work within the ZEUS Collaboration at DESY. My deepest thanks to Prof. Peter Schleper and Dr. Tancredi Carli for their guidance, support, everlasting enthusiasm and profound physical insights, i.e. for being most inspiring mentors. Prof. Schleper took additional burden of correcting the drafts of the thesis and Dr. Carli's enthusiasm and help were always there, even after he moved to Geneva, many thanks.

It was a great pleasure to work within the ZEUS Collaboration and I am quite sure that people will forgive me not mentioning their titles. The exotics, since recently high-$Q^2$, physics group was the most pleasant and helpful collaborating environment. Many thanks to Elisabetta Gallo for her devotion and advice, as well as Lorenzo Bellagamba, Bruce Straub, Katarzyna Klimek, Enrico Tassi, Alex Tapper and all other members of the high-$Q^2$ group.
I am grateful to Rik Yoshida for his support.

I am very thankful to my "tau"-colleagues Dominik Dannheim and Chi-Nhan Nguyen. Their work and engagement were precious and inspiring to me.
In addition, I would like to thank Prof. Maria Krawczyk for her valuable comments and explanations of theoretical aspects of possible Light Higgs production at HERA.

The work on the C5 counter was always special to me and mostly because of my C5 colleagues. I would like to thank Julia Fourletova for fruitful and efficient collaboration, as well as Chris Youngman, Wladimir Hain, Ulrich Kötz, James Crittenden, Alessandro Polini, Uwe Schneekloth and Wojtek Ruchlewicz.

Always friendly and supportive atmosphere within DESY, ZEUS and Hamburg University group was inspiring and relaxing. I am thankful to my colleagues Oliver Gutsche, Liz Nuncio-Quiroz, Volker Adler, Chi-Nhan Nguyen, Amita Raval, Raquel Santamarta, Dominik Dannheim, Ingo Bloch, Benjamin Kahle, Florian Göbel, Margherita Milite, Ulrich Fricke, Stefan Stonjek, Sonja Hillert, Harald Labes, Amaya López-Durán Vianni, Matthias Moritz, Ignacio Redondo, Oscar Gonzalez, Manuel Zambrana, Vincenzo Chiochia, Jörg Stahl, Devis Contarato, Andreas Schramm, Claus Horn, Mark Sutton, Tim Namsoo, Nicola Coppola, Silvia Miglioranzi, Alessandro Montanari, Mayuko Kataoka, Detlef Bartsch, Eileen Heaphy, Xiang Liu and Heuijin Lim.

My special thanks go to my colleagues and friends Arafat Gabareen-Mokhtar, Dorian Kçira, Mónica Vázquez, John Loizides, James Ferrando, Erik Maddox and Gregor Kramberger. Thanks to Karl-Dieter Schaller for his great company.

Of course, all my friends outside DESY and Germany deserve my deepest gratitude, as they very well know.

At the end, it is needless to specially stress that everything achieved was possible only because of love, devotion and sacrifice of my family.

**ABSTRACT**

This thesis describes a generic search for events containing $\tau$ leptons in $e^{\pm}p$ collisions at HERA using the ZEUS detector. A multi-observable discrimination technique was used, exploiting the internal jet structure to discriminate between pencil-like jets coming from hadronic $\tau$ decays and quark- or gluon-induced jets.

In a search for events containing isolated $\tau$ leptons and large missing transverse momentum, two candidate events with a transverse momentum of the hadronic system $p_T^{had} > 25\ GeV$ have been observed, while $0.20 \pm 0.05$ events were expected from Standard Model processes.

To verify the $\tau$ discrimination technique and to explore the feasibility of tagging $\tau$ pair events at HERA, a di-$\tau$ study was performed. 14 data events were selected while the expected number of di-$\tau$ signal events was $10.38 \pm 0.13$ for an expectation of $1.12 \pm 0.85$ events from multi-electron and di-muon production.

A study of the perspectives for light Higgs boson search at HERA has been performed using MC simulations. The perspectives for a search in the channel $gg \to h \to \tau^+\tau^-$ were found to be not very promising, due to the properties of the underlying event.

## ZUSAMMENFASSUNG


Diese Dissertation beschreibt eine generelle Suche nach Ereignissen mit $\tau$-Leptonen mit dem ZEUS Detektor in $e^{\pm}p$-Kollisionen bei HERA. Zur Unterscheidung zwischen kollimierten Jets von hadronischen $\tau$-Zerfällen und Quark- oder Gluon-Jets wurde eine Multi-Observablen-Diskriminator Technik benutzt, welche die innere Jet-Struktur ausnutzt.

In einer Suche nach Ereignissen die ein isoliertes $\tau$-Lepton enthalten und einen hohen fehlenden Transversal-Impuls vorweisen, wurden zwei Kandidaten mit einem Transversal-Impuls des hadronischen Systems $p_T^{had} > 25\ GeV$ beobachtet, wohingegen $0.20 \pm 0.05$ Ereignisse von Standard-Modell-Prozessen erwartet werden.

Zur Überprüfung der $\tau$-Diskriminator-Technik wurden Ereignisse mit $\tau$-Paaren untersucht. Es wurden 14 Daten-Ereignisse selektiert, wobei $10.38 \pm 0.13$ Di-$\tau$-Ereignisse bei $1.12 \pm 0.85$ Ereignissen aus Multi-Elektron- und Di-$\mu$-Produktion erwartet werden.

Eine Studie der Perspektiven der Suche nach einem leichten Higgs-Boson bei HERA wurde unter Zuhilfenahme von MC-Simulationen durchgeführt. Die Perspektiven für eine Suche im Kanal $gg \rightarrow h \rightarrow \tau^+\tau^-$ wurden aufgrund der Eigenschaften zusätzlicher weicher hadronischer Wechselwirkungen in den Ereignissen als nicht sehr vielversprechend eingestuft.

# TABLE OF CONTENTS

## LIST OF TABLES

## LIST OF FIGURES

# CHAPTER 1
# INTRODUCTION

To know what is the essence of the world (if you like the universe) is an everlasting human desire. Physics, in it's own way, tries to follow that old desire and even wants to quantify how well we know the things.

Nowadays, in the physical picture of the world everything is made of two types of "elementary" particles: *quarks* and *leptons*, and their corresponding antiparticles. Quarks and leptons interact with each other via gravitational, electromagnetic and weak interactions, while the strong interaction occur among quarks, exclusively, which is the main difference between quarks and leptons. The language used to describe particles and their interactions is *Quantum Field Theory* (QFT). Where, both, particles and interactions are described as quanta of associated fields. QFT is the basis of *the Standard Model* (SM), the theory which is largely successful in description of particles interacting electromagnetically, weakly and strongly. The known "elementary" particles are shown in Fig 1.1, together with force quanta (carriers). The electromagnetic force carrier is called *photon* ($\gamma$), the strong force carriers are *eight gluons* ($g$) and the weak force quanta are ($W^{\pm}$ and $Z^0$) bosons[1].

The SM was (is) thoroughly tested in numerous experiments and is seen to describe and predict an impressively large spectrum of measurements. However, the SM cannot be the final theory for a very simple reason: it does not contain gravity, the oldest known interaction. But, recent measurements suggest that the SM has to be revised even in it's own domain of description. Namely, findings that the neutrinos have a small but finite mass [1, 2] implies the existence of right-handed neutrinos, indicating the need for changes to the chiral properties of the SM. The other hints that do not seem to fit in the theory come from astrophysics. The dynamics of the galaxies and universe itself indicates that most of the matter in the universe is of an unknown nature, *the dark matter.* Even more puzzling, astrophysical measurements suggest the existence of mysterious uniformly-distributed energy across the universe, so called *dark energy.* One of the common ideas is that dark matter and may be even dark energy are composed of unknown particles and fields predicted by theories and models which go beyond the Standard Model.

The impact of present and future particle accelerators could give crucial hints how to proceed beyond our present understanding of nature.

[1]Bosons are particles with integer spins. All force quanta are *bosons*, while all matter particles are *fermions.* The fermions have half-integer spins.

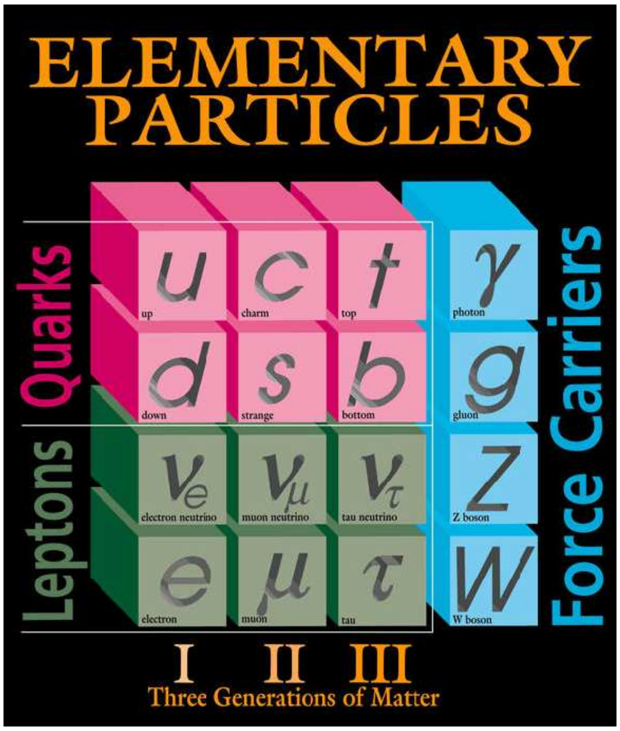


Figure 1.1: The "elementary" particles and force carriers except gravity

This thesis focusses on a search for possible deviations from the small rates of SM processes involving $\tau$ leptons at the HERA (*Hadron Elektron Ring Anlage*) accelerator and is performed within the ZEUS Collaboration. To measure processes with $\tau$ leptons is a challenge even for the SM predicted production mechanisms, but possible observation of deviations from the SM could be striking, already for small event rates detected.
Here a measurement of $\tau$ leptons is presented in two channels:

- a single (isolated) $\tau$ in events with large missing transverse momentum
- di-$\tau$ events

High transverse momentum leptons in events with large missing transverse momentum are remarkable signatures and very rare in the Standard Model. The only significant SM process as source for such events is a single W-boson production ($\sigma \sim 1\ pb$) followed by leptonic decays of the W boson. Both HERA colliding experiments, H1 and ZEUS, have searched for such signatures in the $e$- and $\mu$- channel [3, 5]. The H1 experiment results show an excess in observed events compared to the SM prediction, while the ZEUS finding is in agreement with the SM expectation. The analysis presented here extends the ZEUS search to the $\tau$ channel.

Lepton pair production at HERA proceeds mainly via two-photon interactions, $\gamma\gamma \rightarrow l^+l^-$, where the photons come from the radiation of beam particles. An accurate SM prediction and clean experimental signature make the search for possible non-SM multi-lepton production mechanisms very attractive. In the dimuon channel, H1 and ZEUS results are in agreement with the SM expectation [7, 8], while in the multi-electron channel the H1 observation exceeds theoretical prediction [9] and the ZEUS finding is consistent with the SM [8], for the large invariant mass region ($M > 100\ GeV$). This work exploits possibility for a multi-$\tau$ observations in the ZEUS experiment.

The only undetected fundamental particle of the SM is the *Higgs boson*, particle connected with the origin of mass. The combined results of the *Large Electron Positron* (LEP) collider at CERN have excluded masses of the SM Higgs below 114.4 $GeV$ at the 95% confidence level [10]. Because of the LEP limit, a search for the SM Higgs boson at HERA is not promising, as the production cross-section is way too small. The minimal extension of the SM in the Higgs sector is to include another complex scalar field in the symmetry breaking mechanism (Higgs mechanism). The resulting *Two Higgs Doublets Model* (2HDM) [11] allows the existence of the Light Higgs boson beyond present experimental limits [12]. Within the 2HDM the predicted Higgs production cross section varies from $\sim$ 40-50 $pb$ to $\sim$ 1 $pb$ for Higgs masses between 5 and 25 $GeV$ [13]. The dominant Higgs decay mode below 10 $GeV$ is $h \rightarrow \tau\tau$, while for the Higgs masses above 10 $GeV$ b-quark decays of the Higgs take over, but $h \rightarrow \tau\tau$ contribution is still sizable, around 10%. This thesis presents a study of the perspectives for the Light Higgs boson search at HERA via the $h \rightarrow \tau\tau$ decay channel.

# CHAPTER 2
# BASICS OF THE LEPTON-NUCLEON SCATTERING

To understand the structure of hadrons, particles composed of quarks and gluons is a great challenge, with until now many open questions. The HERA collider is a place almost fully dedicated to address this issue.

Although the subject of the thesis is not directly devoted to the structure of hadrons, this chapter contains a very brief flash through that amazing topic, as well as some basic concepts of electron-proton scattering and HERA physics. Understanding of hadron interactions is however required to understand production mechanisms and background for this analysis.

## 2.1 Lepton-nucleon scattering

In the most general case lepton-nucleon interaction proceeds via the exange of a force quanta ($\gamma, Z^0, W^{\pm}$, the gravity is ignored). But, as far as nucleon structure is concerned, it is sufficiently instructive to see what is going on in the case of electromagnetic interaction ($\gamma$ exchange). Leptons are assumed to be structureless elementary particles.

Concerning the proton faith there are only two possibilities as outcome of the electron[1]-proton interaction. The interaction can be either *elastic* when the proton is just recoiled, or *inelastic*, when the proton is broken up and there are more hadronic particles in the final state, see Fig 2.1.

In the Quantum Mechanical picture of the electromagnetic electron-proton interaction, the cross section can be written for, both, elastic and inelastic case straight away:

$$\frac{d\sigma^{el.}}{dq^2dx} \sim \frac{\alpha_{em}^2}{q^4} F_{el.}^2(q^2) \cdot \delta(1-x) \tag{2.1}$$

$$\frac{d\sigma^{inel.}}{dq^2dx} \sim \frac{\alpha_{em}^2}{q^4} F_{inel.}^2(q^2, x) \tag{2.2}$$

There are only two terms in each equation. The term $\alpha_{em}^2/q^4$ is nothing more than a point-like, so called *Rutherford cross section*, as if the proton would be point-like, i.e. elementary particle. The other term $F_{el.,inel.}$ is *Proton Form Factor* which describes spatial charge distribution in the proton, if proton is a composite

[1]Here and in the following, the term 'electron' denotes generically both the electron ($e^-$) and the positron ($e^+$).

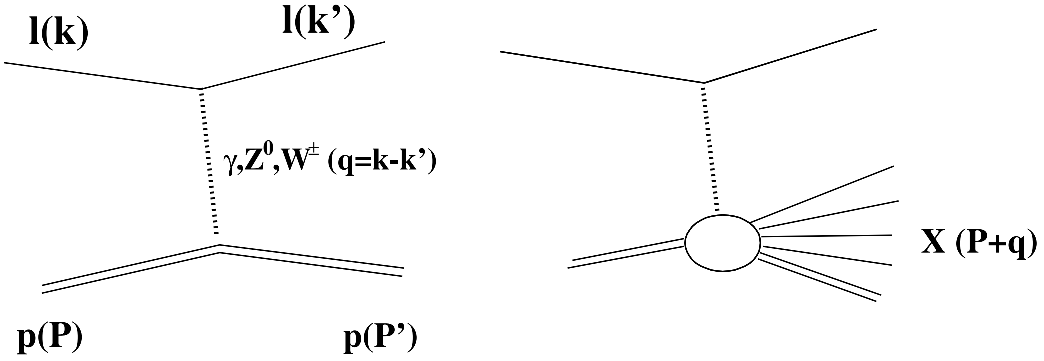


Figure 2.1: Schematic diagram describing *elastic* and *inelastic* lepton-nucleon scattering. The four momenta of the particles, or particle systems, are given in parentheses.

object. The variable $q^2$ is the *square of the four momentum transfer*, determines the hardness of the interaction, or in other words, the resolving power of the interaction. The variable $x$ specifies an inelastic break up of the proton (will be defined in the next section), $\alpha_{em}$ is an electromagnetic coupling proportional to the elementary charge. The delta function $\delta(1-x)$ makes the two equations equivalent.

It is obvious that the behaviour of the cross section is determined directly by the proton structure itself.

The outcome of numerous experiments performed since the late 1960s till nowadays is astonishing. Namely, the elastic cross section falls steeply with $|q^2|$ and the inelastic cross section stays large even for the highest value of $|q^2|$, but it is dependent on the $|q^2|$ value. In other words, the proton is completely destroyed even after small "scratch" of $|q^2| \sim 1\ GeV^2$ (the proton mass is 0.938 $GeV$) is applied. In adition, it is undoubtedly established that there are constituents inside the proton.

The only picture of the proton which is in agreement with the findings [14] says that there are constituents inside the proton, but they are not strongly bound together, neither at the small distances (highest $|q^2|$) nor on scales comparable to the whole proton size ($|q^2| \sim 1\ GeV^2$). In the standard prescription a perturbation expansion in terms of the strong running coupling constant, $\alpha_s(|q|^2)$, is used to calculate scattering amplitudes of the hard interaction. At high $|q^2| \gg 0$, $\alpha_s$ is small and it is sufficient to consider first few terms in the perturbative expansion. At the low $|q^2|$ (few $GeV^2$), the effective coupling becomes large and perturbative approach is not valid any more. However, as argued by Gribov and Dokshitzer [14, 15] and is suported by experimental findings [17], it should be possible to obtain a coherent description of the low $|q^2|$ region without breakdown of perturbative theory. The perturbative approach supported by consistent description of the vacuum could be applicable even in so called "non-perturbative" regime [14, 15].

The constituents of the proton have never been detected as free particles outside the proton and other hadrons.

Having all this in mind, there is an unavoidable and fundamental question: *Why are the quarks confined inside the proton, or if one likes, why is the proton bound object*!? There is no answer to this absolutely essential question till the present day.

However, if there is no final answer it only means the subject is amazingly tricky and evolved, and significant progress has made in the understanding of the structure of hadrons.

### 2.1.1 Kinematics

As it is shown in Fig. 2.1, $k, k', P, P'$ are the four momenta of the initial and final lepton, of the incoming nucleon and of the outgoing hadronic system, respectively, while the four momentum transfer is $q = k - k'$. Fixed by the incoming momenta, the *centre-of-mass energy squared* is defined as:

$$s = (k + P)^2$$

However, an energy variable more appropriate at HERA is *centre-of-mass energy squared of the force quantum nucleon system*, or, in other words, an *invariant mass of the hadronic final state*, defined as:

$$W^2 = (q + P)^2$$

As had been shown, the cross section depends on only two kinematical variables, $q^2$ and $x$:

$$Q^2 = -q^2 = -q^\mu q_\mu,$$

$$\mathbf{x} = \frac{\mathbf{Q^2}}{\mathbf{2P \cdot q}} = \frac{Q^2}{Q^2 + W^2 - M_p^2} \Longrightarrow \mathbf{W^2} - \mathbf{M_p^2} = \frac{\mathbf{1 - x}}{\mathbf{x}}\mathbf{Q^2} \geq \mathbf{0} \Longrightarrow 0 \leq x \leq 1.$$

The square of the four momentum transfer is always negative (for space-like particles which exist only inside the limits of Heisenberg's Uncertainty Principle), so the positive variable $Q^2$ has been introduced. From the expresion above it is clear why the dimensionless variable $x$, so called *Bjorken's x*, describes an inelastic break up of the proton, $M_p$ is just the proton mass.

The HERA data cover a $Q^2$ region up to $\sim 40000\ GeV^2$, corresponding to a resolvable distance of $\lambda \approx \hbar c/\sqrt{Q^2} = 10^{-18}\ m$, which is 1/1000 of the proton radius.

## 2.2 The Quark Parton Model, scaling and non-scaling

To construct a consistent theory of electron-proton scattering one has to employ the knowledge of Quantum Field Theory to describe creation and annihilation of quarks and gluons. The formalism is more evolved, but the picture stays the same. There is, again, elastic cross section for the interaction of structureless, point-like, particles and inelastic cross section handled by using the inelastic form factors (the *Proton Structure Functions*), once more.

The sign that there are structureless particles inside a complex system like a proton lays in the fact that for small wavelenghts of the probe (large $Q^2$), the proton suddenly starts behaving like a set of independent free Dirac particles (*quarks*). In that case, at large $Q^2$, inelastic electron-proton scattering is viewed simply as elastic scattering of the electron on a "free" quark within the proton. Intriguing property is that the inelastic structure functions are independent of $Q^2$, at a given value of $x$. This is equivalent to the behaviour of the cross section for large momentum transfer in the Rutherford experiment, which reveals the "point" charge of the nucleus in the atom. The data from the *Stanford Linear Accelerator* (SLAC) has shown that measured proton structure functions are independent of $Q^2$, at given value of $x \approx 0.25$, revealing the fact that the photon is indeed interacting with point-like particles. This behaviour of the structure function is called *scaling*.

Although this was the proof of the existence of the quarks inside the proton, the very idea of the constituents of the proton is quite older and comes from attempts to solve the quantum number problems in the spectroscopy of hadrons. A study of the quantum numbers of these partons allows us to identify them with "original" quarks introduced in the study of the hadron spectrum.

In the *Quark Parton Model* (QPM) the electron-proton interaction is described as an incoherent sum of contributions from individual free quarks. But, how is it possible to justify such picture? Namely, although the results from HERA experiments [17] point out that constituents of the proton never interact strongly with each other, they do interact on the scales comparable to the proton size. Moreover, the lifetimes of the partons in the proton rest frame are approximately equal to the vacuum fluctuations time, so we can talk only about fluctuations, not about free particles, in the proton rest frame.

But, if we go, via Lorentz boost, to the *Proton Infinite Momentum Frame*, the frame in which the proton longitudinal momentum is much larger than its mass ($P_z \gg M_p$), the picture changes dramatically. It is best seen in the *Breit (or brick wall) frame* in which the quark and the virtual (space-like) photon collides head-on. The interaction time may be defined as the overlap time between the quark and the field of the photon, $t_{int.} \sim 2m_q/Q^2$, where $m_q$ stands for some effective mass of the quark [16]. The lifetime of the quark is then estimated to be $t_q \sim \sqrt{Q^2}/m_q^2$, much larger than the interaction time $t_{int.}$. Thus at large $Q^2$, it is indeed justified to consider the quark as free and to neglect possible interactions of the photon with other partons.

The interpretation of the variable $x$ defined in the previous section is specially interesting in the QPM. It is easy to show that the variable $x$ is the fraction of the proton momentum carried by the struck massless quark.

### 2.2.1 Where are the gluons?

If we sum over the momenta of all partons, we must reconstruct the total momentum $P$ of the proton. The data obtained from the measurements of the proton and neutron structure functions show that the contribution from the charged partons, quarks, is only $\approx 50\%$ of the total proton momentum. Hence, about 50% of the proton momentum is carried by electromagnetically neutral particles.

As has been mentioned, at the basis of the coherent description of the electron-proton interaction is Quantum Field Theory. So, there should exist a particle which is the quantum of the interaction under study. It is obvious that quarks must interact with each other with an additional interaction called the strong interaction, to overcome an electromagnetic repulsion between them inside the proton. The quanta of the strong interaction are called *gluons* and the charge of the strong interaction is called *colour charge*. The proper field theory of strong interaction is *Quantum Chromodynamics* (QCD).

It is tempting to identify the neutral partons with gluons, but is this identification justified?

The QPM approach completely ignores the dynamical role of gluons as the carriers of the strong force associated with coloured quarks. It was neglected that the quark may radiate a gluon before or after being struck by the virtual photon.

It is clearly crucial to check that the gluons can indeed be identified with the neutral partons, and subsequently try to probe the dynamical properties of QCD. As it will be described in the next section, one of the consequences of inclusion of the dynamical properties will be the *scaling violation, or non-scaling.*

## 2.3 QCD evolution equations

An inclusion of the dynamics of the partons (quarks and gluons) will affect the picture of large $Q^2$ electron-proton scattering drastically. Quark-gluon colour theory allows precise predictions of dynamical effects on the behaviour of the proton structure functions. Figure 2.2 shows one of the most striking HERA plots, the scaling violation of the proton structure function $F_2$ [21], which in the QPM describes quark distributions inside the proton, for an impressive range of $Q^2$ and $x$ values. The QCD prediction clearly describes the data trend.

Due to the QCD radiation, the number of small $x$ partons increases and for the same reason the number of large $x$ partons decreases, with the resolving power $Q^2$.

From Fig. 2.2 it is obvious how deservedly lucky SLAC pioneers were, measuring in the "proper" region of $x \approx 0.25$, where scaling can be seen. Otherwise the QCD development would have been much more difficult.

The parton distributions in the hadron cannot be calculated from first principles of QCD. As mentioned in the first section of the chapter, there is still lack of understanding why the hadrons are colourless objects, but there is no doubt that QCD is the correct theory of the colour interaction. In other words, it is, more or less, known how to deal with the quarks and gluons at short distances, but it is unknown how they are organised in the colourless hadrons.

However, the *Factorisation Theorem* (Collins et al., 1985) allows to separate the long range effects (such as parton distribution at small $Q^2$) from the short range interaction (calculable high $Q^2$ region). The main reason why the factorisation is possible comes from the fact that short and long range interactions are well separated in time, so it is possible, somehow, to disentangle each contribution.

Using the factorisation theorem, the proton structure function $F_2$ can be written as:

$$F_2(x, Q^2) = \int_x^1 dx' f(x', \mu_F^2) \hat{\sigma}(\frac{x}{x'}, Q^2, \mu_F^2) \tag{2.3}$$

where $f(x', \mu_F^2)$ is the probability to find a quark with momentum fraction $x'$ in the proton and $\hat{\sigma}(\frac{x}{x'}, Q^2, \mu_F^2)$ is the reduced cross section for the elastic quark-photon scattering in the form equivalent to the structure function [22], for the

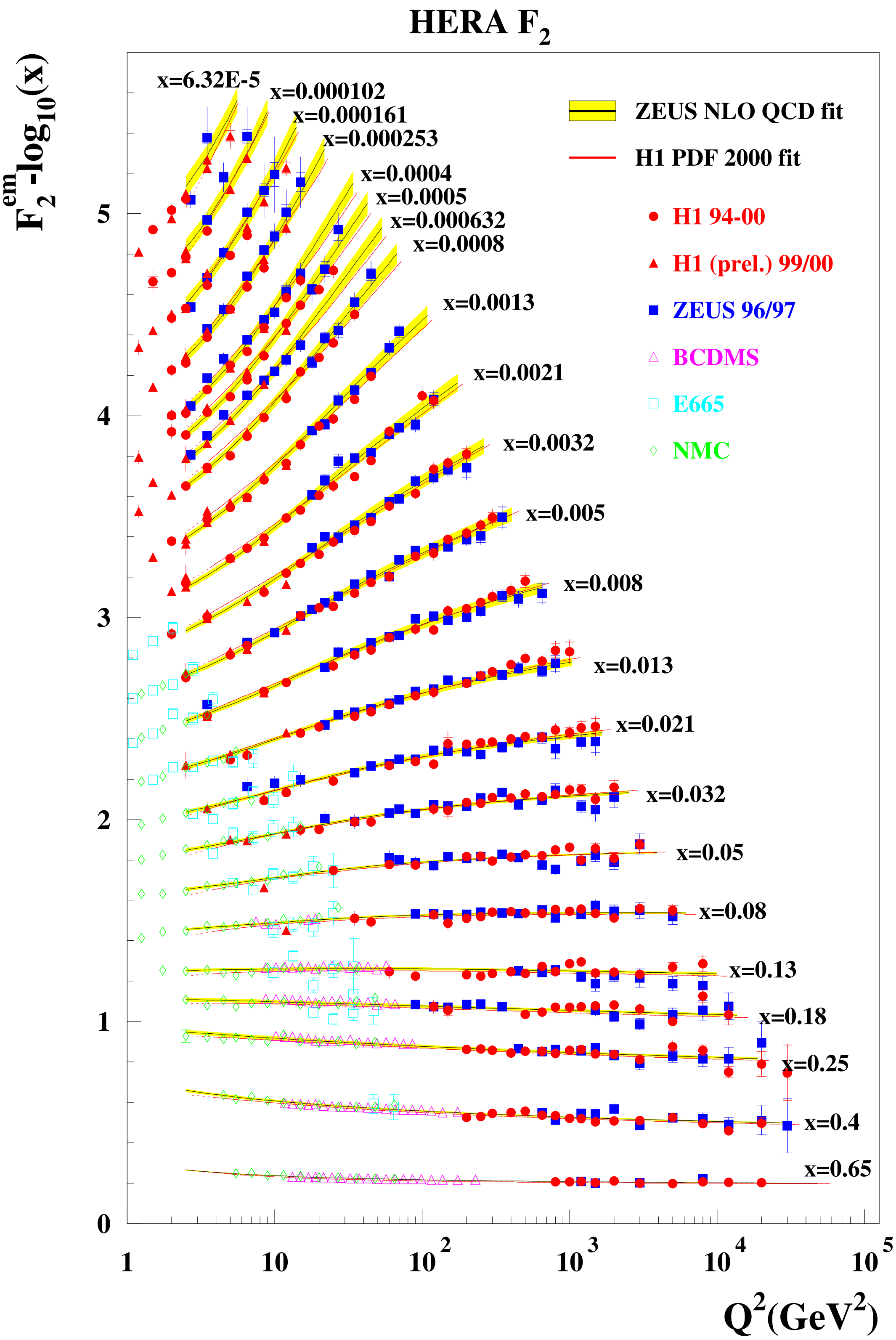


Figure 2.2: Measurements of the structure function $F_2$ as a function of $Q^2$ for different values of $x$. The measurements at different values of $x$ have been scaled by constant factors for display purposes. The QCD evolution of the structure functions through the DGLAP equations are given, as well.

photon resolution power $Q^2$. The QCD radiation can lower the quark momentum fraction from $x'$ to $x$, therefore all contributions have to be summed up. All the ignorance had been pumped up into, so called, *parton density function* $f$ (PDF). The factorisation scale $\mu_F$ shows the place of the cut between the short and long range contributions. The physical observable $F_2$ is, of course, independent of $\mu_F$.

The way to proceed is to have an input from the experimentally measured $F_2$ and get PDFs at particular value of $Q^2$, and then try to evolve them to another value of $x$ and $Q^2$ using the QCD knowledge. The factorisation theorem says that PDFs are process independent quantities. Once determined for a given process, PDFs can be used to make predictions for other processes. Figure 2.3 shows the PDFs extracted from a ZEUS QCD analysis of large $Q^2$ data [18]. As can be seen, the $u$ and $d$ valence quark (constituent quarks of the proton) densities dominate at large $x$ values, while sea quarks (results of gluon splittings, and the gluons beeing radiated from quarks) and gluons dominate at small values of $x$.

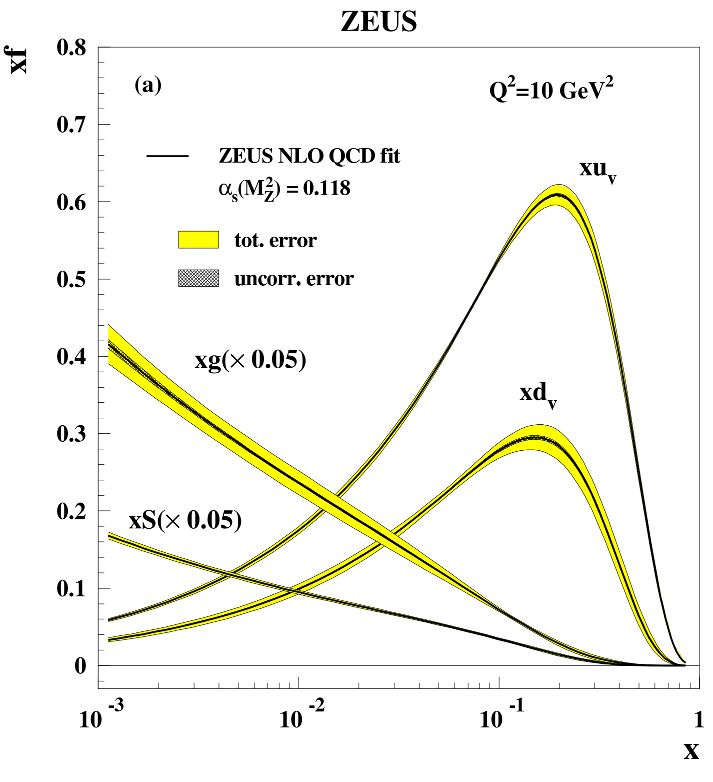


Figure 2.3: The gluon, sea, and valence PDFs extracted from the ZEUS NLO QCD fit ($Q^2 = 10\ GeV^2$).

To calculate an evolution of the PDFs on the basis of the factorization theorem, the *Dokshitzer Gribov Lipatov Altarelli Parisi* (DGLAP) evolution equations

[19] are used. For the small $x$ evolution, the *Balitzki Fadin Kuraev Lipatov* (BFKL) evolution equation [20] is more suitable. The detailed description is beyond the scope of this thesis.

So far, the fact that partons of the proton do not, practically, interact at short distances and start to interact only on the distances comparable to the size of the proton, has been taken as the experimental fact. But, how is it possible to explain that partons do not interact at small distances and do interact at larger scale? This effect, known as *asymptotic freedom* comes from the special property of the gluons. Namely, gluons interact not only with quarks, but with each other. When this exclusive property of QCD is fully taken into account, the result is asymptotic freedom at small distances (large momentum transfers).

## 2.4 Electron-proton scattering at HERA

If we exclude gravity, exchanged force quanta in the $e^{\pm}p$ scattering are $\gamma, Z^0$ and $W^{\pm}$, see Fig. 2.1. As was mentioned, a photon mediates an electromagnetic interactions, while $Z^0$ and $W^{\pm}$ are mediators of the weak force. According to the charge of an exchanged force quantum, the process is called *Neutral Current* (NC) ($\gamma, Z^0$ exchange) or *Charged Current* (CC) ($W^{\pm}$ exchange). In the CC process, an incoming lepton is transformed into associated neutrino, and outgoing neutrino escapes undetected.

A behaviour of the cross sections is governed by the fact that the photon is massless, while $Z^0$ and $W^{\pm}$ are massive particles ($M_W \approx 80\ GeV$, $M_Z \approx 91\ GeV$). Therefore, the exchange of massive mediators is suppressed by their masses and the cross section ratio is:

$$\frac{\sigma(Z, W^{\pm})}{\sigma(\gamma)} \sim \left(\frac{Q^2}{Q^2 + M^2_{Z,W^{\pm}}}\right)^2 \tag{2.4}$$

The signifficant weak effects can be expected only for large values of $Q^2$ ($\mathcal{O}(10^4\ GeV^2)$). Hence, the CC cross section is well suppresed compared to the NC cross section until $Q^2$ reaches values comparable to the $Z^0$ and $W^{\pm}$ masses. As can be seen in Fig 2.4, where single differential NC and CC cross sections as function of $Q^2$ obtained by H1 and ZEUS Collaborations are presented [21].

In addition, it is obvious that the CC cross section is larger for $e^-p$ than for $e^+p$ scattering, the reason being the larger $u$-quark component of the proton, which is relevant for $W^-$ exchange, while the smaller $d$-quark component is involved in

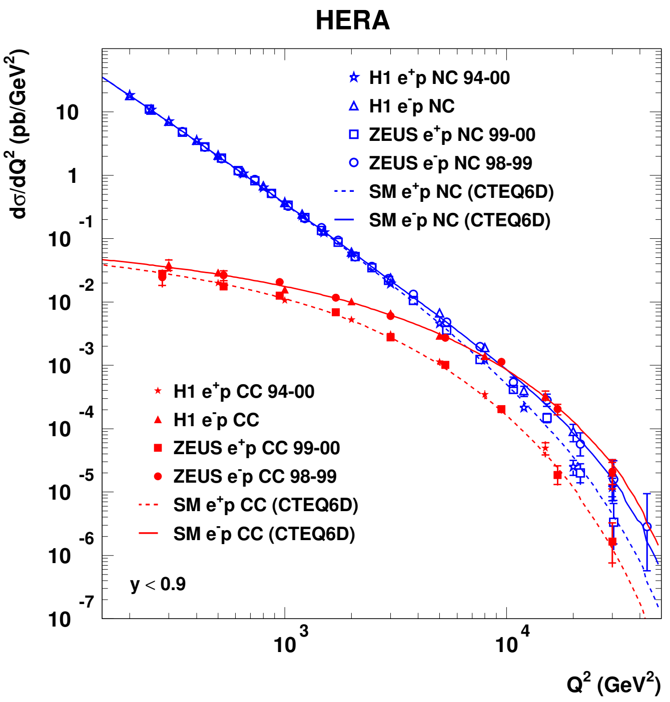


Figure 2.4: The single differential NC and CC cross sections as function of $Q^2$, obtained by H1 and ZEUS collaborations, for $e^-p$ and $e^+p$ scattering

$W^+$ exchange.

The NC current cross section at large $Q^2$ becomes larger, as well, for $e^-p$ than for $e^+p$ scattering. The reason being in the $\gamma Z^0$ interference term which reflects the special property of the electroweak theory that it does not conserve the parity (invariance under space inversion) and charge conjugation (invariance under particle-antiparticle exchange). The result is a positive interference for the $e^-p$ case, while destructive interference occurs in the $e^+p$ case and lowers the cross section value accordingly. The corresponding part of the proton struction functions is proportional to the difference between quark-antiquark density functions and can be determined from the difference between measured cross sections in $e^-p$ and $e^+p$ scattering case.

HERA is the first accelerator which offers the possibility to measure this part of the proton structure functions [22]. All previous measurements were done with the fixed target experiments at much lower values of $Q^2$.

### 2.4.1 Photoproduction and Deep Inelastic Scattering

The previously described classification of the HERA processes was based on the charge of exchanged force quantum (NC and CC), but even more common classification is made according to the *virtuality*, i.e. $Q^2$, of the exchanged force mediator.

It is clear from the above consideration that the major subject of interest is what happens at so called *proton vertex*, i.e. at the proton side of the $e^{\pm}p$ interaction. The role of the electron beam is simply that it is responsible for the presence of virtual force carriers and specially for the presence of virtual photons which dominate the small $Q^2$ region. Why do we call these particles virtual? The reason is that they exist only inside the limits of Heisenberg's Uncertainty Principle and their momentum transfer squared, $q^2$, is always negative (space-like particles). This was the reason for the convenient introduction of the positive variable $Q^2 = -q^2$ and larger $Q^2$ means larger virtuality, because for *real photons* $Q^2 = q^2 = 0$.

Once again, because of Heisenberg's Uncertainty Principle, there is a dramatic consequence on the nature of interactions depending on the actual virtuality of exchanged photon.

From Eq. 2.4 it is clear that cross section goes down with $Q^4$, therefore the main contribution comes from the small $Q^2$ region.

If $Q^2$ of the exchanged photon is around zero ($Q^2 \ll 1\ GeV^2$), the *photoproduction regime* (PhP), the photon is quasi-real therefore its virtuality is very small and there is enough time for the photon to fluctuate into, for example, quark-antiquark pair, acording to Uncertainty Principle and Special Relativity. This quark-antiquark pair can subsequently develop further structure and that structure interacts with a proton. In this case, the electron-proton scattering can then be viewed as hadron-hadron scattering.

The picture is dramatically different when photon virtuality is large, $Q^2 \gg 1\ GeV^2$, so called *Deep Inelastic scattering* (DIS). In DIS case the photon is highly virtual, i.e. it is, already, deeply "Heisenberg" particle, so the probability to acquire aditional structure is largely suppressed and the outcome is that photon interact as point-like particle. This photon then probes small distances inside the proton and resolves point-like quarks inside. However, if the energy of the photon (in the rest frame of the proton) is large enough, even highly virtual photon can acquire the structure, because the fluctuation probability rises with the photon energy!

Additional details of amazing lepton-nucleon scattering are beyond the scope of this thesis, and the specific signal processes considered in this study will be presented in more details in the corresponding chapters.

# CHAPTER 3
# HERA ACCELERATOR AND THE ZEUS DETECTOR

A tremendous effort and dedication of thousands of people involved in the development, construction and maintenance of the HERA accelerator and the ZEUS experiment, made the analysis in this thesis possible.

This chapter shortly describes HERA and the ZEUS detector. The components of ZEUS particularly relevant to this work are introduced in more detail. The ZEUS Trigger System and data acquisition are presented, as well.

## 3.1 HERA

HERA is the world largest microscope. Our knowledge and understanding increase with increasing resolution-power of a microscope. Because HERA works in a regime of Quantum Physics, the object size which can be resolved is determined by the momentum transfer of the probe. According to the Heisenberg's Uncertainty Principle, better resolution requires larger momentum transfer, i.e. higher energy involved. Due to another fundamental principle of the mass-energy equivalence, HERA can create new particles, as well as it can probe.

Located at DESY (*Deutsches Elektronen Synchrotron*, see Fig 3.1) in Hamburg, Germany, HERA is the first (could easily be the last) electron proton ($ep$) collider. Fig. 3.2 shows a schematic view of the HERA facility.

The construction was finished in the late 1990 and the first collisions were obtained in 1992. Both, electrons[1] and positrons can be brought into collisions with protons at zero colliding angle. For the data taking period from 1994-2000 studied in this analysis, the lepton beam energy was 27.5 $GeV$. The proton beam energy was 820 $GeV$ from 1994-1997 and since 1998 it was increased to 920 $GeV$. The corresponding centre of mass energy, $\sqrt{s}$, was 300 $GeV$ (1994-1997) and 318 $GeV$ since 1998. The remarkable asymmetry in the energies between electron and proton beams largely influence the detector designs and is just another unique feature of the accelerator. HERA is equivalent to a fixed target facility with an incident electron beam energy of $\sim 52\ TeV$! At this energy electrons and protons can be probed at distances as small as $10^{-18}\ m$.

The accelerator is 6.3 $km$ long, and consists of four curved and four straight

[1] Here and in the following, the term 'electron' denotes generically both the electron ($e^-$) and the positron ($e^+$).

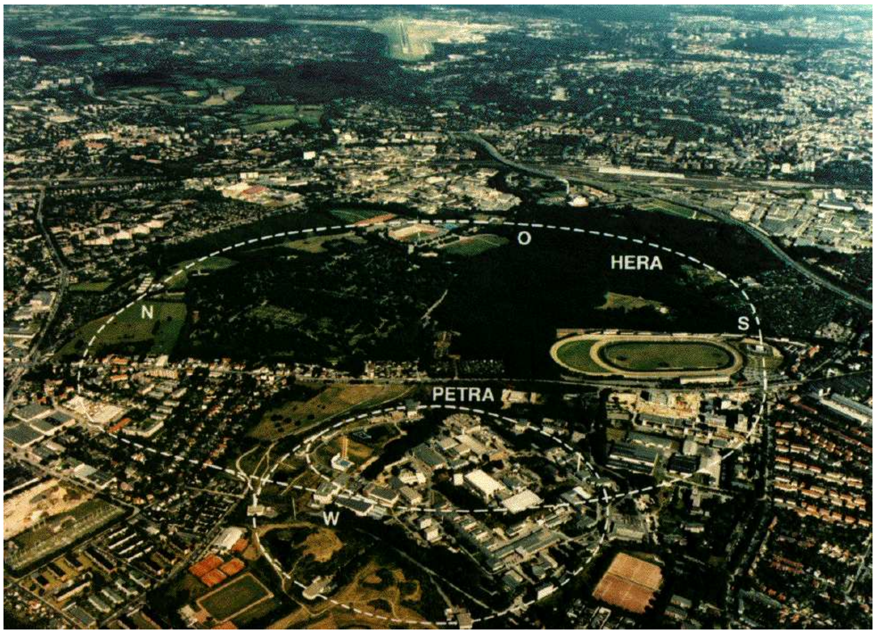


Figure 3.1: HERA and DESY main site.

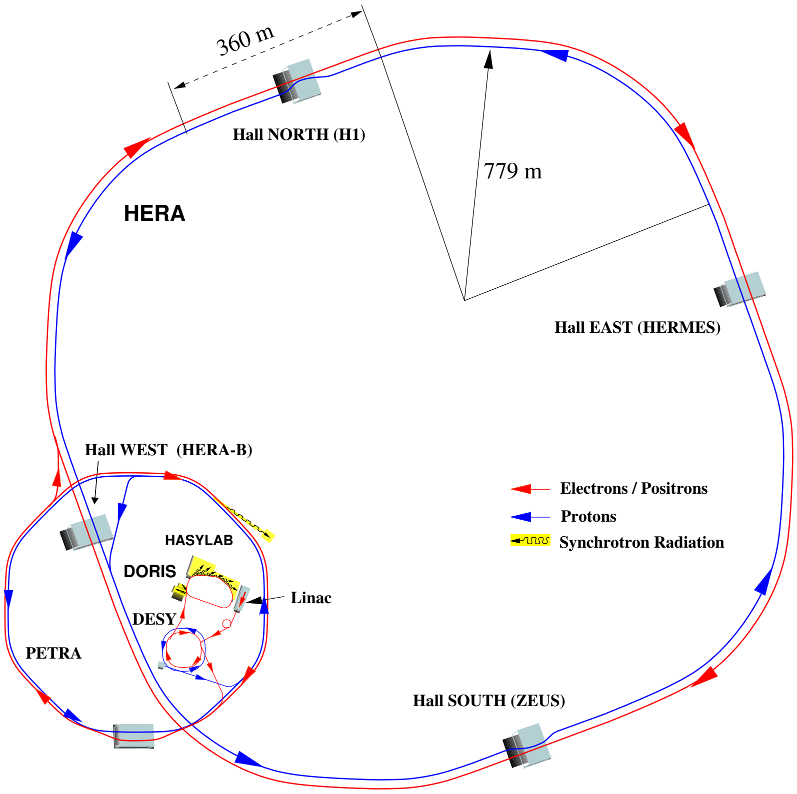


Figure 3.2: Sketch of the HERA facilities.

sections. Two general purpose detectors, H1 and ZEUS, are situated at places where two beams are brought in collision, at the north and south side of the accelerator. The HERMES experiment, dedicated for nucleon spin structure studies by colliding longitudinally polarized lepton beam onto a polarized gas target, is situated in the east hall. The HERA-B detector, primary designed for measuring CP violation in the $b\bar{b}$ system by colliding proton beam halo on a fixed target, is placed in the west hall.

To maximize the luminosity (quantity suitable to describe colliding characteristics, see Section 3.2.3), each beam is structured in up to 210 bunches, with ten empty bunch crossings giving ten unpaired bunches, used for the backgrounds estimations and detector calibrations. The time interval between bunches is 96 $ns$ (28.8 $m$) which corresponds to the beam crossing frequency of 10.4 $MHz$. The length of the electron bunches is 0.83 $cm$ and 8.5 $cm$ for the proton bunches. The resulting HERA machine desired peak luminosity for the period 1994-2000 is $1.5 \times 10^{31}$ $cm^{-2}sec^{-1}$. The integrated luminosity delivered by HERA as a function of days of operation is shown in Fig. 3.3.

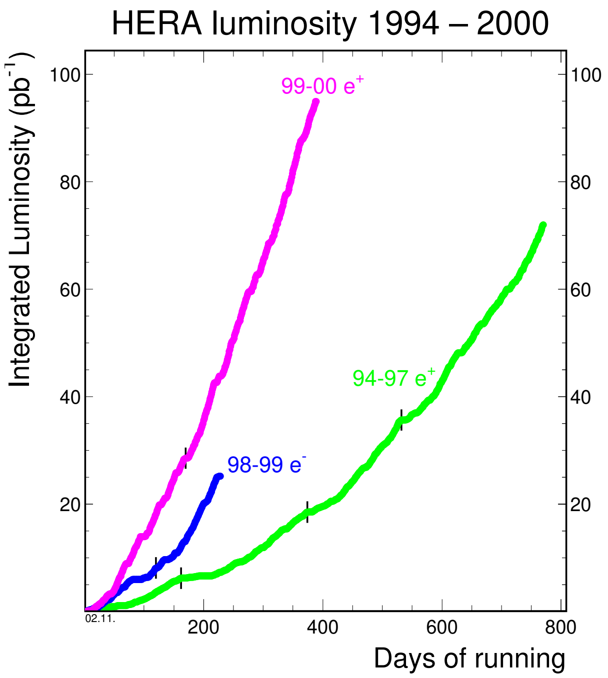


Figure 3.3: Integrated Luminosity delivered by HERA.

The electron pre-acceleration consists of several facilities, the last one being the PETRA II ring. Electrons are extracted from a hot cathode and positrons are produced by pair production from bremsstrahlung photons, obtained using an electron beam. Just before injection into HERA, PETRA II is filled with 70 bunches each with $\sim 10^{10}$ electrons spaced apart as in HERA (96 $ns$). The electron energy just before injection into HERA is 12 $GeV$. The whole injection procedure is repeated twice to achieve the designed 210 bunches in the HERA ring. The final HERA electron energy for the data taking period relevant for this work was 27.5 $GeV$.

The proton pre-acceleration consists, as well, of several parts and ends with the PETRA II ring. The source of the protons are negatively charged hydrogen ions which are stripped of negative charges during the pre-acceleration process. The maximum number of 70 bunches with $\sim 10^{12}$ protons are accelerated to 40 $GeV$ before injection to HERA ring. The whole procedure is repeated twice more as in the electron case. The maximum proton energy of the HERA accelerator is 920 $GeV$.

The HERA electron and proton beams are guided and accelerated by two separate magnet and cavity systems.

## 3.2 ZEUS

The ZEUS detector is a multipurpose particle detector designed to study the rich spectrum of HERA physics. ZEUS has the usual features of a nowdays collider experiments. The tracking system is the most inner part, uses a uniform magnetic field (1.43 $T$) of a thin superconducting solenoid. The solenoid is surrounded by a high resolution calorimeter. This is further enclosed by an iron sampling calorimeter (backing calorimeter) which also serve as a return yoke for the solenoid magnetic field. The most outer part is the muon chamber system, mounted on the inside and the outside of the backing calorimeter. Other ZEUS detector components are placed close to the beampipe to measure backgrounds, luminosity and for small angle tagging.

The detail description of the ZEUS detector can be found elsewhere [23]. In this section, an outline of the detector components of particular relevance to this thesis is given, as well as the data acquisition and ZEUS Trigger System. The detector overview is schematically presented in Fig 3.4 and 3.5.

All positions and angles will be quoted with respect to the ZEUS reference frame. That is a right handed frame with the $z$ axis pointing in the proton beam direction of motion, refered to as forward direction. The transverse coordinates are defined as: $y$ axis is perpendicular to the beams pointing upwards, and the $x$ axis

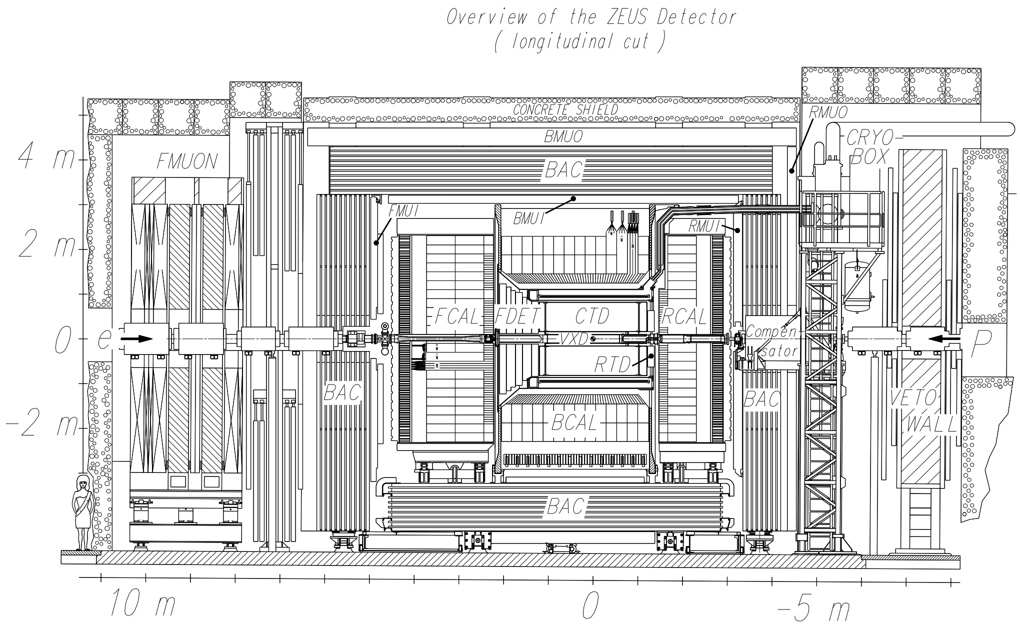


Figure 3.4: The $rz$ view of the ZEUS detector.

points to the centre of the HERA ring. The polar angle, $\theta$, is measured w.r.t. the positive $z$ axis and the azimuthal angle, $\phi$, w.r.t. the $x$ axis.

### 3.2.1 Central tracking detector

The *central tracking detector* (CTD) is the main tracking device of ZEUS. At first, a *vertex detector* (VXD) was installed inside the CTD, but it was removed during the 1995/1996 shutdown and VXD was not concidered in this study. The CTD is a cylindrical wire chamber. Using the uniform magnetic field, it measures charges, trajectories and momenta of the charged particles. In adition, particle identification is possible through the measurement of the energy loss $dE/dx$.

The radial extension is between 16 $cm$ and 85 $cm$ and covers the polar angle range from $11.3^\circ < \theta < 168.2^\circ$ with full azimuthal coverage. The CTD is divided into 9 superlayers and each superlayer is further divided into cells of 8 sense wires separated by ground wires, see Fig. 3.6.

Odd numbered superlayers are aligned parallel to the $z$-direction and even numbered ones are tilted by $\sim 5^\circ$ angle to improve the z determination.

The CTD is operated with a gas mixture of $Ar/CO_2/C_2H_6$, in the proportions of 83/3/14 by volume. This mixture has been chosen on the grounds of safety and

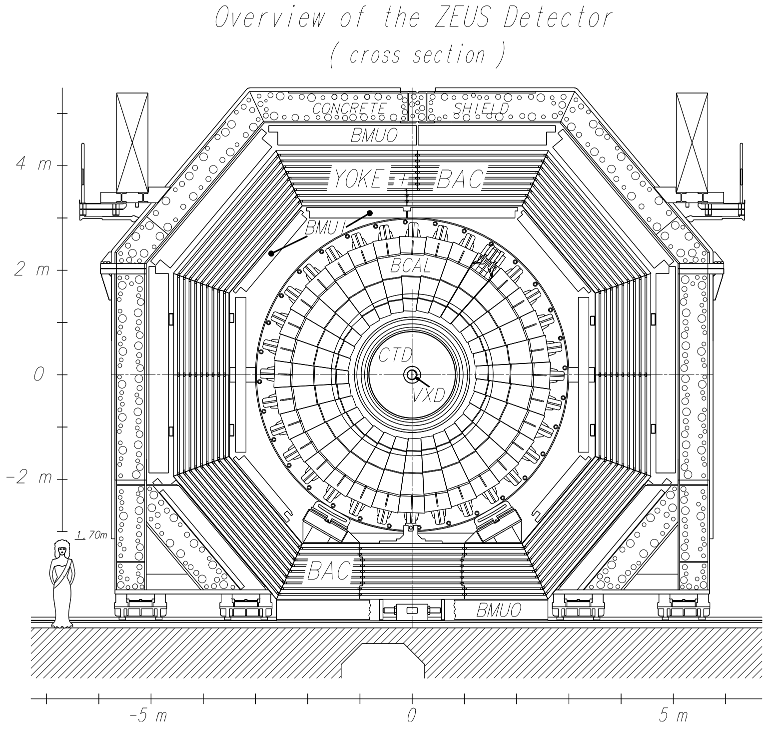


Figure 3.5: The $xy$ view of the ZEUS detector.

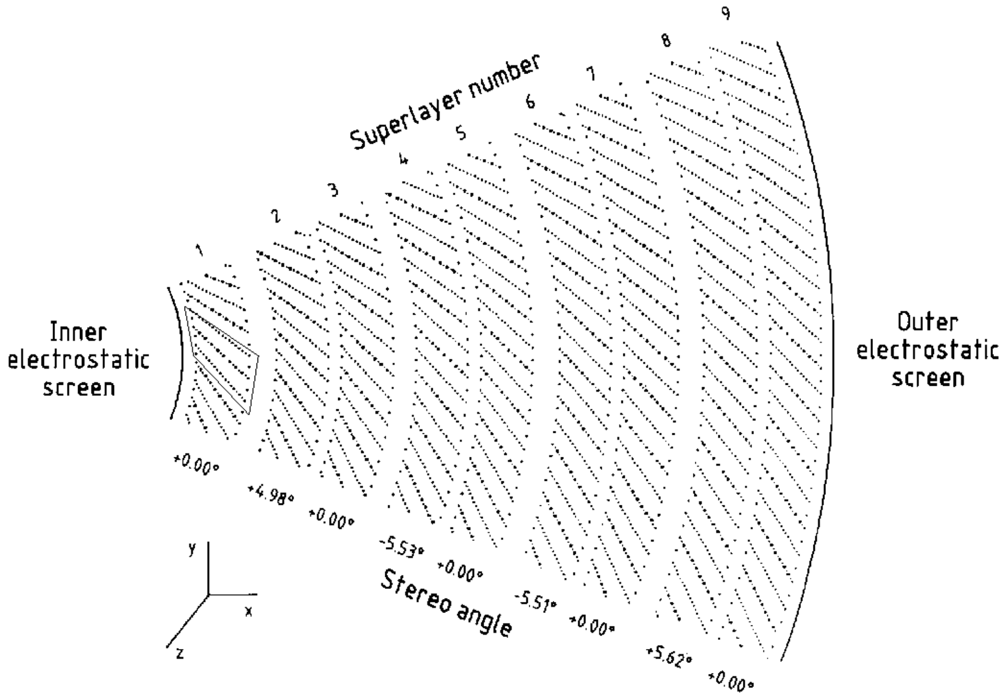


Figure 3.6: The CTD wires.

detector lifetime, although a pure argon-ethane mixture (50/50) would provide a better resolution and less noise [24].

Charged particles traversing the CTD active area ionize gas molecules. The electrons drift to the positive sense wires with a drift velocity of $\sim 50\ \mu m/ns$, while the positive ions drift towards the negative wires. Close to the sense wires an avalanche-like multiplication takes place and amplifies the signal by a factor $\sim 10^4$.

There is a possibility to reconstruct the $z$-vertex by an arrival time difference of the signal between the two ends of the sense wires in superlayer 1, 3, and 5. The time resolution is $\sim 200\ psec$ which gives a $z$-resolution $\sim 4\ cm$. This fast $z$-vertex reconstruction is used for trigger purposes to suppress the non-$ep$ collision background. The transverse momentum resolution for tracks crossing all the superlayers of the CTD can be parametrised as $\sigma(p_T)/p_T = 0.0058 p_T \bigoplus 0.0065 \bigoplus 0.0014/p_T$ for track transverse momentum $p_T > 150\ MeV$. Here $p_T$ is expressed in GeV and the $\bigoplus$ sign indicates a quadratic sum. The first term in the expression is associated to the CTD single-hit resolution and limits the high momentum tracks resolution. The second term parametrises the multiple scattering inside the drift chamber and places a lower limit on the momentum resolution. The third term is relevant for low $p_T$ tracks and can be atributed to scattering in the beampipe and inner wall of the CTD. These parameters have been obtained using the detector simulation (tuned with data) on generated tracks coming from the $D^\star \to D^0\pi_s \to (K\pi)\pi$ channel [25].

The resolution in the measured polar angle for tracks with large $p_T$ is $\sim 3.5\ mrad$ [28]. This resolution is better than the calorimeter resolution and thus gives a preferable measurement technique to determine a polar angle of the isolated tracks. Such determination is not affected by any possible misalignment between CTD and calorimeter.

The typical CTD primary $z$-vertex resolution is $< 2\ mm$ and $< 1\ mm$ in the $xy$ plane for events with high momentum transfer and several tracks.

In the forward region (proton direction) the CTD acceptance is extended by the *forward tracking detector* (FTD), a system of three planar drift chambers. Between the three FTD chambers, the modules of a *transition radiation detector* (TRD), designed to improve hadron-electron separation in the forward region, are positioned. FTD and TRD together form the *forward detector* (FDET). In the rear region, a single chamber of the *rear tracking detector* (RTD) is placed. The design of the RTD is identical to the FTD. The FTD covers polar angle from 7.5° to 28.0° and the RTD covers the region from 160.0° to 170.0°.

The analysis described in this thesis was based on the CTD only tracking.

### 3.2.2 Calorimeter

Calorimeters are devices which measure energies of particles in high energy physics. They are central components of the large experiments at present colliders. In this section, the very basic ideas of calorimetry will be presented, as well as the description of the ZEUS calorimeter.

#### 3.2.2.1 Basics of calorimetry

The interactions of particles with a matter are the essence of detection devices. The nature of the reaction depends on the type of a particle itself, its energy and the penetrated material. A calorimeter absorbs an incident particle completely and transforms its energy into measurable signal for, both, charged and neutral particles. The penetrated detection material can suffer a damage from incoming particle radiation and may change it's detection characteristics. Therefore, the knowledge of particle reactions and effects of these reactions on the material is of fundamental importance in the detector design.

The following processes predominantly characterise the passage of particles through matter with kinetic energies from several $keV$ upwards [29]:

- nuclear reactions,
- elastic or inelastic scattering from nuclei,
- inelastic collisions with the atomic electrons of the material,
- emission of Cherenkov radiation,
- bremsstrahlung.

In high energy physics (typical energies of the particles are above $\sim 10\ MeV$) all charged particles, with an exception of muons, make, so called, particle showers as a result of their penetration through the matter of the detector. The nature and characteristics of the electron and photon induced showers are different from those of hadrons, hence there are two general types: *electromagnetic* and *hadronic showers*. A hadronic shower has much larger longitudinal and transverse dimensions than electromagnetic showers. This difference is commonly used to identify electrons, positrons and photons (high energy photons develop showers similar to the electron ones). Like high energy photons, the detection of neutrons and other long lived neutral particles requires a transfer of all or part of their energy to a particle capable of ionizing and exciting the detector material by either nuclear or electromagnetic interaction.

The distinction between different types of heavy particles is achieved using the energy deposition dE/dx described by Bethe-Bloch formula [30], using Cherenkov radiation when the velocity of the particle is greater than the speed of light in the same medium and using other techniques.

The length scale appropriate for a description of hadronic showers is *the nuclear interaction length* $\lambda_{int}$ [31] defined as the mean free path of a particle before undergoing an inelastic interaction in a given medium.

A calorimeter based on scintillating materials is one of the most common energy measurement devices in particle physics. These calorimeters transform the part of completely absorbed energy of the incoming particle into fluorescence light. The light is transformed into measurable electrical signal by photo-detectors.

Several possibilities exist to assemble the calorimeter. A *homogeneous calorimeter* consists of one uniform material used for both energy dissipation and measurement ("active material").

However, as $\lambda_{int}$ of active material is typically large (e.g. 68 $cm$ for scintillator) [32], quite often calorimeters have to be sampling devices. A *sampling calorimeter* is based on alternating layers of passive absorbing material and active detector part. The absorbing material is usually of high density $\rho$ and high atomic number, such as lead, tungsten or iron. Plastic scintillators, liquid argon or silicon diodes are common choices for the active material. Whatever configuration is, the calorimeter has to fulfill some requirements. It should be sensitive to charged as well as neutral particles in the desired energy range.

In sampling calorimeters a signifficant fraction of energy remains in the absorbing material due to nuclei fragmentations and does not contribute to the measurable signal. At the same incident energy the ratio of the measurable energy of electromagnetic to hadronic showers is larger than unity, i.e. $e/h > 1$.

To reduce the $e/h$ ratio to a value close to 1, the energy of the hadronic shower which remains in the absorbing material has to be compensated. For this purpose the ZEUS calorimeter was constructed using *depleted uranium* (DU) as an absorbing part. The active material is made of plastic scintillators. The hadronic shower traversing the DU plates produces fast neutrons whose kinetic energies are proportional to the energy loss due to nuclear reactions in the shower. These neutrons lose most of their energy in elastic scattering off the free protons of the scintillator and hardly anything due to scattering off the heavy uranium nuclei. The thicknesses of both parts were chosen in a such way that the deposited energy of the neutrons compensates the energy loss of the hadronic shower and the achieved $e/h$ ratio is close to unity [33].

#### 3.2.2.2 The ZEUS calorimeter

The high resolution ZEUS *calorimeter* (CAL) is a sampling calorimeter with equal response to electrons (positrons and photons) and hadrons at the same incident energy. The absorber plates are made of depleted uranium and plastic scintillator layers have been chosen as active material. The depleted uranium plates have a composition of 98.1% $U^{238}$, 1.7% $Nb$ and less than 0.2% $U^{235}$. The optical readout is realized via plastic wavelength shifters, lightguides and photomultipliers. In order to achieve equal response to electromagnetic and hadronic showers, 3.3 $mm$ thick uranium layers corresponding to 1 radiation length (the distance over which the electron energy is reduced by a factor 1/e due to radiation loss only) alternate with 2.6 $mm$ thick scintillator plates. The main features of the ZEUS calorimeter are:

- large solid angle coverage (99.7% of the solid angle),
- energy resolution for hadrons of $\sigma(E)/E = 35\%/\sqrt{E} \bigoplus 2\%$,
- energy resolution for electrons of $\sigma(E)/E = 18\%/\sqrt{E} \bigoplus 2\%$,
- calibration of the absolute energy scale to 1%,
- precise angular resolution for particles ($\leq 10\%$ $mrad$),
- longitudinal segmentation for hadron-electron separation,
- short signal processing time at the nano-second level.

The CAL is physically subdivided into *forward* (FCAL), *barrel* (BCAL) and *rear* (RCAL) *calorimeters*. Figure 3.7 shows the layout of the ZEUS calorimeter.

The angular coverages of the FCAL, BCAL and RCAL are $2.2° < \theta < 39.9°$, $36.7° < \theta < 129.1°$ and $128.1° < \theta < 176.5°$ respectively. The inner(outer) radius of the BCAL is 122 $cm$ (229 $cm$). The large momentum imbalance between incoming electrons (27.5 $GeV$) and protons (920 $GeV$) send most particles into a narrow cone around the proton direction, i.e. the forward direction. Thus the FCAL is much thicker than the RCAL to account for this effect. For example, the maximum depth of FCAL is $7.1\lambda_{int}$ while the BCAL and RCAL are $5.3\lambda_{int}$ and $4\lambda_{int}$ thick. The choice of the thickness was determined by the requirement of at least 95% energy containment for 90% of the maximum energy showers at any polar angle.

The three calorimeter components have similar structures and are subdivided longitudinally into an *electromagnetic calorimeter* (FEMC, BEMC, REMC) with a depth of 1 $\lambda_{int}$ ($\sim$ 25 radiation lengths), which is sufficient to fully contain the electromagnetic showers, and *hadronic calorimeter* (HAC). In FCAL and BCAL the

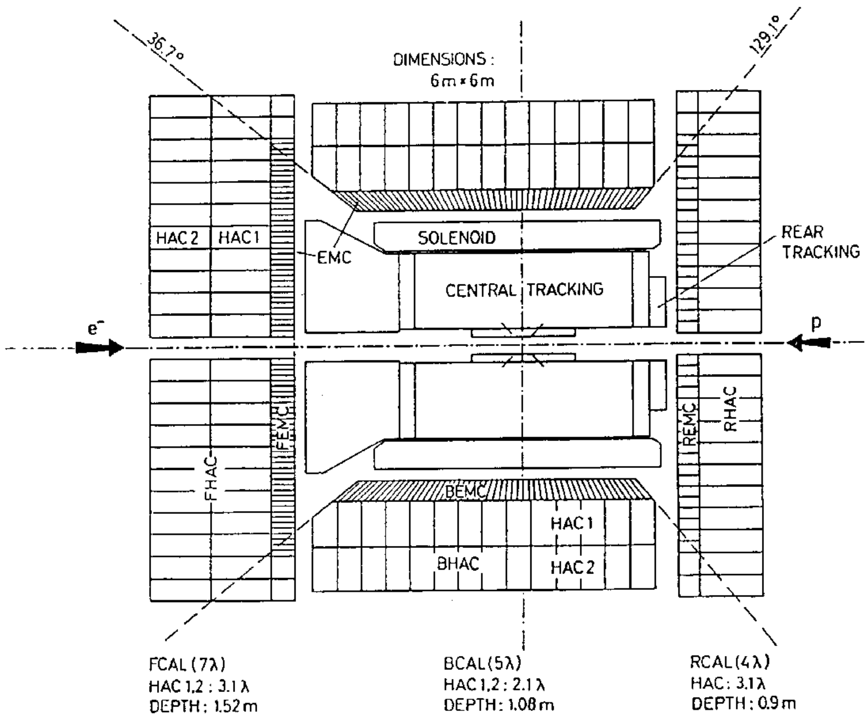


Figure 3.7: The ZEUS Calorimeter layout.

HAC section is devided into two subsections HAC1 and HAC2, while the RCAL has only one HAC section.

The whole calorimeter has a modular structure. The FCAL and RCAL calorimeters consist of 23 modules, , which follow the same construction principle, as shown in the Fig. 3.8, where an isometric view of FCAL module is given.

FCAL and RCAL modules are rectangular, while the 32 BCAL modules, which surround the CTD, are wedge-shaped. Each module consists of so called towers $20 \times 20$ $cm$, with the mentioned longitudinal subdivision (EMC+HAC). The EMC sections are further transversely subdivided into four cells (for the RCAL only two). These 5918 cells are the smallest readout units of the CAL. Each cell is read out on two sides via wavelength shifters by *photomultiplier tubes* (PMT). Whereas the sum of the signals of both photomultipliers are independent of the impact point of the particle, the horizontal impact point can be deduced by comparing the two signals.

The timing resolution for each cell is $\sigma_t = 1.5/\sqrt{E} \bigoplus 0.5$ $ns$, where $E$ $(GeV)$ is the energy deposited in the cell, yielding $< 1$ $ns$ for $E > 4.5$ $GeV$. The timing information from the calorimeter is useful to remove non-$ep$ background already on the trigger level. The characteristic timing profiles are different for good $ep$ events in comparison to all kinds of non-$ep$ interactions (for example: beam-gas and cosmic rays), and give useful separation power.

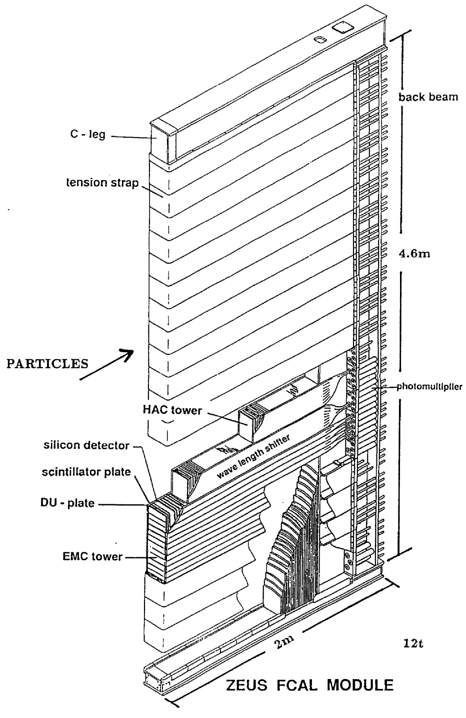


Figure 3.8: The FCAL module.

The main calibration of the ZEUS calorimeter is making use of the natural uranium radioactivity. This produces a low and stable background current in the PMTs, which helps in detecting possible irregularities in the operation of photomultipliers. On the other hand, to calibrate the electronic system readout for each channel, test pulses are used to simulate the signal coming from the PMTs. In that way, it is possible to calibrate the effects of the electronics, after subtraction of the noise contribution. The calorimeter is calibrated on a daily basis.

### 3.2.3 Luminosity measurement

An important quantity that characterises the collision performance is the luminosity. This quantity determines the rate at which interractions occur. For the time integrated *luminosity* (L) and the *cross section for a given process* ($\sigma$) the *number of events observed* (N) is given by:

$$N = L \cdot \sigma \tag{3.1}$$

So, the only way to increase the number of observed events is to increase the luminosity, because the cross section is a given quantity. The luminosity is controlled by the parameters of the collider, such as the number of bunches, the number of particles per bunch, the spatial dimensions of the bunches and the bunch crossing time.

To measure the luminosity with enough accuracy is one of the essential requirements which high energy physics experiment has to fulfill. The value of the luminosity can be either calculated provided there is a good knowledge of the collider parameters or can be determined by using well known process (i.e. calculable with small uncertanties) and applying Eq. 3.1. Any process to be used to monitor the luminosity has to have a fairly large cross section, so that the measurement performed in a short time is a reasonably accurate estimation of the instantenous luminosity (the luminosity per second).

At HERA, the *ep-bremsstrahlung, Bethe-Heitler process*

$$ep \rightarrow e'p\gamma$$

is used to measure luminosity. The cross section for this process is large enough ($\sigma_{BH} \geq 20\ mb$) and the photon energy spectrum can be calculated to an accuracy of 0.3% [34]. In this process, the incoming electron radiates a high energy photon in the electromagnetic field of the proton. The momentum transfer to the proton is most often negligible, so that the combined energy of final state electron and photon is equal to the electron beam energy.

The luminosity monitors consist of three small electron taggers and a photon calorimeter. Initially, the luminosity was calculated by requiring the coincidence detection of an energetic photon and an electron. However, after 1992, the background conditions were sufficiently good to allow a precise lumi determination using only the bremsstrahlung photons, with the electron detectors used for estimating the systematic uncertainty.

An electron and photon emerge from the interaction point at very small angles with an average of about 230 and 70 $\mu rad$ for the horizontal and vertical directions, respectively [35]. The beampipe has a Cu-Be exit window for the photons at $z = -92.5\ m$. The photon calorimeter is placed at $z = -107\ m$, see Fig. 3.9.

The photon detector consists of a carbon filter to absorb synchrotron radiation, an air filled Cerenkov counter to veto charged particles, and a lead scintillator sampling calorimeter. The photon detector has 98% geometrical acceptance independent of the photon energy for bremsstrahlung events. The resolution in the coordinates perpendicular to the photon beam is about 3 $mm$, corresponding to an uncertainty of $\sim 30\ \mu rad$ on the photon angle. This accuracy allows to measure the position and angular dispersion of the electron beam, to tune the electron beam. The energy resolution of the calorimeter is around $\sigma(E)/E = 20\%\sqrt{E(GeV)}$. The

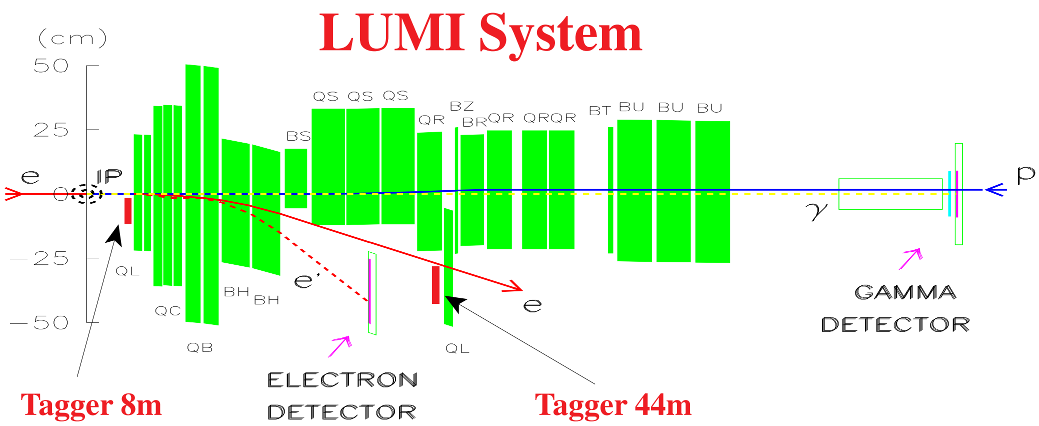


Figure 3.9: The LUMI system.

detector is additionaly protected by moving it behind the lead shielding during beam injection.

Electrons resulting from a Bethe-Heitler process have an energy smaller than the beam electrons, and their trajectories are bent by the HERA magnets towards the centre of the ring. They can be detected by small taggers placed at $z = -8\ m$, $-35\ m$, $-44\ m$ on the inside of the HERA ring. The detectors placed at $z = -8\ m$ and $-44\ m$ are small tungsten-scintillator sampling calorimeters and the detector placed at $z = -35\ m$ is of a similar construction as the photon calorimeter. These detectors are used to tag photoproduction events, as well.

The luminosity measurements suffers from a number of background processes. The most important background comes from electron beam-gas bremsstrahlung, $eX \rightarrow e'X\gamma$, which can mimic a Bethe-Heitler process and its contribution is subtracted statistically using electron pilot (unpaired) bunches. The effect of miscounting of the Bethe-Heitler photons (so called pile-up effect), the calorimeter energy calibration, linearity and acceptance have to be taken into account, as well.

The recorded statistics is sufficiently large and the statistical uncertainty of the luminosity measurement is negligible while the overall systematic uncertainty for the 1994-2000 data taking periods is $\sim 2\%$.

### 3.2.4 Other components

The iron yoke surrounds the inner tracking system and the calorimeter and serves as the *backing calorimeter* (BAC) to detect the leakage of energies from the calorimeter. The energy resolution of the BAC is $\sigma(E) = 1.0\sqrt{E(GeV)}$ for hadrons.

Muons with energies greater than 2 $GeV$ will easily escape the calorimeter. Thus, for muon identification, the BAC is instrumented in the front and behind with large *limited streamer tube* (LST) chambers to measure the directions and positions of muons. The muon chambers are constructed in three main parts: the *forward* (FMUON), *barrel* (BMUON), and the *rear region* (RMUON). In crossing the iron yoke between the inner and outer muon chambers, muons lose approximately 1 GeV of energy.

The forward direction is equipped with special muon chambers, which give an independent measurement of the muon momentum up to 100 $GeV$ and down to very small angles. The detector consists of a toroidally magnetised iron part, interleaved with sections of drift chambers, limited streamer tubes and time-of-flight counters.

Behind the RCAL ($z = -3.2\ m$), untill the year 2000, the *C5 counter* has been positioned. In 2001, the old lead-scintillator C5 counter was replaced by new tungsten-scintillator one, and placed in front of the RCAL ($z = -1.234\ m$). A detailed description of the functionality of the new C5 counter will be presented in the next chapter.

Particles produced upstream of the main detector by the incoming proton beam are detected by a *vetowall detector*. It is made of two layers of scintillator on either side of an 87 $cm$ thick iron wall centered at $z = -7.3\ m$.

### 3.2.5 Triggering and data acquisition

The expected $ep$ event rate under nominal HERA I running conditions (1994-2000) is $\sim$ 300 $Hz$, while the expected backround event rate is several orders of magnitude larger. The dominant background origins from beam-gas interactions (order of few $kHz$ or more) and cosmic rays ($\sim$ 500 $Hz$). The total designed data taking rate of the ZEUS detector is 5-10 $Hz$, depending on the event size.

The ZEUS trigger system [36] was designed to filter an input event rate to an output rate of interesting physics events of $\sim$ 10 $Hz$.

The system is divided into three trigger levels. This allows more processing time for the more complex algorithms used at the higher levels while keeping the system essentially free of dead time (lost of the valid bunch crossing information due to the trigger failures). A diagram of the trigger chain is shown in Fig. 3.10.

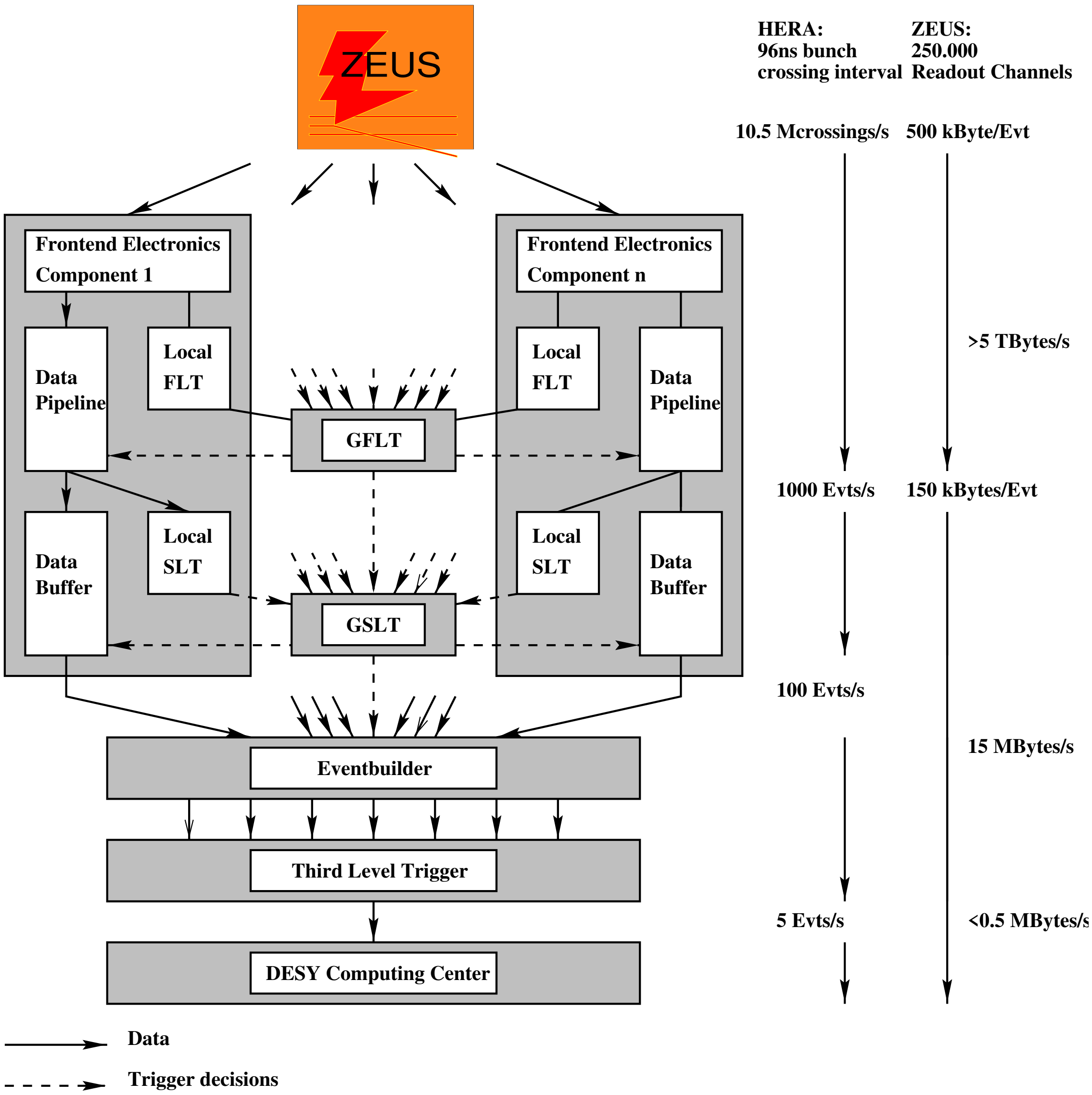


Figure 3.10: The ZEUS trigger system.

The *First Level Trigger* (FLT) is a hardware trigger, designed to reduce the input rate below 1 $kHz$. The components of the ZEUS detector have their own FLT, which stores the data in a pipeline and makes a trigger decision within 2 $\mu s$ after the beam crossings. The decisions from all the FLTs are collected by the *Global First Level Trigger* (GFLT), which decides whether to accept or reject the event and returns this decision to the different components within 4.6 $\mu s$, corresponding to 46 beam crossings. The FLT operates only on a small subset of detector information to achieve such a rate in the decision. At this level most of the beam gas related background is rejected. To do this, the tracking FLT performs a first determination of the event vertex using CTD $z$-by-timing system, mentioned in Section 3.2.1, in combination with the information from forward tracking detectors. The event is rejected if the reconstructed vertex is outside of the detector volume.
The calorimeter FLT (CFLT) calculates global sums of energy and transverse energy in the calorimeter and searches for patterns consistent with the detection of isolated electrons or muons. The fast analysis of calorimeter data are used to reject the event consistent with background.

If the event is accepted by FLT , the data are transferred to the *Second Level Trigger* (SLT), which is software based and runs on a network of transputers. For the SLT almost all the event information is used. The *Global Second Level Trigger* (GSLT) recieves all of the SLT info from the individual components, as well as the trigger information from the GFLT. The SLT produces a decision within 3 $ms$ after the corresponding *ep* interaction. At this level, the rate is reduced below 100 $Hz$. For example, the SLT rejects proton beam-gas interactions using the calorimeter timing information, thus reducing the FLT rates by an order of magnitude without loosing good *ep* collision events.

If the event is accepted by the GSLT, all the detector components send their data to the *Event Builder* (EVB). The EVB collects the information to reconstruct the event. The data are then passed to the *Third Level Trigger* (TLT) which is software based and runs a reduced version of the offline data analysis. The trigger runs physics based filter code on complete events. The TLT reduces the rates to a few $Hz$ and the events accepted by the TLT are written to tape for further studies.

# CHAPTER 4
# THE NEW C5 COUNTER

During the years 2000-2001 there was a major shutdown of the HERA collider to increase the $e^{\pm}p$ peak luminosity from 1.5 to $7.0 \cdot 10^{31}$ $cm^{-2}s^{-1}$ and to provide longitudinally polarised lepton beams with a polarisation up to 55%. The superconducting magnets have been installed inside the collider detectors, H1 and ZEUS, to reduce the transverse size of the beams at the interaction point, and hence to achieve the desired luminosity inhancement. Only before and after the experiments, *"spin rotators"* have been positioned to obtain sufficient longitudinal polarisation for the HERA experiments. The polarised beams are specially interesting for studies of nucleon spin structure and electroweak aspects of the Standard Model.

To fully profit from the new situation a *silicon microvertex detector* (MVD) and a new forward tracking device, the *straw tube tracker* (STT), were installed in the ZEUS experiment. The STT detector has been installed instead of the transition radiation detector, TRD. The new tracking system significantly improves the measurements in the forward direction which are of particular importance for many physics studies, like heavy quark production, QCD jet analysis and for various searches.

In addition, inside the ZEUS detector, the *new C5 counter* has been placed and this chapter contains a description of C5 and its functionality.

## 4.1 Hardware and readout

The C5 detector is sensitive to the particle flux created by interactions of the proton and electron beams with a residual gas in the beampipe. So, the signal for the C5 counter is exactly the major background for the ZEUS detector!

The C5 is positioned 1.2 $m$ from the nominal interaction point in the electron flight direction, in front of the RCAL, see Fig. 4.1, close to the collimators No. 5 (collimators protect the main detetector from background radiation).

The new C5 detector consists of $2 \times 2$ scintillator layers interleaved with layers of tungsten[1]. The shape of the C5 detector is a square of $20cm \times 20cm$ with the corners (triangles of side lengths $5cm \times 5cm \times 7cm$) removed. The total thickness is

[1]The old C5 was a scintillator-lead combination and was installed untill 2000-2001 shutdown.

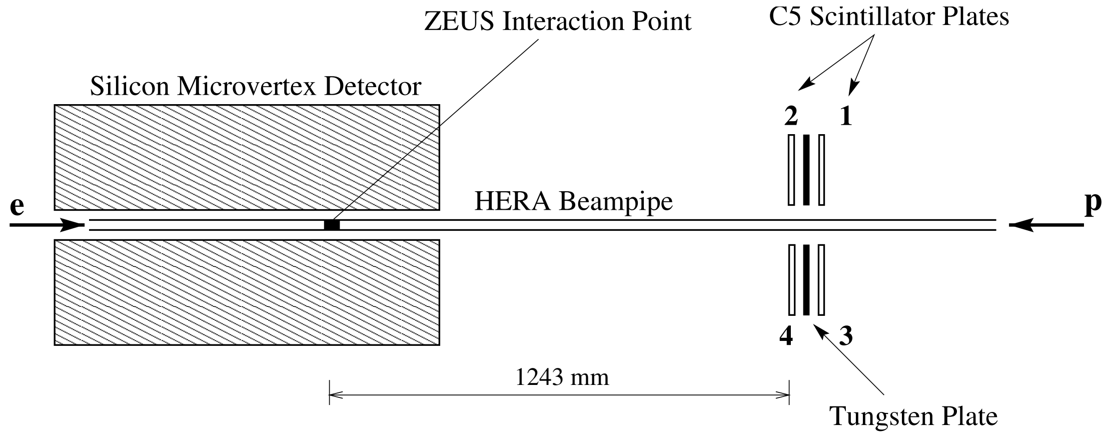


Figure 4.1: The position of the C5 counter relative to the ZEUS interaction point.

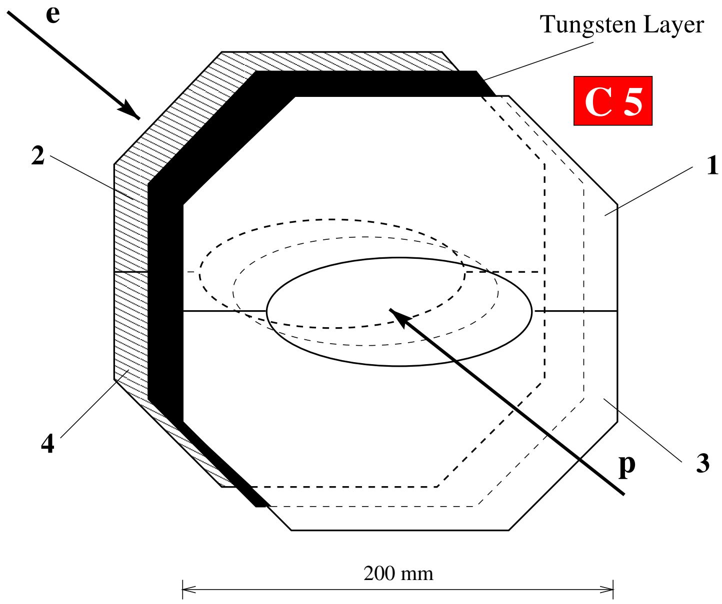


Figure 4.2: The arrangement of the C5 plates. Note that there are two additional tungsten planes, in front and behind the counter.

69 $mm$. The four scintillator plates are arranged in two planes, such that one plate is located above the beampipe and the other located below the beampipe, see Fig. 4.2. Each plate has a tickness of 5 $mm$. The scintillator material is SCFN36 [37]. The scintilator planes are separated by a tungsten plane and they are surrounded by a tungsten housing. Tungsten was chosen as shielding material against synchrotron radiation.

Each scintillator plate is read out independently, so there are four readout channels. The VME/PowerPC technology has been chosen for the readout system. The system reads out the rate information, digitized timing information and the ADC (analog-to-digital converter) data. The slewing effects of the C5 signal (lost of the signal due to the conduction of the light from the counter to phototubes) limit the time resolution of the counter (for more about C5 time resolution, see Section 4.2.1.2). A constant-fraction discriminator is used to reduce the slewing effects.

From the PowerPC, the data are transfered to a Linux-PC shared memory for further analysis and distribution.

## 4.2 Functionality of the C5 system

As mentioned, C5 is sensitive to the stream of particles coming from the beam-gas interactions. The tungsten housing and tungsten layer beetwen two scintillator plates makes it, essentially, insensitive to synchrotron radiation.

The C5 detector is usefull component of the ZEUS first level trigger and essential in the monitoring of HERA beam conditions, including bunch arrival times, vertex position and background rates.

### 4.2.1 Online and Offline monitoring of HERA beam conditions

The C5 counter is a major tool for the online and offline estimation of particle backgrounds inside the ZEUS detector. One of the consequences of the HERA machine upgrade is the more severe background condition near the interaction regions of the experiments. In addition, newely installed inner detector components reduce the background tolerance further more. Hence, the online (real time) and the offline monitoring of HERA beam conditions is essential for an optimal detector performance.

#### 4.2.1.1 Monitoring of background rates

The signals from the four C5 scintillator plates are used to measure particle background rates, namely single and coincidence rates. Single rates are obtained from each of the scintillator plates separately, while coincidence rates are just the logical AND of the signals from the two plates above the beampipe (plates 1 and 2) and two plates below the beampipe (plates 3 and 4), respectively. The effects of a tungsten plane between coincidenced scintillator planes and discriminator readout threshold, make coincident rates totally insensitive to the synchrotron radiation.

The rates measured for a typical 12 hours period of the HERA running are shown in Fig. 4.3, together with the corresponding HERA beam parameters. The C5 rates closely follow the HERA activity. At the beginnig the rate is stable and slowly decreasing as the HERA electron current decreases. This is typical luminosity (data taking) condition. At the end of the fill, the reduced lifetime of the electron beam results in an enhancement of C5 rate. No spikes in the rates are visible when beams are dumped indicating a clean beam dumping. Large spikes are seen during the proton beam injection and acceleration, as well as during injection and acceleration of a lepton beam. The period of luminosity tunning typically reduces the C5 rates, followed by a smooth and slowly decreasing rate period indicating luminosity conditions, once more.

The C5 rates are readout at least every second and are online displayed in the HERA and the ZEUS control rooms for permanent beam monitoring.

A signifficant increase of the C5 rates without an obvious reason (beam injection, acceleration and steering) usually indicates serious problems (e.g. collimators are not closed, beam conditions are unstable or beam dumping was not clean,...).

To protect the ZEUS calorimeter from large background, the forward and the rear part of the ZEUS calorimeter are opened (moved out on the extension rails) during the beam injection. The C5 rate info plays a crucial role to decide when to close the calorimeter and start data taking.

#### 4.2.1.2 The C5 online bunch timing and $z$-vertex information.

The C5 coincidence signals are used for timing measurements, as well. TDCs (time-to-digital converter) are started by the 10.4 $Mhz$ HERA proton clock and stopped by the C5 signals. The TDC info is integrated over a period of 30 $s$.

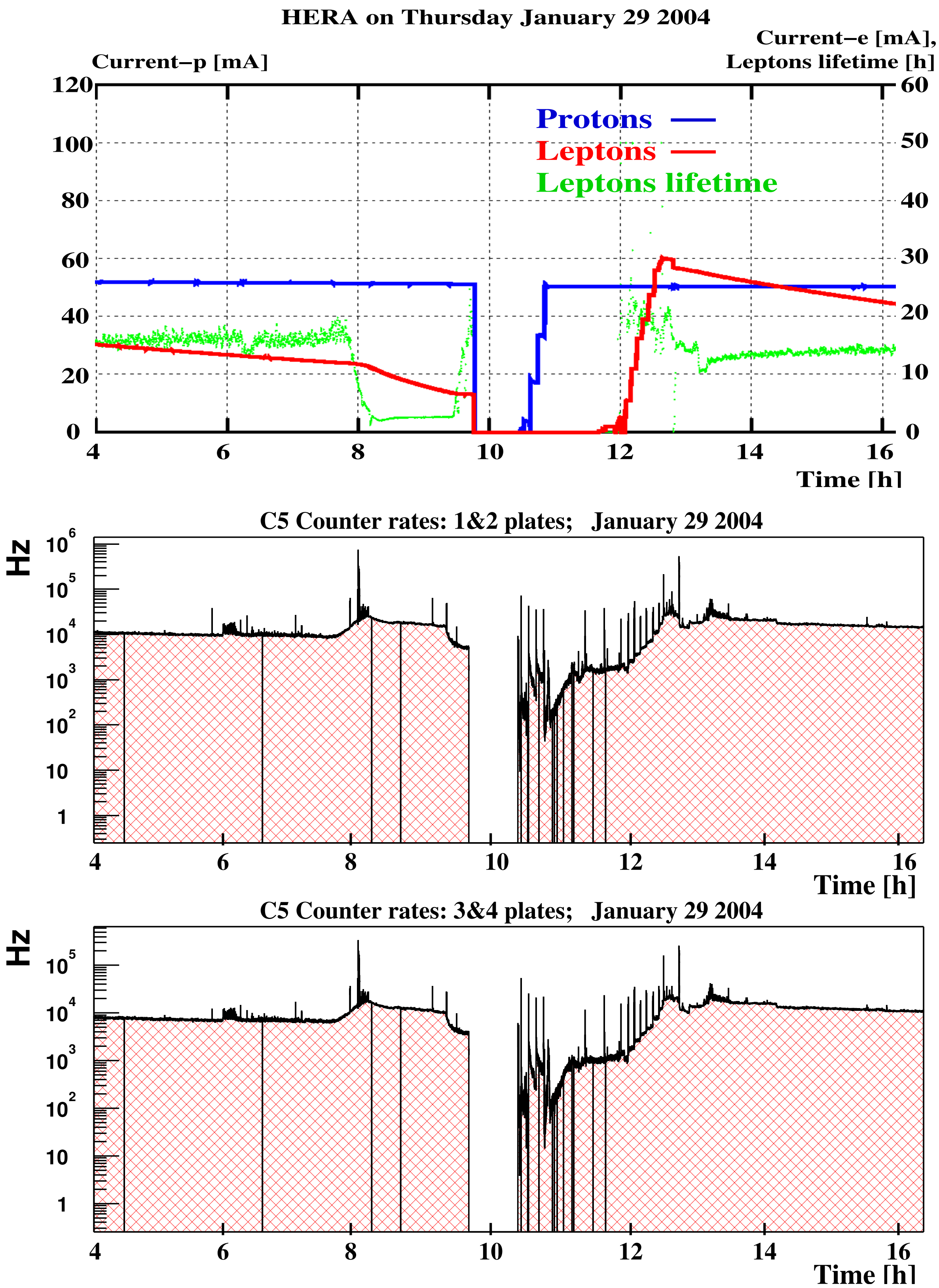


Figure 4.3: HERA beam currents and C5 counter rates on 29/01/2004.

A typical C5 timing profile is presented in Fig. 4.4. The information shown is accumulated over the integration period. The internal TDC resolution is 200 $ps$.

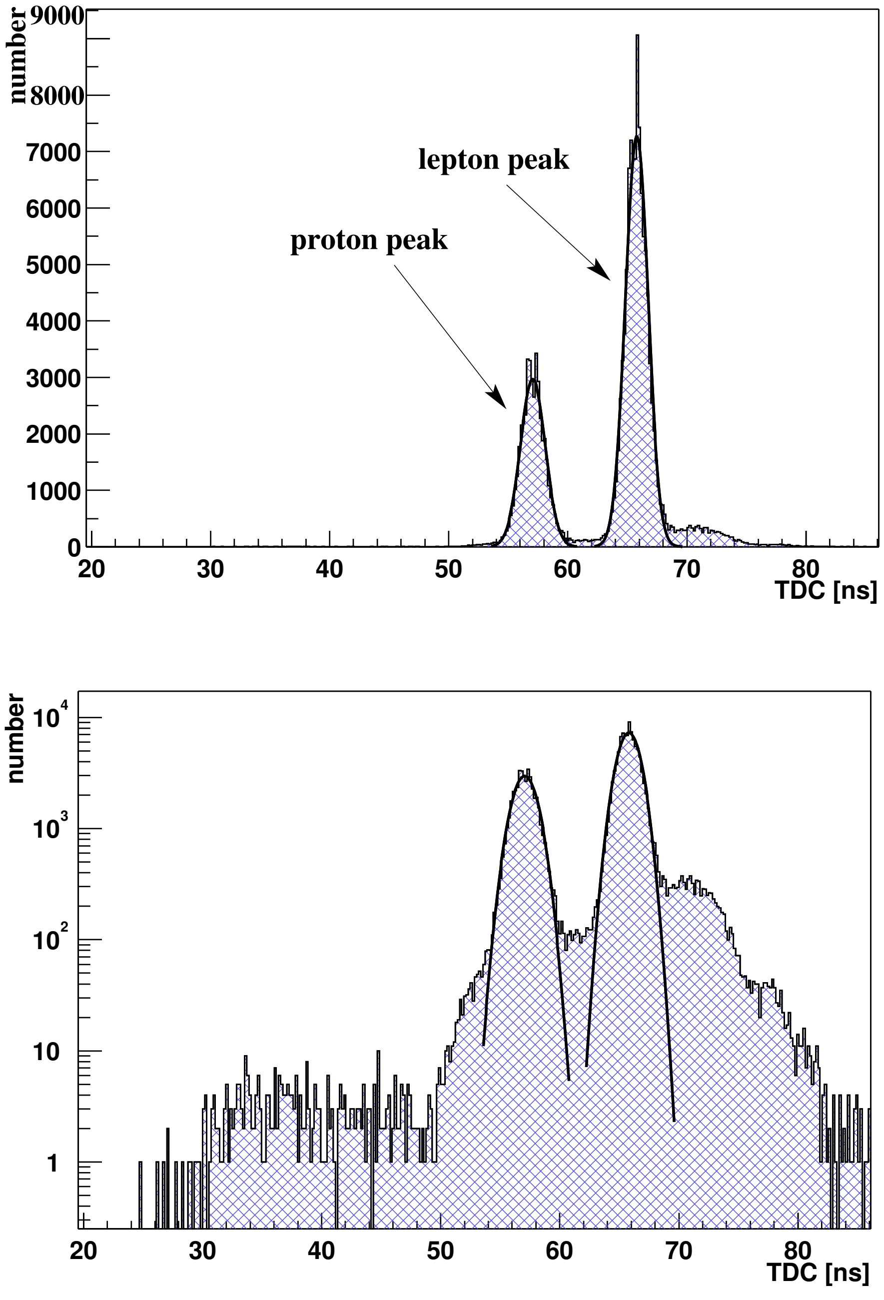


Figure 4.4: The C5 TDC profile as linear and logarithmic scales.

Because the C5 is positioned in the electron flight direction upstream from the ZEUS interaction point ($z_{C5} = -1.234\ m$), the main proton induced background peak arrives earlier than the corresponding lepton peak.

The C5 system performs an online Gaussian fitting of the time profiles resulting in a precise determination of bunch arrival times. The length of the electron bunch corresponds to a time period much shorter than the TDC internal resolution, so the half-width of the electron peak is a good estimation of the C5 counter resolution which is just below 1 $ns$.

From the logarithmic plot in Fig. 4.4 it is possible to estimate the contributions from electron and proton satellite bunches. The satelite bunches are results of high-frequency preacceleration facillities and their effect in the C5 TDC profile is manifested as a tail of the main beam peaks. From the figure it is obvious that proton satelite contribution is very small, while the tail of the main electron peak is larger. However, this electron tail cannot be uniquely associated to the electron satelite, but to the exponentially falling time distribution of halo and spray particles, as well as to the slewing effects of the C5 signal.

Knowing the position of the C5 counter and assuming that the signals travel with the velocity of light, it is straightforward to calculate the nominal interaction $z$-vertex using C5 timing info:

$$z_{vtx} = (t_e - t_p) \cdot \frac{c}{2} + z_{C5} \tag{4.1}$$

where $t_p$ and $t_e$ are proton end electron arrival times, $c$ is the velocity of light and $z_{C5}$ is a nominal C5 position.

The calculation of the C5 $z$-vertex is performed online.

Using the bunch arrival timing it is posible to devide the total C5 rate into an electron and proton beam contributions.

The C5 system is equipped with another type of TDC. This TDC is a long range multi-hit TDC capable to encompass the whole HERA bunch train. The internal resolution of this TDC is 1 $ns$. It is started by the “bunch-crossing-zero” signal and stoped by the next “bunch-crossing-zero” signal. Therefore, this TDC contains bunch per bunch timing information and is usefull for a crosschecking of the first TDC information and for other studies. Figure 4.5 shows one (random) bunch-pair timing information from multi-hit TDC, which have been obtained at the same time as the TDC profile from Fig. 4.4. The similarities of the two TDC profiles (Fig. 4.4 and 4.5) are obvious which points out very similar bunch per bunch structure.

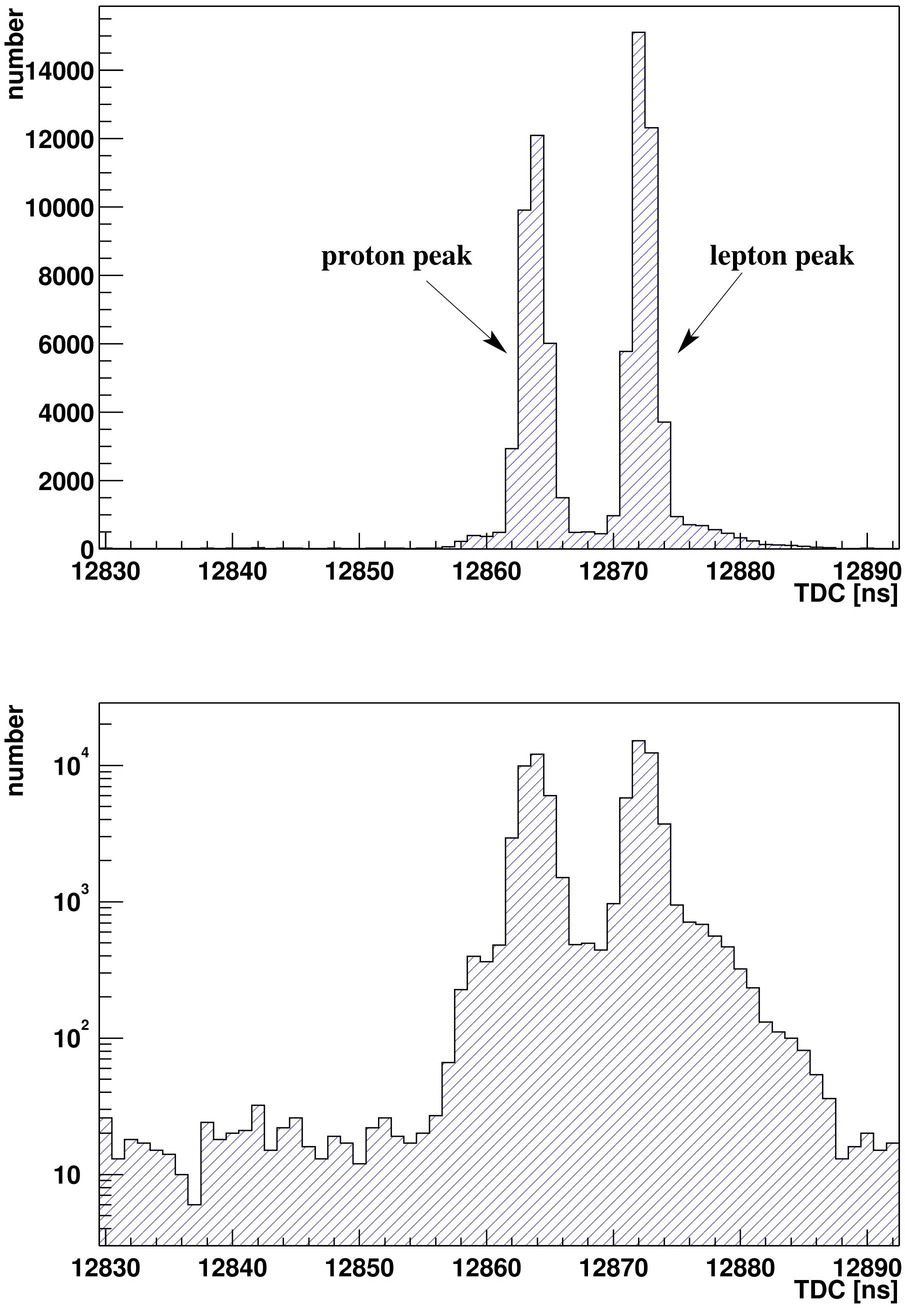


Figure 4.5: The multi-hit TDC profile, linear and logarithmic scales

#### 4.2.1.3 Offline analysis of the C5 information

It is interesting to note that the C5 data acquisition system is independent from the ZEUS Run Control, i.e. data is taken even when the ZEUS experiment is switched off. On the other hand the C5 data is not in the usual ZEUS data flow, therefore C5 has got its own system of data and histogram logging.

The most frequent offline usage of the C5 rate information is to estimate particle background contribution inside the ZEUS detector, for electron and proton beams separately. For example, the particle background contribution inside the central tracking detector can be derived from the C5 rate information.

It is not so straightforward to measure the quality of the beampipe vacuum inside the ZEUS detector. The C5 rate is directly dependent on the quality of the vacuum itself. At the same proton and electron beam currents, the C5 rate is lower if the vacuum is better. In this way, the vacuum trend inside the detector is monitored continuously.

### 4.2.2 Application of the C5 data

The C5 time information has been widely used to analyse the properties of HERA beams, i.e. to monitor the stability of the bunch arrival times, the C5 $z$-vertex and the contribution of satellite bunches. The first studies of the post-upgrade running period of the HERA II show no signifficant contribution from the satellite bunches to the main luminosity.

In the past, the C5 time spectra have served to provide a correction to the ZEUS luminosity during a period when the electron satellite bunches were large [38], to correct F/RCAL timing measurements for drifts in the HERA clock, to generate a ZEUS- trigger-independent estimation of $z$-vertex over the running period and to study the short- and long-term behaviour of the proton satellite bunches [39].

The C5 coincidence signals are sent to the ZEUS Glogal First Level Trigger. The arrival of the signal is digitized by TDC and subsequently used as a *timing veto* to reject beam-gas interaction.

In addition, the ZEUS GFLT uses a precise C5 time fitting result, described in Section 4.2.1.2, to adjust global ZEUS-online timing relative to the HERA proton clock. Deviations of more than 1 $ns$ from the nominal ZEUS-online timing result in a substantial ZEUS data acquisition problem and the data acquisition chain of the detector becomes unstable.

The C5 time fitting information is saved on run-by-run basis in the ZEUS run-summaries. This info is used as a trigger-independent crosscheck of the interaction $z$-vertex obtained from tracking devices at Third Level Trigger.

# CHAPTER 5
# EVENT MODELING AND UNFOLDING OF DETECTOR EFFECTS

The complexity of the outgoing particle systems from an *ep* interaction and of the detector itself is such that it is impossible to calculate analytically the full detector response.

*Monte Carlo* (MC) generators are used to simulate complex high energy physics processes, as well as the detector response on the basis of statistical methods. The MC procedure uses a physics event generator to model the underlying physics process. The outcome are 4-momenta of all outgoing particles. In the next step the information is passed to the detector simulation resulting in the detector response. For the ZEUS detector, the output format of the simulation is of the same format as the real data. The advantage of this approach is that the same event reconstruction and physics analysis chain can be used for data and MC events.

This chapter describes the simulation of physical processes considered in this study and a brief description of the detector simulation. Emphasis is put on the simulation of background processes, while the detailed description of the simulation of signal processes will be presented in the corresponding chapters. Because the thesis describes a search for rare SM and possible non-SM signals at HERA, the physical background could come from all SM processes with signifficant cross sections.

## 5.1 General considerations: QCD cascade and hadronisation

As presented in Chapter 2, QCD describes interactions between partons, quarks and gluons, but in the detector only colourless hadrons can be measured while the partons are confined inside the hadrons. There is lack of knowledge how partons are organised into colourless hadrons. Moreover, the parton density functions, PDFs, cannot be calculated from first principles of QCD, but have to be extracted from experiments and then can be evolved according to the QCD knowledge.

To be able to test the parton dynamics, it is obvious that we have to parametrise the ignorance and the complexity of the hadronic system in such way that the corrections to the parton level are the smallest possible. Once the parton dynamics is well known, one could turn the arguments around and learn more about quark confinement, hopefully.

Therefore, every MC simulation consists of two major parts. The first part is the *hard subprocess* which describes the calculable parton interactions and determines the main characteristics of the event. The second part deals with problems described above, namely with multiple parton emissions in QCD (so called *QCD cascade*) and with confinement effects, i.e. with *hadronisation* (*fragmentation*).

To take into account the initial and final state photon (general electroweak) radiation is not as difficult as parton radiation and is usually a standard part of the simulation process and will not be presented here.

This section contains a brief description of the common approaches how to handle QCD cascade and hadronisation.

### 5.1.1 QCD cascade

There are two main approaches how to deal phenomenologically with multiple parton emissions in QCD.

*Colour Dipole Model* (CDM). In the Colour Dipole Model QCD cascade is described as parton radiation from independently radiating colour dipoles [40], see Fig. 5.1, where the CDM diagram for $e^+e^-$ interactions is shown. In *ep* scattering, the first dipole is spanned by the quark struck by the photon and the remaining proton constituents (*proton remnant*) and that dipole radiates a gluon. Then the emission of a second (softer) gluon is treated as radiation from two independent dipoles, one between the struck quark and the first gluon, the other between that gluon and the proton remnant. Subsequent, even softer gluon emission is the result of radiation of more dipoles.

A conservative estimate of the uncertainty associated to the CDM treatment of the QCD cascade can be obtained by using different models as a systematic check.

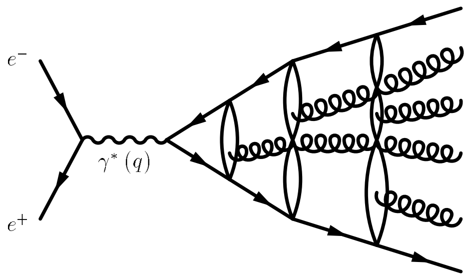


Figure 5.1: Schematic representation of the Colour Dipole Model for the simulation of the parton cascade for $e^+e^- \to q\overline{q}$ process. The parton radiation is generated by colour dipoles defined between the partons present in each step.

*Matrix Element Parton Shower Model* (MEPS). In this model QCD radiation (corresponding to higher orders in perturbation theory) is completely summed up using the, so called, DGLAP leading log approximation (LLA). A parton shower is generated in which the splitting processes are determined from the Altarelli-Parisi splitting functions [19] that govern the DGLAP evolution equation. The process is schematically depicted in Fig. 5.2., for the *ep* scattering case.

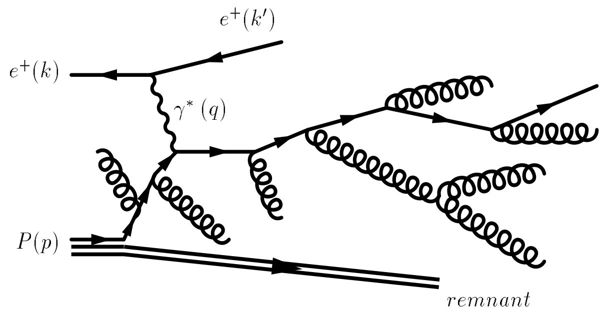


Figure 5.2: Representation of the parton shower approach to the simulation of the parton cascade. The partons are generated by succesive splittings.

### 5.1.2 Hadronisation

After the treatment of the QCD cascade the final part is the transformation to colourless hadrons, i.e. hadronisation or fragmentation. Two commonly used hadronisation models are *Lund string model* and *Cluster fragmentation model*.

The Lund string model [41] uses standard assumption of linear confinement. Namely, as $q$ and $\bar{q}$ move apart the colour field between them is treated as a string of constant energy density ($\sim 1\ GeV/fm$), which serves as a parametrisation of self-interactions of the gluons. The constant energy density results in an increasing string energy with growing $q\bar{q}$ distance until a critical energy is reached when the vacuum gets seriously restructured and a new $q\bar{q}$ pair is created. The string keeps breaking into smaller parts until the initial $q\bar{q}$ pair energy is exhausted. When considerd in detail, the string fragmentation is complicated by the appearance of additional string regions during the time evolution of the system and with the possibility to create *baryons*, as well.

The cluster fragmentation model [43] uses the idea of preconfinement of colour [44]. In this model colour singlet clusters of partons are formed after the parton branching. Colour singlet clusters are formed via non-perturbative splittings of gluons into $q\bar{q}$ pairs [45]. Neighbouring quarks and antiquarks can then combine into colour singlets. The final state hadrons are then products of colour singlet cluster decays or momentum readjustments between clusters to get correct hadron masses.

## 5.2 Simulation of photoproduction processes (PhP)

As explained in the Chapter 2, it is very likely that a photon with $Q^2 \approx 0$ $GeV^2$ will develop a complicated structure which then interacts with the proton. To be able to simulate the PhP process in an efficient way, PhP is devided in a *direct* and a *resolved part*. In the direct process the exchanged photon participates in the hard scattering whereas in the resolved part it acts as a source of partons. It is necesary to stress the fact that such a division is largerly ambiguous, i.e. a resolved process in the lowest order of the perturbative QCD expansion can easily be a direct process in the next order, depending on a definition of the hard scattering in the higher order case. The PhP MC simulations used in this analysis always refer to the direct and resolved processes in the lowest order of the QCD expansion (called *Leading Order* (LO)).

The generator HERWIG [46], version 5.9, was used to simulate both direct and resolved PhP. The proton parton density function was CTEQ4D [47] and the photon PDF was GRV-G LO [48]. LO matrix elements have been used to simulate partonic processes, including initial- and final-state parton showers. The hadronisation model used is the cluster fragmentation model. The samples considered were restricted at the generator level in the transverse energy of the produced hadronic system, $E_T$, or in the individual transverse momentum of the produced hadrons , $p_T^{hadron}$, depending on the requirements of the particular analysis. Specific cut values were different for isolated $\tau$ search and for di-$\tau$ analysis, and will be quoted in the corresponding chapters.

## 5.3 Neutral and charged current deep inelastic scattering

The event generator DJANGOH 1.1 [49] was used to simulate neutral current DIS processes. The DJANGOH event generator containes the HERACLES [50] package which simulates electroweak corrections to the hard process simulated with the LEPTO 6.5 [51] generator. The LEPTO program is based on the LO electroweak cross sections for the underlying parton level scattering, and includes QCD corrections using exact first-order matrix elements. The choice of proton density functions, PDFs, was CTEQ5D [52]. The colour dipole model (CDM) was used to simulate the QCD cascade incorporated in the ARIADNE [53] program. To astimate the uncertainty introduced by QCD cascade model another sample of NC DIS events was generated using Matrix Element and Parton Shower Model (MEPS), implemented in LEPTO MEPS program. The Lund string model was chosen as fragmentation (hadronisation) model.

The charged current DIS background events were simulated in the same way as NC DIS sample, using CTEQ4D PDF [47].

## 5.4 Detector simulation

To be able to compare the simulated events with the measured data, the generated MC events were put through a simulation of the ZEUS detector. The package MOZART simulates the response of different detector components taking into consideration full geometry and inactive (dead) material. MOZART is based on the GEANT [54] package and was tuned with testbeam data for each of the detector components. It is constantly improved with studies of the running ZEUS experiment. After detector simulation, the events are passed to the simulation of the ZEUS three level trigger called ZGANA. The same ZEPHYR program is used for the event reconstruction for both MC and real data events resulting in the same format for real data and MC simulation. ZEPHYR contains the event reconstruction routines of the different detector components. Physics objets, for example tracks, are built from the event information after the calibration corrections were applied.

## CHAPTER 6
## EVENT RECONSTRUCTION AND DEFINITION OF VARIABLES

The chapter contains a description of the event reconstruction and definitions of event and jet variables used in the following chapters.

### 6.1 Calorimeter variables

The calorimeter cells taken into account for the reconstruction had to contain energy depositions above a noise threshold of 80 $MeV$ for electromagnetic cells and 140 $MeV$ for hadronic cells.

To improve the accuracy of the energy scale, the energy measured by the electromagnetic and hadronic parts of the three CAL sections were calibrated applying correction factors to the energy measurements of all CAL cells of the corresponding section and cell type [80][1]. The remaining uncertainty on the CAL energy measurement was $\pm 1\%$ for the FCAL and BCAL and $\pm 2\%$ in the RCAL [79].

The total energy deposition in the calorimeter can be organized in the a CAL 4-vector defined as:

$$E = \sum_i E_i,$$

$$p_x = \sum_i E_i sin\theta_i cos\theta_i,$$

$$p_y = \sum_i E_i sin\theta_i sin\theta_i,$$

$$p_z = \sum_i E_i cos\theta_i.$$

The index $i$ runs over all CAL cells not associated to identified muons. $E_i, \theta_i, \phi_i$ are the energy, polar angle and azimuthal angle of the $i$-th CAL cell. The CAL 4-vectors were corrected for energy losses in inactive material in front of the calorimeter sections, for the CAL back-splash and for non-uniformity in the energy response of the calorimeter cells. The hadronic system and identified electrons were treated separately and added to form the total CAL 4-vector.

The total transverse energy is calculated as:

$$E_T^{CAL} = \sum_i E_{T,i} = \sum_i E_i \cdot sin\theta_i.$$

[1] The following corrections were applied: FEMC +4%, FHAC −5%, BEMC +4%, BHAC +8% and RCAL (both EMC and HAC) +2.5%.

The total energy minus the longitudinal component of the CAL 4-vector, $E-p_z$, is defined as:

$$E - p_z = \sum_i E_i(1 - cos\theta_i).$$

The energy and momentum conservation laws require the $E-p_z$ value to be 55 $GeV$, i.e. twice the energy of the incoming lepton beam, if only undetected particles escape only through the forward detector beampipe at $\theta = 0$.

The conservation laws require, also, that the vector of detector transverse momentum, $\overrightarrow{p_T^{CAL}} = (-p_x, -p_y, 0)$, should have magnitude close to zero, if all final state particles are detected except particles that escaped through the beampipe in both forward and rear directions. CC DIS events, where a neutrino escapes undetected, are characterised by the imbalance of the detector transverse momentum. The magnitude of the $\overrightarrow{p_T^{CAL}}$ vector is defined as:

$$p_T^{CAL} = \sqrt{p_x^2 + p_y^2}.$$

$p_T^{ex1IR}$ is the imbalance of the detector transverse momentum calculated without the contributions from the CAL cells that belonging to the first inner ring of the FCAL. The $p_T^{ex1IR}$ value for this study was not corrected for energy losses in inactive material in front of the calorimeter sections, for the CAL back-splash and for non-uniformity in the energy response of the calorimeter cells.

The same definition as for the CAL 4-vector was used to calculate the 4-vector of the hadronic system, except that cells belong to identified electrons were excluded from the calculation:

$$E_{had} = \textstyle\sum_{i \neq el.cells} E_i,$$

$$p_{x,had} = \textstyle\sum_{i \neq el.cells} E_i sin\theta_i cos\theta_i,$$

$$p_{y,had} = \textstyle\sum_{i \neq el.cells} E_i sin\theta_i sin\theta_i,$$

$$p_{z,had} = \textstyle\sum_{i \neq el.cells} E_i cos\theta_i.$$

The transverse vector of the hadronic system and its magnitude are defined as $\overrightarrow{p_T^{had}} = (-p_{x,had}, -p_{y,had}, 0)$ and $p_T^{had} = \sqrt{p_{x,had}^2 + p_{y,had}^2}$, respectively.

## 6.2 Track and vertex reconstrucion

Tracks were reconstructed from hits in the CTD [55]. The reconstructed tracks from CTD were used to calculate the position of the event vertex. The track quality requirements applied for particular studies will be presented in the following chapters. The track charges were determined from the sign of the track curvature. No selection based on the charges of the tracks were applied.

### 6.3 Electron and muon identification

The identification of electrons was based on the electron finder EM [56] for isolated $\tau$ study and on the Sinistra95 [57] finder for di-$\tau$ analysis. The electron identification was used to reject the tracks associated to the identified electrons for both studies.

EM calculates the likelihood for different variables to be originating from an electron. For EM electron candidates in this analysis, the product of the different likelihoods had to exceed a value of $10^{-3}$. The electron energy was calculated from the corrected depositions in the calorimeter. The direction of EM candidate was determined from the CTD track pointing into the direction of the electron candidate. The minimum electron energy required was 4 $GeV$ and only isolated electrons were considered: the energy not belonging to the electron candidate, within a cone of radius 0.8 in the $(\eta, \phi)$ plane around the candidate, was required to have less than 20% of the energy belonging to the electron candidate. $\eta$ is the pseudorapidity defined as:

$$\eta = -ln\ tan(\theta/2).$$

Sinistra95 is a neural network based program which combines neighbouring energy deposits into islands and subsequently converts these islands into a probability for being a positron by analysing the calorimeter shower shapes. The probability varies from zero (cluster of hadronic origin) to one (cluster stems from positrons). The CTD information was used to increase the purity of the finder, if an electron candidate was within CTD acceptance. For the di-$\tau$ study, identified electrons were required to have the Sinistra95 probability greater or equal to 0.95.

The muon identification algorithm matches vertex fitted CTD tracks ($p_T^{trk} > 2$ $GeV$) with energy deposition in the calorimeter. The energy deposition was required to be compatible with the energy deposition of a *minimum ionizing particle* (MIP). Tracks that had a distance of less than 30 $cm$ to the MIP were classified as muons, if there were no other tracks within the 100 $cm$ distance from the muon candidate. The CTD track information was used to calculate kinematic parameters of the muon candidate.

## 6.4 Jet finding algorithm

The energy depositions in the calorimeter cells were combined to jets in the $(\eta, \phi)$ plane of the laboratory reference frame with the inclusive $k_T$ cluster algorithm [115, 116]. The energy deposition in the CAL cells that were combined to jets was required to exceed 100 $MeV$ for electromagnetic and 150 $MeV$ for hadronic cells, respectively.

The $k_T$ cluster algorithm implies the following steps:

1. For every object $i$ (here, CAL cell) its distance from the direction of the proton beam was calculated as $d_i = E^2_{T,i}$
2. For every pair of objects the distance between them was evaluated as: $d_{ij} = min[E^2_{T,i}, E^2_{T,j}] \cdot ((\eta_i - \eta_j)^2 + (\phi_i - \phi_j)^2)$
3. If the smallest of all the $d_i$ and $d_{ij}$ quantites was a $d_{ij}$, the objects $i$ and $j$ were recombined into a new object $k$ folowing the $E_T$ recombination scheme:
$$\begin{aligned} E_{T,k} &= E_{T,i} + E_{T,j}, \\ \eta_k &= \frac{E_{T,i} \cdot \eta_i + E_{T,j} \cdot \eta_j}{E_{T,i} + E_{T,j}}, \\ \phi_k &= \frac{E_{T,i} \cdot \phi_i + E_{T,j} \cdot \phi_j}{E_{T,i} + E_{T,j}}. \end{aligned}$$
4. If the smallest of all the $d_i$ and $d_{ij}$ quantites was a $d_i$, the object $i$ was defined as a protojet and was no longer merged. This protojet was removed from further clustering.
5. The procedure was repeated for the remaining particles until none is left.

Jets were all the protojets with transverse energy above the $E_T^{jet} > 5\ GeV$ threshold. The jet transverse energy, $E_T^{jet}$, and the $\eta_{jet}$ and $\phi_{jet}$ variables were defined as:
$$\begin{aligned} E_T^{jet} &= \textstyle\sum_i E_{T,i} = \sum_i E_i sin\theta_i, \\ \eta_{jet} &= \frac{\Sigma_i E_{T,i} \cdot \eta_i}{\Sigma_i E_{T,i}}, \\ \phi_{jet} &= \frac{\Sigma_i E_{T,i} \cdot \phi_i}{\Sigma_i E_{T,i}}. \end{aligned}$$
where the sum runs over all cells associated to the jet.

## 6.5 Jet energy corrections

A jet measured in the calorimeter has a transverse energy that is different from that at the hadron level. Jets measured in the calorimeter usually have smaller transverse energies $E_T^{jet}(CAL)$ than the "true" values $E_T^{jet}(had)$ of the outgoing set of hadrons. This energy loss is due to dead material in front of the calorimeter and due to particles that do not deposit a significant amount of energy in the calorimeter, such as muons and neutrinos. The transverse jet energy as measured by the CAL was, therefore, corrected for these effects.

The transverse jet energies were corrected on the basis of simulated CC DIS MC sample. For the considered MC sample, the jet reconstruction was performed on the CAL cells and on the hadronic final state as obtained from the simulation. A correction factors were obtained for each jet of the reference sample from the difference between the jet transverse energy reconstructed from the hadronic final state and jet transverse energy reconstructed from the CAL cells. Obtained correction factors as a function of the pseudorapidity $\eta_{jet}$ and transverse energy $E_T^{jet}$ of the jet were used to correct the jet energies for all data and MC simulation samples.

The energy correction procedure was the same as described in [58, 59, 60], and the correction factors applied were largely inherited from these studies.

After the corrections were applied, the remaining discrepancies between the reconstructed jet energies from the CAL cell information and the jet energies reconstructed from the simulated hadronic final state were below 2% for the whole $\eta_{jet}$ and $E_T^{jet}$ range considered.

# CHAPTER 7
# ISOLATED $\tau$ LEPTONS AND LARGE MISSING TRANSVERSE MOMENTUM

Isolated leptons produced together with large missing transverse momentum are spectacular signatures and rare in the Standard Model. At the HERA *ep* accelerator a decay of $W^{\pm}$ bosons into lepton and associated neutrino, the $W^{\pm}$ being radiated from the quark or the beam lepton, is the only significant SM source of such events. A possible observation of a deviation (excess) from the SM prediction would be striking evidence for physics beyond the SM.

Previous searches in the electron and muon channel performed by the H1 and ZEUS Collaborations [3, 4, 5] are quite puzzling. Namely, for events with a large hadronic transverse momentum produced in addition to an isolated lepton and missing transverse momentum, where the SM background is suppressed, the H1 results show an excess in the number of observed events while the ZEUS findings are in agreement with the SM.

This chapter presents a search for isolated $\tau$ leptons and missing transverse momentum using ZEUS data. The results have been published by ZEUS in [6].

## 7.1 Production of isolated leptons in events with large transverse momentum at HERA

Within the SM single $W^{\pm}$ decay is the dominant source of events with isolated $\tau$ leptons and large transverse momentum which does not originate from the $\tau$ decay. Opposite to leptons that originate from semi-leptonic heavy quark decays, for example, the leptons originating from single $W^{\pm}$ decays are well isolated from other tracks and jets, typically.

A possible source, beyond the SM, of such a signature would be the production of single top quarks via flavour changing neutral currents (FCNC), with subsequent decay $t \rightarrow bW^{+}$, predicted by some theories beyond the SM [61] or $R$-parity ($R_p$) violating stop quark production and subsequent decay. These production mechanisms will be described in more detail.

### 7.1.1 Single $W^{\pm}$ boson production and subsequent leptonic decays

Two reactions contribute to the SM single $W$ boson production at $ep$ colliders:

$$ep \to eWX \text{ and } ep \to \nu WX$$

where $X$ stands for the hadronic final state [65]. The second, charged current like, reaction involves an extra $W$ boson propagator connected to the initial beam lepton and is therefore suppressed. Its contribution to the total cross section is about 5%. In the following considerations this process will be ignored.

The dominant contribution of the first, Neutral Current like, reaction comes from the photoproduction of the real $W$ boson, depicted in Fig. 7.1 a) and b).

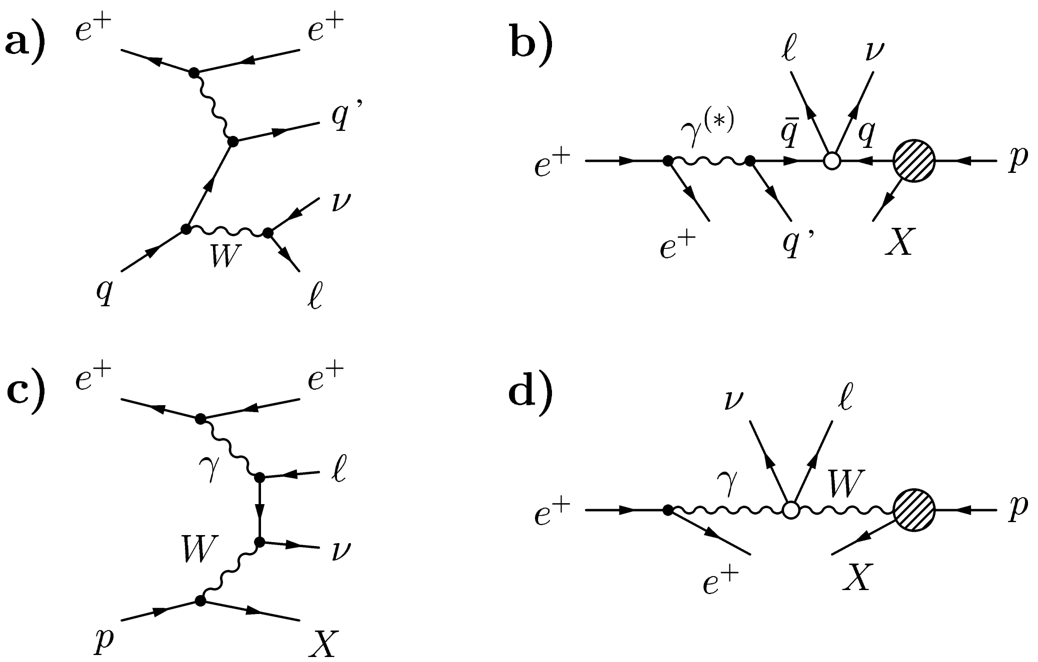


Figure 7.1: The schematic view of the lepton+neutrino production at HERA. The single $W$ boson production via radiation from the quark line a), is dominated by photoproduction as depicted in b). The $l\nu_l$ pair can be produced also in a $t$-channel fermion exchange between two bosons $\gamma$-$W$, as sketched in c). This corresponds to boson-boson fusion, diagram d).

The photon entering the reaction from the electron side, see Fig. 7.1 b), is quasi-real ($Q^2 \simeq 0$) and fluctuates into a $q\bar{q}$ pair. The $W$ boson is then produced in a $q\bar{q}$ fusion between a quark coming from the photon and another quark with different flavour originating from the proton. Due to the $q\bar{q}$ head-on hard scattering, the transverse momenta of the proton and photon remnants are typically small and therefore the transverse momentum of the hadronic final state is expected to be quite small [66].

When the photon virtuality is large ($Q^2 \gg 0$), the DIS $W$ boson production proceeds via a $W$-strahlung from the quark line. In this case the scattered beam electron is visible in the detector together with the charged lepton originating from the $W$ boson decay. The hadronic system $X$ can acquire substantial transverse momentum. This topology contributes approximately 25% to the total cross section in the detector.

The production of an isolated lepton and missing transverse momentum in boson-boson ($\gamma, Z$-$W$) fusion is shown in Fig. 7.1 c) and d). The process contains an off-shell $W$ particle. Boson-boson fusion events do not show a mass peak in the lepton-neutrino invariant mass distribution. This production channel contributes about 5% to the total cross section. $W$ bosons can also be produced by a triple boson coupling $\gamma WW$, via $\gamma$-$W$ fusion. A $W$ cross section measurement therefore allows for the probing of possible anomalous $\gamma$-$W$ couplings.

A complete leading order (LO) QCD calculation of $W$ boson production in $ep$ scattering can be found in [65]. An event generator EPVEC, based on this calculation, was used to simulate $W$ boson processes. The QCD parton shower simulation in the final state is included in the EPVEC Generator [67]. The hadronisation is simulated using the Lund string model [41] as implemented in the JETSET 7.3 program [42].

Recently, a next to leading order (NLO) QCD calculation [68] in the framework of the EPVEC Generator [65] has been performed.

To account for the difference between LO and NLO, $W$ boson events generated by EPVEC program were weighted by a factor dependent on the transverse momentum and rapidity of the $W$ particle [69], such that the resulting production cross section corresponds to the NLO calculation [71]. The reweighting was performed to obtain the final SM $W$ contribution to the isolated $\tau$ search. As will be explained in Section 7.3, one of the selection requirements was at least one jet in the detector with $E_T^{jet} > 5\ GeV$ in addition to the high $p_T^{jet}$ associated to the hadronically decaying $\tau$ lepton. This requirement favors $W$ boson production with significant transverse momentum, $p_T^W$. For $p_T^W > 10\ GeV$, NLO QCD corrections modify the corresponding LO cross section by about $\pm 10\%$ at the nominal renormalisation/factorisation scale $\mu_R = \mu_F = M_W$ [68]. The remaining theoretical uncertainty on the $W$ production cross section is reduced to 15% (30% at leading order). The improvement is mainly due to the significantly reduced scale dependence (from $\approx$ 20% (LO) to $\approx$ 5% (NLO), where the scale was varied from $0.5M_W$ to $2M_W$).

The total predicted single $W$ cross section reaches 1.1 $pb$ for $\sqrt{s} = 300$ $GeV$ and 1.3 $pb$ for $\sqrt{s} = 318$ $GeV$ [66].

The study was designed to search for events coming from the decay of a heavy particle. The FCNC production of single top quarks, with subsequent decay $t \to W^+b$, was used as a template process. The event topologies of the selected data and MC events will be given and discussed in more details in Sections 7.4 and 7.6.

### 7.1.2 Single top quark production beyond the SM

At the HERA collider top quarks can be only singly produced due to the energy available. In the SM, single top quarks are produced through charged current reaction $ep \to \nu t\bar{b}X$ [73]. The SM cross section at HERA is less than 1 $fb$ [74]. Therefore any observed single top event in the present data sample can be associated to physics beyond the SM.

*Flavour changing neutral current* (FCNC) single top production, see Fig. 7.2, is predicted by many theories beyond the SM [61].

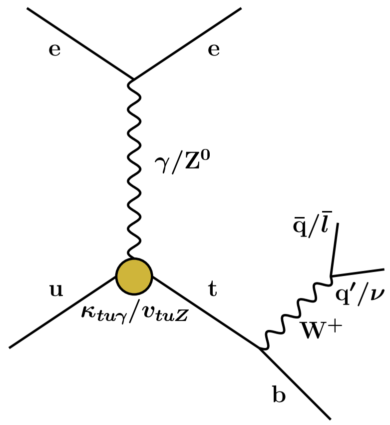


Figure 7.2: Single top quark production by FCNC process in $ep$ scattering and subsequent SM top decay $t \to W^+b$.

In the single top case, the large mass of the top quark usually leads to a large hadronic transverse momentum in the detector through the $b$ quark decay, in addition to the large missing transverse momentum. For single $W$ boson production and decay one does not expect a large hadronic transverse momentum in SM events, typically. In the following considerations the anomalous production of single top quarks is used as a template for processes involving the production of heavy particles with $\tau$ lepton as one of decay products.

Single top production through flavour changing $\gamma$ and $Z^0$ exchange in $ep$ collisions at HERA was simulated using the HEXF generator [62, 71]. HEXF is based on the phenomenological model of Hagiwara et al. [63] for fermion compositeness. An excited $u^*$ quark with a mass of 175 $GeV$ was produced and forced to decay into $b$ and $W$. The matrix element and parton shower model as implemented in Lepto 6.1 [51] was used to simulate the QCD cascade. The fragmentation model was the Lund string model [41] simulated using JETSET the 7.4 program [42].

### 7.1.3 Possible supersymmetric scenario

One of appealing extensions of the Standard Model is *Supersymmetry* (SUSY). It is beyond the scope of this thesis to enter into the rich subject of SUSY, but large parts of the SUSY parameter space allow for a number of different processes that could result to isolated leptons produced together with large missing transverse momentum.

In particular, not yet excluded regions of the SUSY parameter space give enhanced $\tau$ couplings as compared to other leptons, which might result in enhanced isolated $\tau$ production. As mentioned, previous isolated muon and electron searches performed by the ZEUS Collaboration are in agreement with the SM expectation. Creation of stop quark in $R_p$ violating SUSY models [64] with subsequent two-body decay ($\tilde{t} \to \tau b$) or $R_p$-conserving three-body decay channels ($\tilde{t} \to \tau \tilde{\nu_\tau} b$, $\tilde{\tau} \nu_\tau b$) are potential sources of events with isolated $\tau$ leptons and large missing transverse momentum.

SUSY processes have not been considered in detail as a possible source of signal events. However, after a discussion of the kinematic properties of the found events with $\tau$ candidate, particular SUSY processes which could lead to the signal topology are given in the summary of this chapter.

## 7.2 $\tau$ identification

The mean lifetime of the $\tau$ lepton $t = (290.6 \pm 1.1) \cdot 10^{-15}$ $s$ [113] leads to a decay length of $ct = 87$ $\mu m$ which is below the 3-$D$ vertex resolution of the central

| Decay Mode | BR |
|---|---|
| $\tau^- \rightarrow e^-\bar{\nu_e}\nu_\tau$ | 17.8% |
| $\tau^- \rightarrow \mu^-\bar{\nu_\mu}\nu_\tau$ | 17.4% |
| $\tau^- \rightarrow had^-\nu_\tau \geq 0\ neutrals$ | 49.5% |
| $\tau^- \rightarrow 2had^-had^+\nu_\tau \geq 0\ neutrals$ | 15.2% |
| $\tau^- \rightarrow 3had^-2had^+\nu_\tau \geq 0\ neutrals$ | 0.1% |

Table 7.1: The major decay modes of $\tau^-$ lepton and the associated branching ratios [113]. The $had^\pm$ label indicates a charged hadron and label *neutrals* neutral hadrons. The branching ratios of $\tau^+$ decay agree with the branching ratios quoted, for the given accuracy.

tracking detector (CTD) ($< 2\ mm$) used for this analysis. With newly installed silicon microvertex detector (MVD), capable of measuring impact parameters of about 100 $\mu m$ [26, 27], it might be just possible to tag secondary vertices associated to $\tau$ lepton decays at HERA II program.

In this thesis, a multi-observable discrimination method is used to distinguish between hadronic $\tau$ lepton jets and quark- and gluon-induced jets. This section presents a detail description of the $\tau$ technique, as well as its verification based on a sample of neutral current deep inelastic scattering (NC DIS) events. The $\tau$ identification method is an essential ingredient of the whole study described in this thesis.

### 7.2.1 $\tau$ lepton properties

The $\tau$ lepton was discovered at the SPEAR collider, the *Stanford Linear Accelerator Center* (SLAC), 1975 [75]. The study of its decay implied the existence of the associated neutrino, $\nu_\tau$. The rest mass of $M_\tau = 1777.03^{+0.30}_{-0.26}\ MeV$ (world average [113]) is almost twice the nucleon mass and significantly heavier than the rest mass of a pion ($M_\pi = 139.67018 \pm 0.00035\ MeV$), the lightest known hadron. Therefore, opposite to the electron and muon leptons, a $\tau$ can decay into hadrons which is exploited by the $\tau$ identification technique presented here. The major decay modes and associated branching ratios are given in Table 7.1.

If an isolated $\tau$ particle decays into electron or muon, the corresponding event topology is hard to distinguish from the direct production of isolated electrons and muons. Hence a distinction is usually not made and leptonic decays of isolated $\tau$ leptons enter directly into searches for isolated electrons and muons [5]. As can be seen from Table 7.1, the branching ratio of the $\tau$ particle into one charged hadron ($\pi^{\pm}$ or $K^{\pm}$) and zero or more neutral ones is 49.5% and is of importance for the $\tau$ tagging described in this thesis.

The hadrons emerging from a decay of $\tau$ leptons can be measured with the ZEUS calorimeter as hadronic jets. If the $\tau$ lepton is produced with a high momentum, which is certainly true for the isolated $\tau$ production mechanisms considered, the decay particles will have a direction very close to the $\tau$ lepton. The colour neutrality of the $\tau$ particle is expected to inhibit QCD radiation in the final state and emerging decay particles are expected to have a narrow, pencil-like, energy deposition in the calorimeter. The other expected characteristics of the $\tau$ decays are: low charged particle multiplicity, total charge of $\pm 1$ and presence of a secondary vertex in the event. On the other hand, standard QCD jets originating from coloured quarks or gluons are expected to be far less collimated with a different signature in the calorimeter, due to the gluon radiation in the final state, see Fig. 7.3.

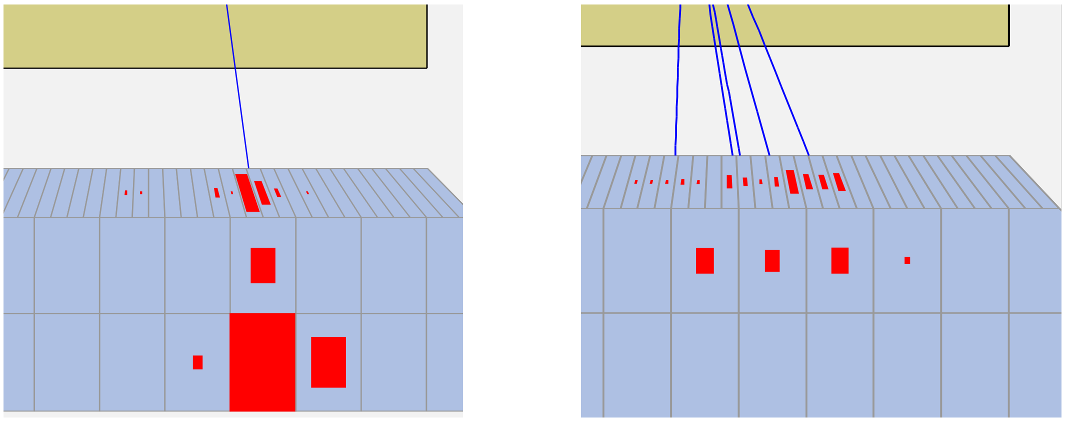

**a)** **b)**

Figure 7.3: An event display [114] of the response of the ZEUS tracking system and calorimeter to a) a tipical 1-prong (1 charged particle) $\tau$ hadronic jet from $W \to \nu_\tau \tau$ simulation and b) a standard QCD jet obtained from simulated photoproduction process.

### 7.2.2 Multi-observable discrimination method

To discriminate $\tau$ lepton induced jets from QCD induced jets is the challenge of this study. For this purpose a multi-observable discrimination technique, introduced in [76, 78], was used. The method is developed for the case when the expected signal is very small in comparison to the expected background.

In order to separate a signal (wanted feature in general) from a large background (unwanted feature in general), the first step is to select a number of quantities which have an as high as possible signal-to-background discrimination power. Each of these quantities can be imagined as a coordinate of the phase space in which the signal and background happenings[1] are distributed. Assuming there are $n$ discriminating quantities, any point in the phase space is caracterised by the $n$-vector $\vec{\mathbf{x}} = (x_1, ..., x_n)$. The probability that the phase space point $\vec{\mathbf{x}}$ is of signal type can be characterised by the *discriminant* $D(\vec{\mathbf{x}})$, written as

$$D(\vec{\mathbf{x}}) = \frac{\rho_s(\vec{\mathbf{x}})}{\rho_s(\vec{\mathbf{x}}) + \rho_b(\vec{\mathbf{x}})}, \tag{7.1}$$

where $\rho_s$ and $\rho_b$ are the signal and background density functions, respectively. Therefore, each phase space point can be classified according to the discriminant value $D$ associated to it. It is obvious from the definition that $0 \leq D(\vec{\mathbf{x}}) \leq 1$ and that the high discriminant values correspond to the signal region while the low discriminant values caracterise the background.

The discrimination technique estimates the density functions in the vicinity of the point $\vec{\mathbf{x}}$, the vicinity being a small box of fixed size in the phase space around the point $\vec{\mathbf{x}}$, and calculates the discriminat $D(\vec{\mathbf{x}})$. The signal and background density functions can be estimated by the ratio of the number of happenings in the small box over the total number of happenings in the whole phase space for signal and background, respectively. If the total number of happenings is large and if the total number of signal happenings is equal to the total number of background happenings, using Eq. 7.1, it is straightforward to see that the discriminant $D$ is equal to the ratio of the number of signal over the number of total happenings in the small box. Figure 7.4 ilustrates the calculation of $D$ for a 2-dimensional phase space.

As can be seen from the 2-dimensional example, it is crucial to ensure dense population of the phase space with both signal and background happenings. In addition, it is necessary to adjust box sizes such that for any point to be classified

[1]For this study the happening corresponds to the jet, but can be any other subject of interest.

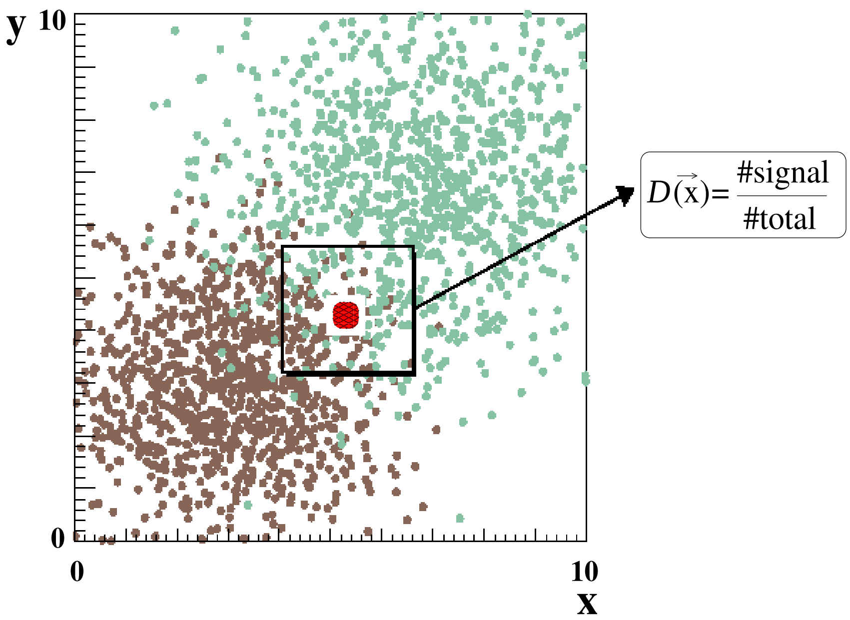


Figure 7.4: Example of a 2-dim phase space (x,y). The green (light) dots represent, say, the signal happenings and brown (dark) dots represent the background. If the point in the highlighted box has to be classified, i.e. the discriminat $D(\vec{\mathbf{x}})$ has to be calculated, $D(\vec{\mathbf{x}})$ is just a ratio of the number of signal happenings over the total number of happenings in the box.

there are enough signal and background happenings in the box to have a reasonably small uncertainty on $D(\vec{\mathbf{x}})$ and that a precise mapping of the density functions onto boxes is achieved.

A technical challenge of the technique is to have a fast algorithm to count the number of happenings in the multi-dimensional box when the total number of happenings is large. The algorithm chosen is based on the range searching [76, 77]. A binary tree structure was used to store the information about quantities used to calculate the discriminant for the signal and background samples.

The multi-observable discrimination technique automatically takes into account corellations between different observables and the only free parameters of the method are the box sizes. For studied examples, the presented method performs as good as *artificial Neural Networks* [76] with respect to the quality of selection. The optimisation phase is usually shorter for this technique than the optimisation time of artificial Neural Networks [76]. The calculation is straight forward and needs less computation time and less human intervention than artificial Neural Networks. This allows to concentrate on the best combination of observables which optimally separates the signal from background, i.e. to concentrate on the "physics" of the problem. However, large samples of reference signal and background happenings are required to populate the whole phase space region for a statistically reliable discriminant estimation. If one uses the Monte Carlo simulations of certain processes as reference signal and background happenings, as for the study described in this thesis, a good description of the true process is crucially important.

### 7.2.3 $\tau$ discriminant

As mentioned, only jet shape observables were used to distinguish $\tau$ hadronic decays from quark- and gluon-induced jets, in other words only jet shape characteristics were used to calculate the isolated $\tau$ discriminant $D$.

#### 7.2.3.1 Jet observables

The longitudinally invariant $k_T$ cluster algorithm [115] was used in the inclusive mode [116] to reconstruct jets from the energy depositions in the calorimeter cells. The jet search was performed in the ($\eta$,$\phi$) plane of the laboratory reference frame, where $\eta_i$ and $\phi_i$, the pseudorapidity and azimuthal angle of each calorimeter cell, were obtained using the primary event vertex as reconstructed in the CTD. The jet axis was defined according to the Snowmass convention [117]. The jet transverse energy, $E_T^{jet}$, was corrected for detector effects such as energy losses in the inactive material in front of the calorimeter, as described in the previous chapter.

For this study, six jet observables were chosen to discriminate $\tau$ hadronic jets from quark and gluon jets:

- the first moment of the radial extension of the jet

$$R_{mean} = \langle R \rangle = \frac{\sum_i E_i \cdot R_i}{\sum_i E_i},$$

  where the sum runs over the CAL cells associated to the jet, $E_i$ is the energy of the cell $i$ and $R_i$ is defined as $R_i = \sqrt{\Delta\phi_i^2 + \Delta\eta_i^2}$, where $\Delta\phi_i$ ($\Delta\eta_i$) is the difference between the azimuthal angle (pseudorapidity) of the calorimeter cell $i$ and the jet axis;

- the second moment of the radial extension of the jet

$$R_{rms} = \sqrt{\frac{\sum_i E_i(\langle R \rangle - R_i)^2}{\sum_i E_i}};$$

- the first moment of the projection of the jet onto its axis

$$L_{mean} = \langle L \rangle = \frac{\sum_i E_i \cdot \cos\alpha_i}{\sum_i E_i},$$

where $\alpha_i$ is the angle between the cell $i$ and the jet axis;

- the second moment of the projection of the jet onto its axis

$$L_{rms} = \sqrt{\frac{\sum_i E_i(\langle L \rangle - \cos\alpha_i)^2}{\sum_i E_i}};$$

- the number of subjets ($N_{subj}$) with a $y_{cut}$ of $5 \cdot 10^{-4}$.
The subjet multiplicity identifies the number of localised energy depositions within a jet that can be resolved using a resolution criterion $y_{cut}$. The number of subjets was found by applying the same algorithm as was initially used to find jets. For the exact definition see [118, 119, 120];

- the invariant mass, $M_{jet}$, of the jet 4-vector, calculated from the cells associated to the jet. The particles of the jet were assumed to be massless.

The six variables were combined in the isolated $\tau$ discriminant $D$, to optimally separate the signal from the background, for any point, $\vec{\mathbf{x}}$, in the phase space, where

$$\vec{\mathbf{x}} = (-\log(R_{mean}), -\log(R_{rms}), -\log(1 - L_{mean}), -\log(L_{rms}), N_{subj}, M_{jet}).$$

Logarithmic observables minimize the phase space regions which are rarely populated and which could cause statistically unreliable discriminant estimation.

#### 7.2.3.2 Inclusive CC DIS control selection and $\tau$ discriminant evaluation

To obtain signal and background jet samples required to establish the $\tau$ discriminant, a control analysis largely independent of the isolated $\tau$ search was performed. Single $W^{\pm}$ Monte Carlo events, where the $W^{\pm}$ decays to a $\tau$ lepton and a neutrino and $\tau$ decays hadronically ($W \to \tau\nu_\tau, \tau \to hadrons$), were used as signal. The background simulation was based on an inclusive CC DIS Monte Carlo sample since CC DIS is a main background for events with large missing transverse momentum.

An inclusive CC DIS data sample was used to check the quality of the simulation. The $e^+p$ data taking period from 1999 to 2000, with an integrated luminosity of $\mathcal{L}_{int} = 65\ pb^{-1}$ was considered. The main selection requirement was large missing transverse momentum [79]. The online selection and the non-*ep* background rejection cuts were as in the search for isolated $\tau$ leptons and will be described in Section 7.3. The list below contains the selection criteria applied to obtain a clean CC DIS event sample. Only cuts not used in the search for isolated $\tau$ particles, described in Section 7.3, are given in more details.

- `Trigger selection`. The charged current trigger bit DST 34 selecting events with transverse momentum outside the first inner ring of the FCAL, $p_T^{ex1IR} > 7\ GeV$, was required.

- `Non-ep background rejection.`
  - calorimeter timing veto (applied for data only)
  - $|z_{vtx}| < 50\ cm$
  - $N_{tracks}^{good} > 0.2 \cdot N_{tracks} - 20$
  - cosmic event rejection (3-dim opening angle between two tracks $< 178°$)
  - cosmic event rejection by visual scanning
  - beam halo rejection (the energy deposited in the electromagnetic part of the BCAL and RCAL was required to exceed 10% of the total energy deposited in those parts of the calorimeter, if the total energy exceeded a threshold of 5 $GeV$).

- `Large missing transverse momentum requirement.`
  - uncorrected calorimeter transverse momentum, $p_T^{CAL} > 20\ GeV$
  - $p_T^{ex1IR} > 9\ GeV$

- `Photoproduction and NC DIS rejection.` A difference between CC DIS and NC DIS (photoproduction) event topology was used to suppress these types of *ep* backgrounds.
  - $\phi_{acopl}^{el} > 0.2$, where $\phi_{acopl}^{el}$ is defined as the azimuthal angle between the electron with the highest value of the transverse momentum and the vector which balances the hadronic system, see Section 6.1. For NC DIS (photoproduction) events the acoplanarity is usually small.
  - $p_T^{CAL}/E_T^{CAL} > 0.5$
  - $E - p_z < 40\ GeV$

- `Jet requirements.` Only well reconstructed jets inside the CTD acceptance were selected. Remaining electrons were rejected using jet electromagnetic energy fraction ("emfrac") and the jet energy fraction carried by the most energetic track in the jet ("ltf"). Only events with at least one jet which fulfills these requirements were considered:
  - $E_T^{jet} > 5\ GeV$
  - $15° < \theta_{jet} < 164°$
  - $ltf > 0$
  - $ltf + emfrac < 1.6$
  - $0.05 < emfrac < 0.95$
  - For the signal jets ($W \rightarrow \tau\nu_\tau$ MC simulation) the reconstructed jet had to be matched with the direction of the $\tau$ lepton that decayed hadronically (the distance in the $(\eta, \phi)$ plane had to be smaller than one unit), to ensure a signal sample of good quality.

Control plots of global event variables for the inclusive CC DIS selection are shown in Fig. 7.5.

Good agreement between data and CC DIS Monte Carlo simulation is achieved for all quantities considered. The simulated signal ($W \rightarrow \tau\nu_\tau$) is far below the data for this inclusive CC DIS selection, which was performed to obtain good reference signal and background samples needed for a calculation of the discriminant $D$.

The jet shape observables that entered discriminant evaluation for an inclusive selection of CC DIS events are presented in Fig 7.6. For each event, only a jet with largest transverse momentum, $p_T^{jet}$, enters.

The data are well described by the CC DIS Monte Carlo Simulation. Different $W \rightarrow \tau\nu_\tau$ signal and CC DIS background shapes for each of the six variables can be seen. This fact is exploited using multi-variable discrimination technique to obtain optimal signal-to-background separation.

To insure reliable discriminant calculation, the total number (signal and background) of jets in a small box around the considered jet was required to be greater than 15. If that was not the case a jet was not classified. The fraction of events that passed all selection cuts, but did not have any classified jet, was 0.7% for the CC DIS simulation and 0.3% for the signal MC. The edge lengths of the small box were:

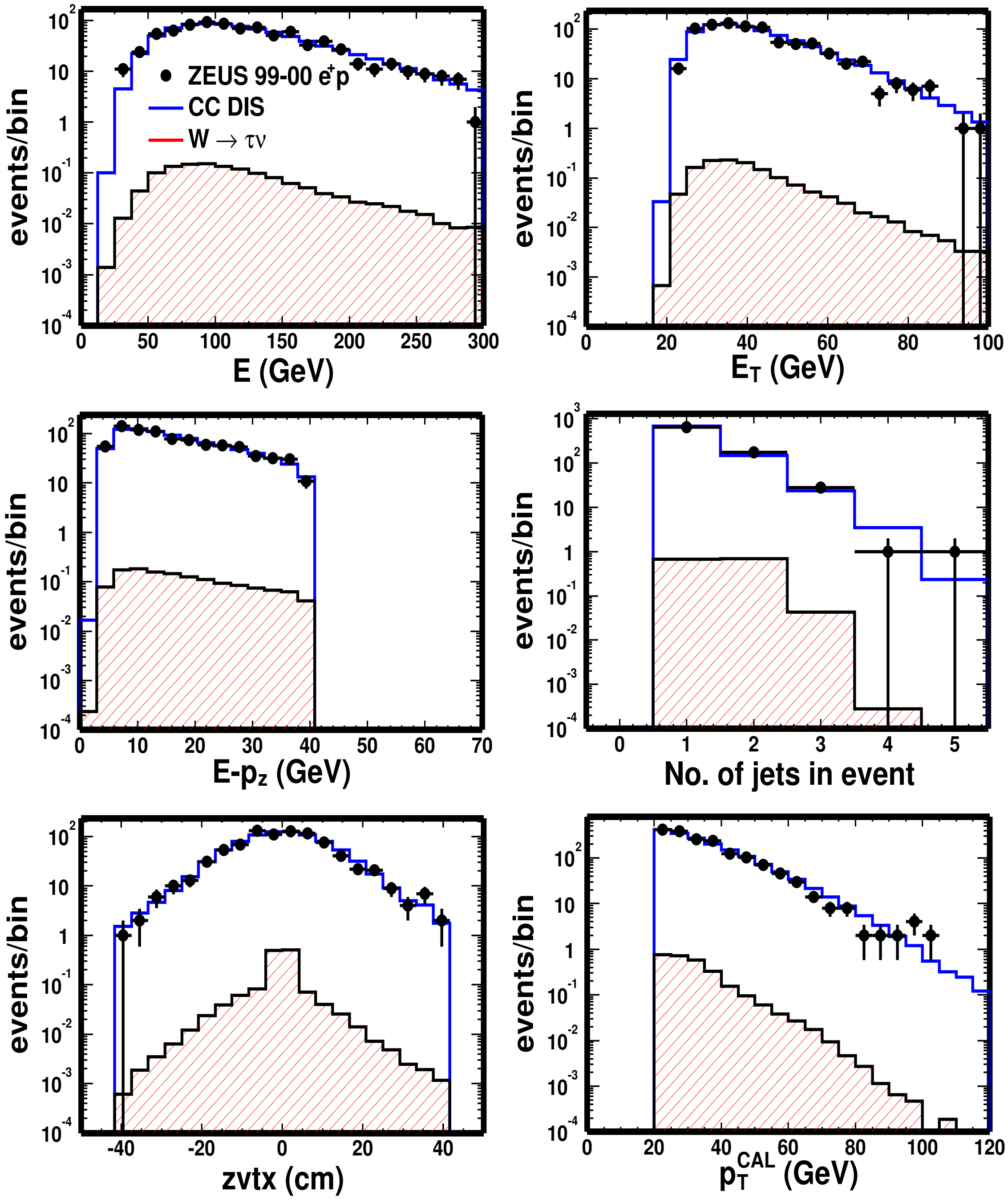


Figure 7.5: Event properties for an inclusive CC DIS selection, the 1999-2000 $e^+p$ data (dots), the CC DIS MC simulation (open histogram) and the $W \to \tau\nu_\tau$ MC simulation where the $\tau$ decays hadronically (hatched histograms). Given are: the total energy, the transverse energy, $E - p_z$, number of jets in event, $z$-coordinate of the event vertex and the missing transverse momentum $p_T^{CAL}$. The histograms are normalised to the luminosity of the data.

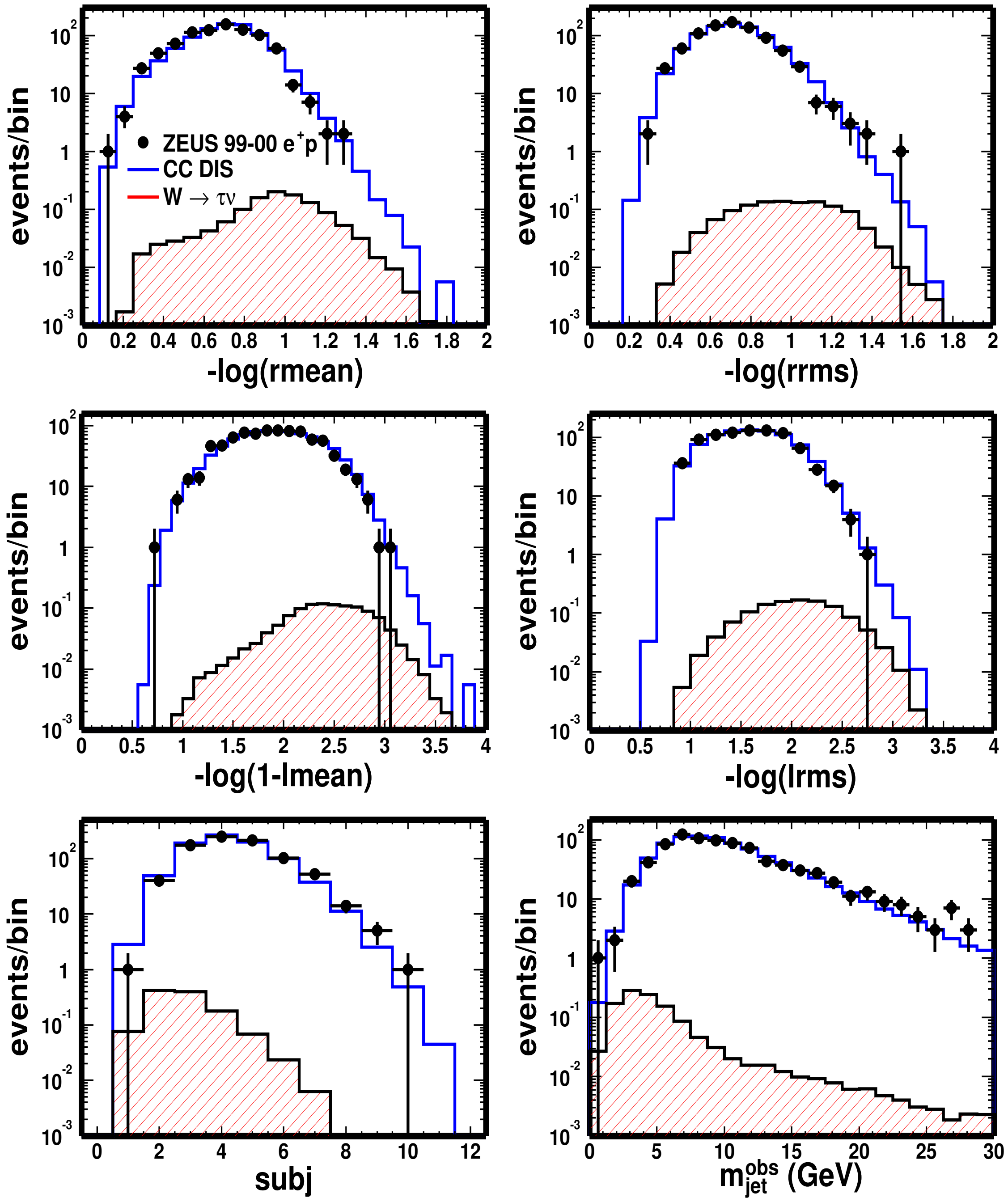


Figure 7.6: Observables characterising the internal jet structure for an inclusive selection of CC DIS events. Shown are the 1999-2000 $e^+p$ data (dots), the simulation of CC DIS events (open histograms) and the $W \to \tau\nu_\tau$ MC simulation where the $\tau$ decays hadronically (hatched histograms). For each event, only the jet with largest transverse momentum enters. The histograms are normalised to the luminosity of the data.

| Variable | edge length |
|---|---|
| $-\log(R_{mean})$ | 0.4 |
| $-\log(R_{rms})$ | 0.4 |
| $-\log(1-L_{mean})$ | 0.4 |
| $-\log(L_{rms})$ | 0.4 |
| $N_{subj}$ | 1 |
| $M_{jet}$ | 1 $GeV$ |

Figure 7.7 shows the distribution of $D$ for the simulated signal and background events and for the data selection. For each event, the jet with the largest value of the discriminant enters.

As expected, the $\tau$ signal tends to have large discriminant values and is clearly separated from the CC DIS background at low discriminant values. The data for inclusive CC DIS selection are well described by the background MC simulation. No enhancement is seen in the data w.r.t. the SM simulation at large D.

The quality of the $\tau$ selection is characterised by the efficiency of the signal selection, $\epsilon_{sig}$, the rejection of the background, $R$, and the separation power, S, which are defined for a given cut on the discriminant, $D_{cut}$, as follows:

$$\begin{aligned} \epsilon_{sig} &= N_{sig,selected}/N_{sig,total} \\ R &= N_{bg,total}/N_{bg,selected} \\ S &= \sqrt{R}\cdot\epsilon_{sig}. \end{aligned}$$

In the equations above, $N_{sig,total}$ and $N_{bg,total}$ are the total number of signal and background events, respectively, and $N_{sig,selected}$ and $N_{bg,selected}$ are the number of signal and background events after applying a cut of $D > D_{cut}$, respectively. The cut on $D$ was optimised for maximal separation power. As defined above, maximal separation power gives the most prominent signal with respect to the background fluctuations. Figure 7.8 a) shows the values of $\epsilon_{sig}$ and $S$ as a function of discriminant cut value $D_{cut}$ for the CC DIS selection. An optimal separation between signal and background is achieved for $D_{cut}$ value of about 0.95, which was used for this analysis. The $\tau$ discriminat signal efficiency $\epsilon_{sig} = 31\pm0.2\%$, a background rejection $R = 179 \pm 6$ and a separation power $S = 4.1 \pm 0.1$ were obtained for $D > 0.95$.

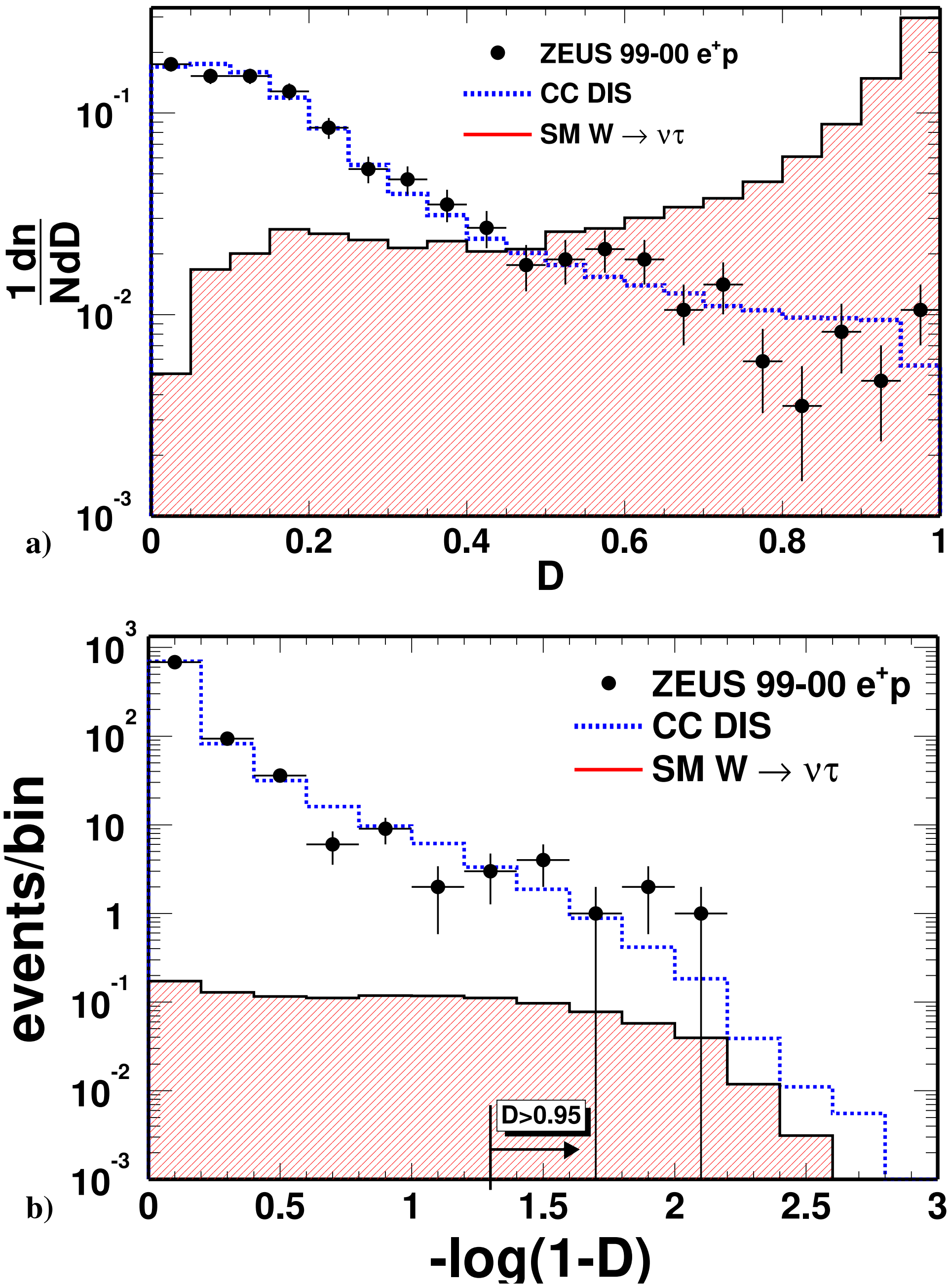


Figure 7.7: Distribution of the $\tau$ discriminant, $D$, for an inclusive selection of CC DIS data events (dots), a simulation of CC DIS events (open histograms) and the simulation of the $W^{\pm}$ production signal $W \to \tau\nu_{\tau}$, where the $\tau$ decays hadronically (hatched histogram). In each event, only the jet with the highest value of the discriminant enters. The histograms are normalised a) to the total number of events N and b) to the luminosity of the data. In b), the $-\log(1-D)$ distribution is displayed to expand the region in which the $\tau$ lepton signal is expected.

The quoted uncertainties are the statistical uncertainties due to the limited number of generated MC events. When restricting the selection to jets with only one track, Fig. 7.8 c), relevant for the search for 1-prong hadronic $\tau$ decays (as required for isolated $\tau$ search) the optimisation again resulted in a value of $D > 0.95$. In this case the signal efficiency was $\epsilon_{sig} = 22 \pm 0.2\%$, the background rejection was $R = 637 \pm 41$ and the separation was $S = 5.5 \pm 0.2$. These results are basically independent of the model chosen for the simulation of the QCD cascade in the CC DIS simulation (CDM or MEPS) [6].

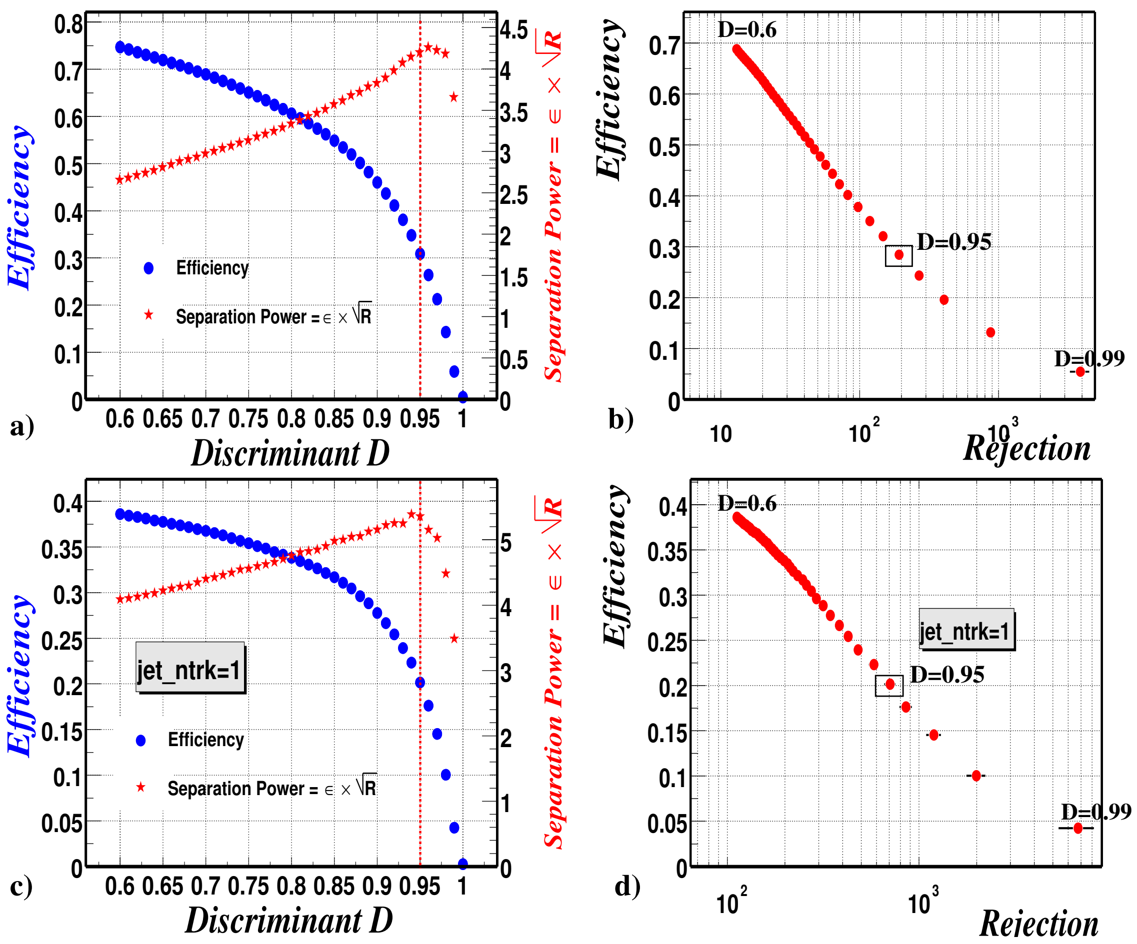


Figure 7.8: Signal efficiency, $\epsilon_{sig}$, and separation power, $S$, as a function of the $\tau$ discriminant cut value, $D_{cut}$, for the inclusive CC DIS selection, a) and c). The background rejection, $R$, and $\epsilon_{sig}$ obtained for different $D_{cut}$ values are shown in b) and d), with associated statistical uncertainties. The cut value $D > 0.95$ (red line) was used in this analysis. In a) and b) there is no restriction on the number of tracks inside the jet, while in c) and d) only jets with one associated track contribute (one track jets are relevant for isolated $\tau$ search based on the isolated track selection).

The inclusive CC DIS selection and discriminant setup, presented above, was based on the 1999-2000 $e^+p$ data taking period and coresponding MC simulations. However, as will be described in Section 7.3, an independent isolated $\tau$ selection was based on the full HERA I data set 1994-2000. The same $\tau$ discriminant setup and calculation, given above, were used for all data taking periods. To justify such approach, the shapes of jet observables used to calculate the $\tau$ discriminat were examined for $W$ signal and CC DIS background, respectively. Negligible shape differences were found between different data taking periods.

### 7.2.4 $\tau$ discriminant: NC DIS crosschecks

Both the suppression of QCD jets and the probability to misidentify electrons as $\tau$ jets were determined from samples of simulated NC DIS events and a selection of NC DIS data events [81], where an electron is scattered back-to-back to a jet in the detector. The main selection criteria for the NC DIS sample were a well reconstructed electron from Sinistra95 electron finder, $Q^2 > 400\ GeV^2$ and at least one jet in the acceptance of the detector. The jet shape observables for a NC DIS selection are presented in Fig 7.9. For each event, only the jet with largest transverse momentum, $p_T^{jet}$, enters. The setup of the discriminant was the same as described in Section 7.2.3.2.

The data are reasonably well described by the NC MC simulation. Both electrons and NC DIS jets contribute, therefore the shapes are different from corresponding jet observables obtained for the inclusive CC DIS selection where only QCD jets matter. A phase space region where descrepancies between the data and NC DIS MC simulation are largest is associated to the electrons.

As explained, the $\tau$ identification technique distinguishes between hadronic $\tau$ jets and QCD induced jets. Electrons can have signature in the detector very similar to hadronic $\tau$ decays. Hence, an efficient electron rejection has to be deployed in addition to avoid misidentification of electron jets with $\tau$ jets. Electron energy depositions in the calorimeter are usually fully contained inside the electromagnetic part and the transverse momentum of the electron track equals the transverse momentum calculated using the energy depositions in the calorimeter. This information was exploited to design electron rejection cuts used for inclusive CC DIS selection presented in Section 7.2.3.2. To determine the electron rejection, events in the NC DIS simulation which had no well identified electron were also considered. The upper limit on the fraction of NC DIS electrons that passed inclusive CC DIS selection and $\tau$ identification ($D > 0.95$) was $3 \times 10^{-6}$. No significant difference

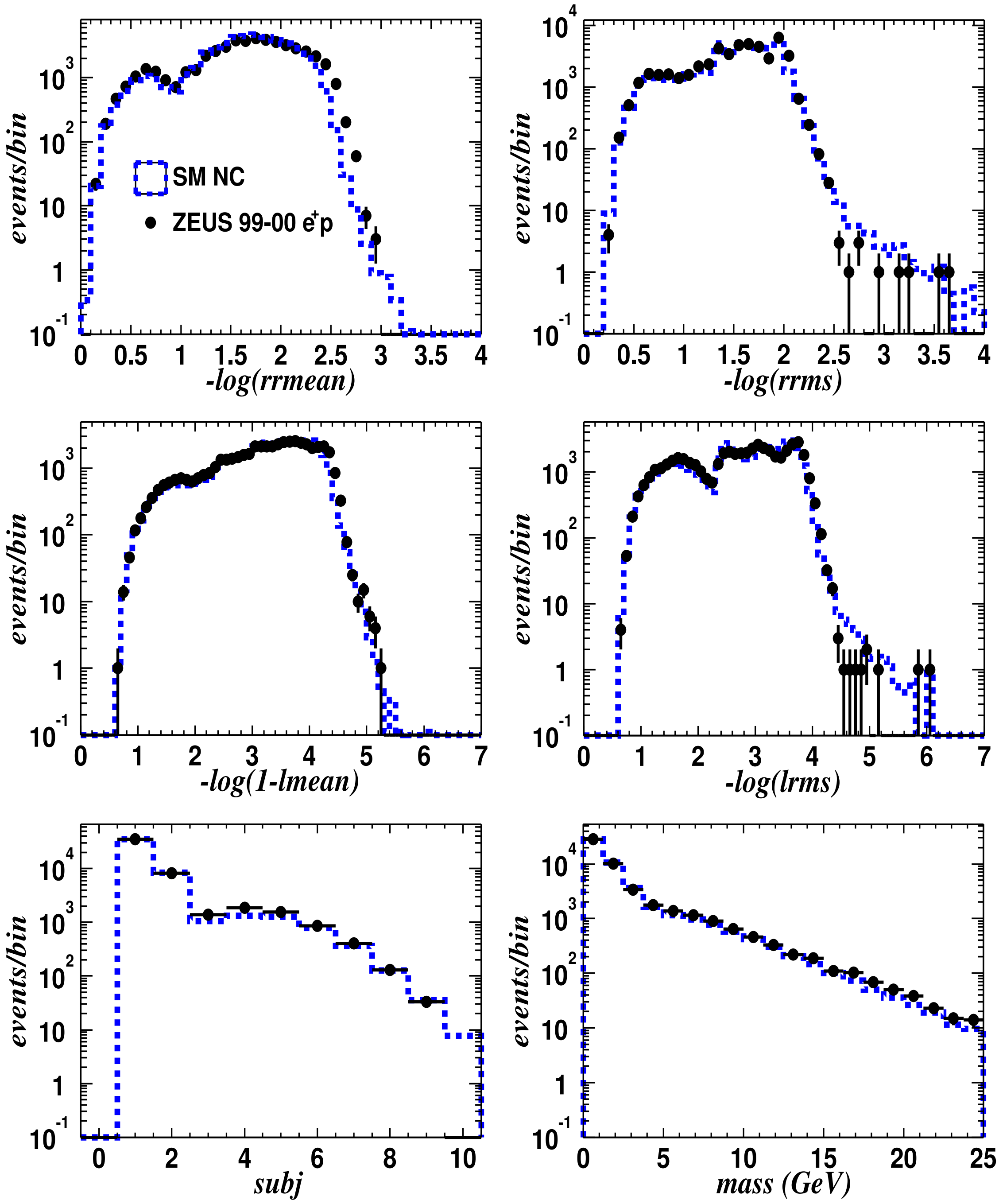


Figure 7.9: Control observables characterising the internal jet structure for a NC DIS selection. For each event, only jet with largest transverse momentum, $p_T^{jet}$, enters. Shown are the 1999-2000 $e^+p$ data (dots) and the simulation of NC DIS events (blue (dashed) histogram).

between data and MC simulation was observed.

To determine the rejection factor for NC QCD jets, the electron rejection cuts from the CC DIS selection were first applied to all jets in the sample. Figure 7.10 a) shows the distribution of the number of tracks in a jet for the NC DIS selection after the electron rejection cuts were applied. The agreement between the data and the simulation is reasonable. The distribution of the number of tracks in a jet after $\tau$ discriminant cut $D > 0.95$ was applied is presented in Fig. 7.10 b). The NC DIS simulation gives fair representation of the data. For the surviving one track jets, the $\tau$ discriminant gives rejection factor of $R = 550$ (the ratio between the total number of jets before cut on $D$ and the number of one track jets after $D > 0.95$ cut, see Fig. 7.10). This result is in reasonable agreement with the results from the CC DIS MC given in Section 7.2.3.2. No significant dependence of the rejection on the transverse energy of the jets was found, as well as on the jet pseudorapidity in the phase space region relevant for the isolated $\tau$ study.

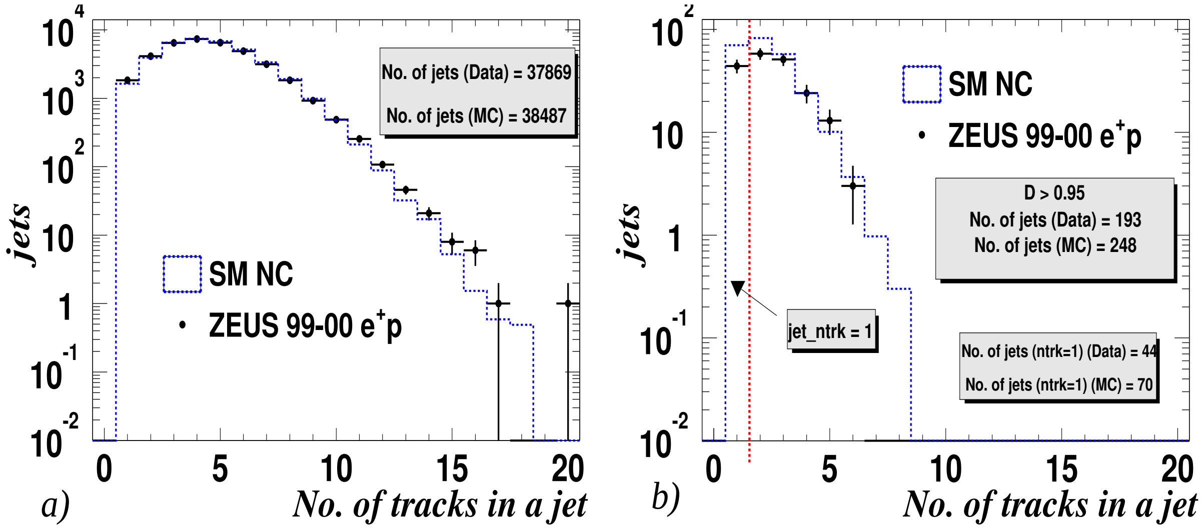


Figure 7.10: Distribution of the number of tracks in a QCD jet for NC DIS selection after electron rejection cuts from inclusive CC DIS analysis were applied. Shown are the distributions for all jets a), and the distributions after $\tau$ discriminant cut, $D > 0.95$, was applied b). The dots are 1999-2000 $e^+p$ data and blue (dashed) histogram is NC DIS MC.

## 7.3 Isolated $\tau$ event selection

The event selection closely follows the previous ZEUS search [5, 71] for events with isolated electrons or muons and large missing transverse momentum.

The non-*ep* rejection and preselection based on the requirement of an isolated $\tau$ lepton, decaying to one charged particle, together with large missing transverse momentum are presented in this section. The final selection stage required events with large values of the hadronic transverse momentum. Unless otherwise stated, the selection requirements were applied to both data and Monte Carlo simulation events.

The data used in this analysis were collected with the ZEUS detector and correspond to an integrated luminosity of 47.9±0.9 (65.5±1.5) $pb^{-1}$ for $e^+p$ collisions taken during 1994-1997 (1999-2000) and $16.7 \pm 0.3$ $pb^{-1}$ for $e^-p$ collisions taken during 1998-99.

To estimate the total SM contribution, the CC and NC DIS ($Q^2 > 100\, GeV^2$), resolved and direct photoproduction MC simulations were considered (as described in Chapter 5). In addition, the simulation of $W^\pm$ *production* $e^\pm p \to e^\pm W X$ as presented in this chapter and the simulation of *lepton pair production* $e^\pm p \to e^\pm l^\pm l^\mp X$, $l = e, \mu, \tau$, see Chapter 8, were analysed. The anomalous production of single top quarks was used as a template for processes involving the production of heavy particles and was simulated as explained in the Section 7.1.2. Depending on the data taking periods mentioned above, for each of these processes, different simulation setups were considered, respectively.

### 7.3.1 Non-*ep* rejection and preselection of isolated $\tau$ events

- `Trigger selection`
  Only events that fulfilled the charged current trigger bit DST 34 were considered. The DST trigger bits contain the selection requirements from all three levels of the ZEUS trigger chain. For the DST 34 bit, the main selection criteria are large missing transverse momentum as measured without contribution from the first inner ring of the FCAL, $p_T^{ex1IR} > 7\ GeV$, and a reconstructed vertex consistent with *ep* interaction. The efficiency of this online selection for the kinematic range of interest was found to be 100% for simulated events.

- `Event` $z$`-vertex`

| timing cuts ($ns$) | minimal energy ($GeV$) |
|---|---|
| $\lvert t_{FCAL}\rvert < 5$ | $E_{FCAL} > 4$ |
| $\lvert t_{BCAL}\rvert < 5$ | $E_{BCAL} > 4$ |
| $\lvert t_{RCAL}\rvert < 5$ | $E_{RCAL} > 4$ |
| $\lvert t_{FCAL} - t_{RCAL}\rvert < 6$ | $E_{CAL} > 5$ |
| $\lvert t_{upCAL} - t_{downCAL}\rvert < 6$ | $E_{CAL} > 5$ |

Table 7.2: Timing cuts and minimal energy demands for the different parts of the CAL.

The event vertex along beam direction was required to be $|z_{vtx}| < 50\ cm$ to reduce non-$ep$ background contribution. The CTD only tracks were used to reconstruct event vertex.

- `Calorimeter timing`
  The timing information from the calorimeter was used to reject energetic muons coming from interactions of cosmic rays in the atmosphere and to reject beam-gas interaction, which took place upstream the detector. The timing of the calorimeter cells was adjusted by using relativistic particles originated from the nominal interaction point. Table 7.2 presents timing cut values used for the minimum energy deposition in the corresponding parts of the calorimeter, where $t_X$ corresponds to the average timing measured in the part $X$ of the calorimeter. The timing cuts for particular calorimeter part were applied only if some energy deposition was measured in that calorimeter part, i.e. if the energy exceeded a default value. The timing information and cuts were used only for data events.

- `Beam gas rejection`
  - $p_T^{ex1IR} > 9\ GeV$. Beam-gas events typically result in a significant energy deposition only in the inner parts (rings) of the forward calorimeter.
  - $N_{tracks}^{good} > 0.2 \cdot N_{tracks} - 20$. Here $N_{tracks}$ is the total number of tracks and $N_{tracks}^{good}$ is the number of good tracks, i.e. tracks fitted to the primary vertex with $p_T^{track} > 200\ MeV$. Beam-gas events and beampipe scatterings have a large number of low energy tracks not associated to a single interaction vertex in the detector.

- `Rejection of cosmic muons`

  Cosmic muons usually traverse the detector in a straight line. Hence, events were not considered if they had only two tracks fitted to the primary vertex with $p_T^{track} > 200\ MeV$ and if the tracks had 3-dim opening angle greater than $178°$.

- `Holes in the calorimeter`

  Calorimeter cells where both photomultipliers were not functioning, were marked as calorimeter holes. If a high momentum track hits a calorimeter hole it may induce serious mismeasurements of the event properties. Therefore, events were not considered in which a $p_T > 3\ GeV$ track was pointed into any dead calorimeter cell (3-dim opening angle between the track and the dead cell vector had to be smaller than $0.1\ rad$). The number of CAL holes varied during the data taking period considered, but the overall effect of the dead cells was very small.

- `Large missing transverse momentum`

  A large missing transverse momentum was required, $p_T^{CAL} > 20\ GeV$, where $p_T^{CAL}$ was reconstructed using the energy deposited in the CAL cells, after corrections for non-uniformity and dead material located in front of the CAL [82].

- `Jet requirements`

  The selected events had to contain at least one hadronic jet, reconstructed as described in Section 7.2.3.1, with a transverse energy $E_T^{jet} > 5\ GeV$ within the range of $-1.0 < \eta < 2.5$.

- `Track requirements`

  A track with transverse momentum $p_T^{track} > 5\ GeV$, associated with the event vertex and pointing in the direction of a candidate jet, was required. It had to pass through at least three radial superlayers of the CTD (corresponding to $\theta \geq 0.3\ rad$) and to have $\theta < 2\ rad$.

- `Track and jet isolation`

  The track was required to be isolated with respect to all tracks fitted to the primary vertex with $p_T^{track} > 100\ MeV$ and jets in the event: $D_{trk} > 0.5$ and $D_{jet} > 1.8$, where $D_{trk}$ and $D_{jet}$ are the separation of the given track in the $(\eta, \phi)$ plane from the nearest neighbouring track and the nearest neighbouring jet in the event, respectively.

- `Electron and muon rejection`

  Isolated tracks that were identified as electrons or muons (see Chapter 6) were rejected. An additional electron rejection was applied based on the fraction of electromagnetic jet energy and on the fraction of jet energy carried by the isolated track, described in Section 7.2.3.2. Remaining electron-type events with a topology characteristic for NC DIS events were rejected by requiring the acoplanarity, $\phi_{acopl}^{trk}$, to be greater than 8°, where $\phi_{acopl}^{trk}$ is defined as the azimuthal angle between the isolated track and the vector which balances the hadronic system. The 4-vector of the hadronic system was calculated by subtracting the 4-vector of the $\tau$ candidate jet from the 4-vector obtained from the energy deposited in the CAL cells.

- $\tau$ `discriminant`
  Only after all cuts described above were applied, the $\tau$ discriminant calculation was performed, with the discriminant setup established using inclusive CC DIS selection presented in Section 7.2.3.2. The events that contained isolated track associated to the jet whose discriminant value exceeded $D > 0.95$ were passed to the final selection stage.

### 7.3.2 Selection of events with high hadronic transverse momentum

To design the final cut for events with high $p_T^{had}$, the single top MC was used as a template for the production and decay of a heavy state. Following the published analysis in the electron and muon channels, an optimisation was performed, resulting in a cut at $p_T^{had} > 25\ GeV$ [6, 71], which gave the best separation between the single top events and the SM background coming from the $W$ boson production. The other sources of SM background gave very low number of expected events in the final sample of $\tau$ candidates to be used for a meaningful optimization of the final $p_T^{had}$ cut. A higher cut at $p_T^{had} > 40\ GeV$ was used for the electron and muon analysis [5]. For isolated $\tau$ search, very restrictive selection cuts had to be applied to suppress the large background from electrons and quark- or gluon-induced jets which resulted in much smaller selection efficiencies for SM $W^{\pm}$ production and, consequently, in smaller $p_T^{had}$ requirement than for electron and muon study.

## 7.4 Results

After the preselection and before the cut on the $\tau$ discriminant, seven events remained in the data while $2.2^{+0.39}_{-0.58}$ are expected from SM background (18% of the SM background came from single $W^{\pm}$ boson production and 67% came from CC

| Selection stage | Obs. | SM exp. ($W^{\pm}$ contrib.) | $\epsilon_{s.top} \cdot BR$ (%) |
|---|---|---|---|
| Isolated tracks | 7 | $2.18^{+0.39}_{-0.58}$ (18%) | 0.68 |
| Discriminant $D > 0.95$ | 3 | $0.40^{+0.12}_{-0.13}$ (43%) | 0.27 |
| $p_T^{had} > 25\ GeV$ (final sel.) | 2 | $0.20^{+0.05}_{-0.05}$ (49%) | 0.27 |
| $p_T^{had} > 40\ GeV$ | 1 | $0.07^{+0.02}_{-0.02}$ (71%) | 0.25 |

Table 7.3: Event yields for the data from 1994-2000, corresponding background expectations and efficiency times branching ratio for the single top MC at different selection stages in the search for isolated $\tau$ leptons. The percentage of single $W$ production included in the expectation is indicated in parentheses. The statistical and systematic uncertainties in quadrature are also indicated.

DIS). Table 7.3 summarises the event yields at different selection stages [6]. The quoted uncertainties on the SM expectations are discussed in Section 7.5.

Event variables after the preselection and before the cut on the $\tau$ discriminant, are presented in Fig. 7.11. The transverse mass, $M_T$, was calculated from the candidate jet and the missing transverse momentum as $M_T = \sqrt{2p_T^{jet}p_T^{CAL}(1-\cos(\delta\phi_{jet}))}$, where $\delta\phi_{jet}$ is the angular difference in the azimuthal plane between the isolated jet and the direction of $p_T^{CAL}$.

Already after the preselection and before the cut on the $\tau$ discriminant, the number of observed data events exceeds the SM background expectation. This will be discussed in more detail in Section 7.6.

The discriminant distributions are given in Fig. 7.12., linear and logarithmic ($-\log(1-D)$). The logarithmic distribution emphasises the high discriminant region.

Three out of the seven events have an isolated jet with $\tau$ discriminant $D > 0.95$ and therefore can be associated to hadronically decaying $\tau$ leptons. After applying the cut $D > 0.95$, $0.40^{+0.12}_{-0.13}$ events are expected from SM background (43% from single $W^{\pm}$ boson production, 30% from CC DIS and 22% from NC DIS).

Figure 7.13 shows the event distributions after applying the cut at $D > 0.95$. The transverse mass, $M_T$, was calculated from the $\tau$ candidate jet and the missing transverse momentum.

After the final cut on the hadronic transverse momentum, $p_T^{had} > 25\ GeV$, two events remained in the data, while $0.20 \pm 0.05$ events are expected from the SM (49% from single $W^{\pm}$ boson production and 42% from CC DIS). With a higher cut at $p_T^{had} > 40\ GeV$, one event remains in the data, while $0.07 \pm 0.02$ events are

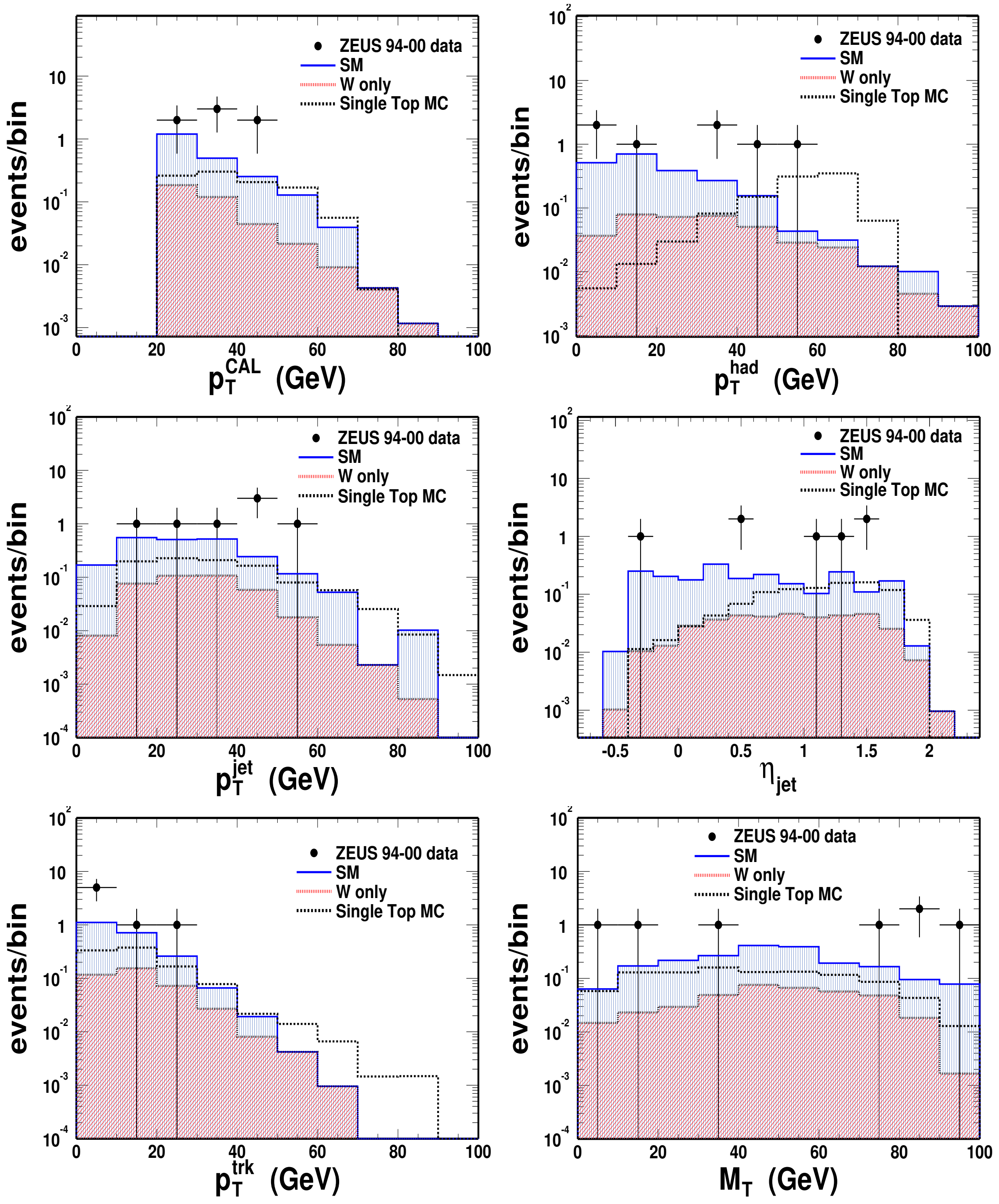


Figure 7.11: Distributions of the missing momentum, the hadronic transverse momentum, the transverse momentum and pseudorapidity of the isolated jet, the transverse momentum of the track associated to the isolated jet and the transverse mass, after the preselection and before cut on the $\tau$ discriminant. The data (points) are compared to the SM expectations blue (light) histogram. The red (dark) histogram represents the contribution from $W^{\pm}$ boson production in the SM. The dashed line represents the distribution of the single top MC, including all decay channels of the $W^{\pm}$ boson, normalised to an integral of one event.

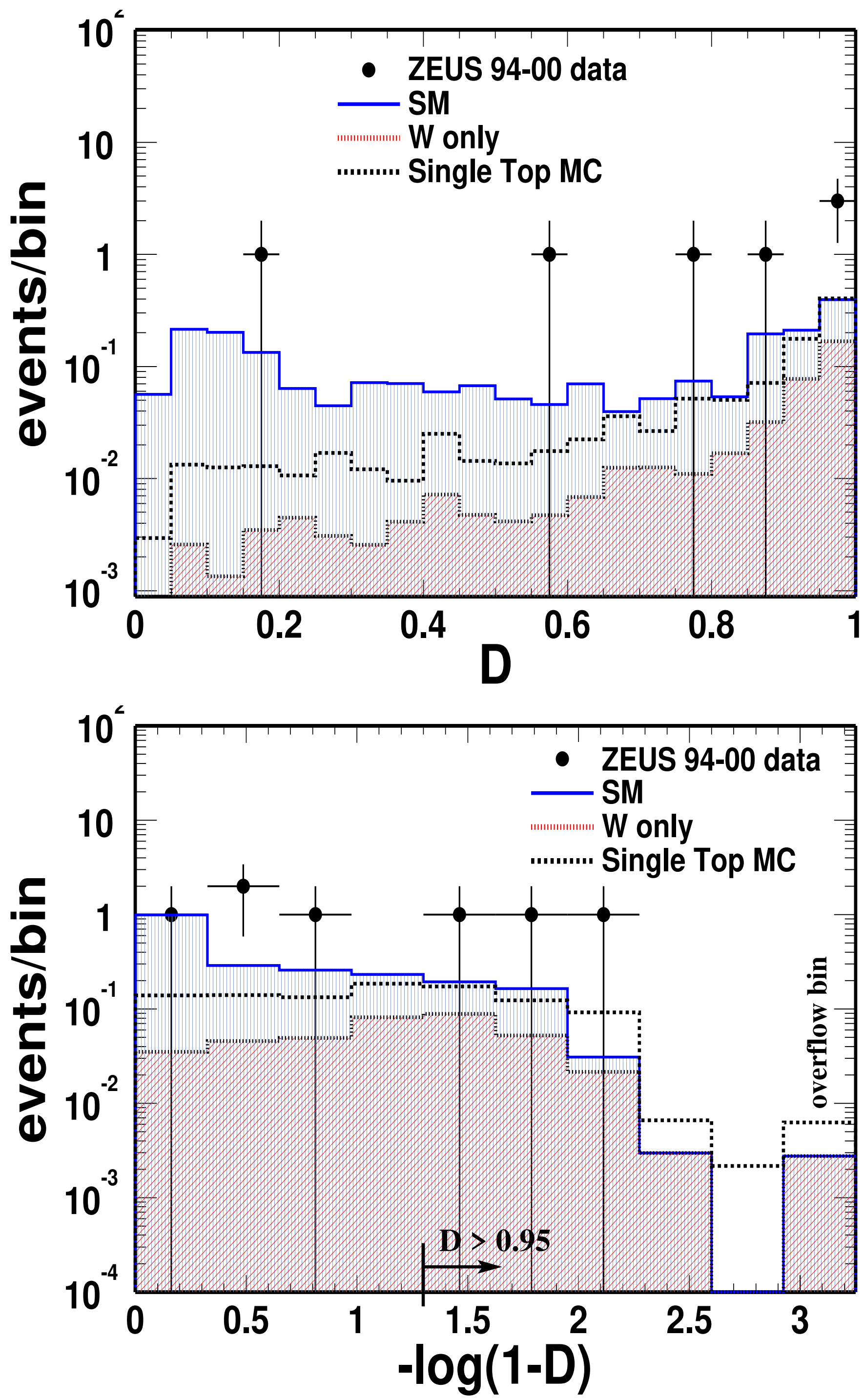


Figure 7.12: Isolated $\tau$ discriminant, linear and logarithmic, for the $\tau$ preselection before applying the cut $D > 0.95$. The data (points) are compared to the SM expectations blue (light) histogram. The red (dark) histogram represents the contribution from $W^{\pm}$ boson production in the SM. The dashed line represents the distribution of the single top MC, including all decay channels of the $W^{\pm}$ boson, normalised to an integral of one event.

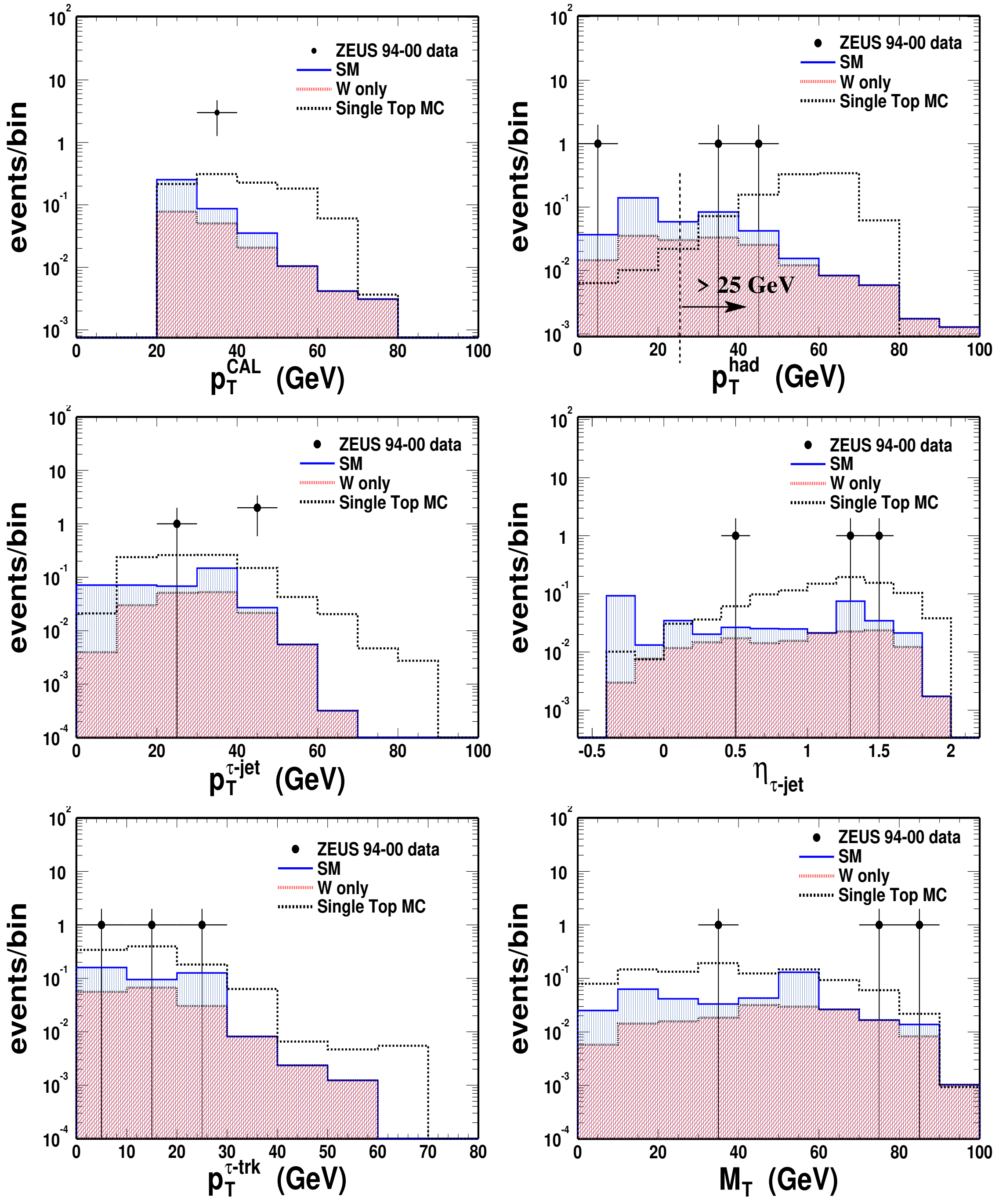


Figure 7.13: Distributions of the missing momentum, the hadronic transverse momentum, the transverse momentum and pseudorapidity of the $\tau$ jet, the transverse momentum of the track associated to the $\tau$ jet and transverse mass, after the cut on the $\tau$ discriminant. The data (points) are compared to the SM expectations blue (light) histogram. The red (dark) histogram represents the contribution from $W^{\pm}$ boson production in the SM. The dashed line represents the distribution of the single top MC, including all decay channels of the $W^{\pm}$ boson, normalised to an integral of one event.

| Quantity | Event 1 | Event 2 |
|---|---|---|
| Missing transverse momentum $p_T^{CAL}$ | 37 GeV | 39 GeV |
| Hadronic transverse momentum $p_T^{had}$ | 48 GeV | 38 GeV |
| Transverse momentum of the $\tau$ candidate jet $p_T^{jet}$ | 21 GeV | 41 GeV |
| Transverse momentum of the $\tau$ candidate track $p_T^{trk}$ | 9 GeV | 27 GeV |
| Charge sign of the $\tau$ candidate track<br>Significance in numbers of standard deviations | $-$<br>$5.7\sigma$ | $+$<br>$3.8\sigma$ |
| Acoplanarity of the $\tau$ candidate track $\phi_{acopl}^{trk}$ | 45° | 55° |
| Transverse mass $M_T$ | 32 GeV | 70 GeV |
| Discriminant $D$ | 0.994 | 0.977 |

Table 7.4: Selected event variables for the two $\tau$ candidate events at high $p_T^{had}$.

expected from the SM (71% from single $W^\pm$ boson production). Figure 7.14 shows event displays of the two events with large values of $p_T^{had}$.

Selected event variables for the two candidates are given in Table 7.4. Both events were found at large acoplanarity, therefore are not likely to originate from NC DIS scattering. The candidate events were identified in the $e^+p$ data sample.

## 7.5 Systematic uncertainties

The errors on the background expectation values were obtained as the quadratic sum of the statistical uncertainties of the generated MC events and each of the following systematic uncertainties [6, 71]:

- *Simulation of the QCD cascade.* The use of MEPS instead of CDM to estimate both the NC DIS and CC DIS background gave a change of up to $-20\%$ in the total background estimation;
- *Track selection.* A variation of the track quality requirements and the angular range of the track selection resulted in changes of up to $\pm 15\%$ in the background estimation;
- *W cross section.* The uncertainty for the expectation from single $W^\pm$ boson production, after including higher order QCD corrections by reweighting the

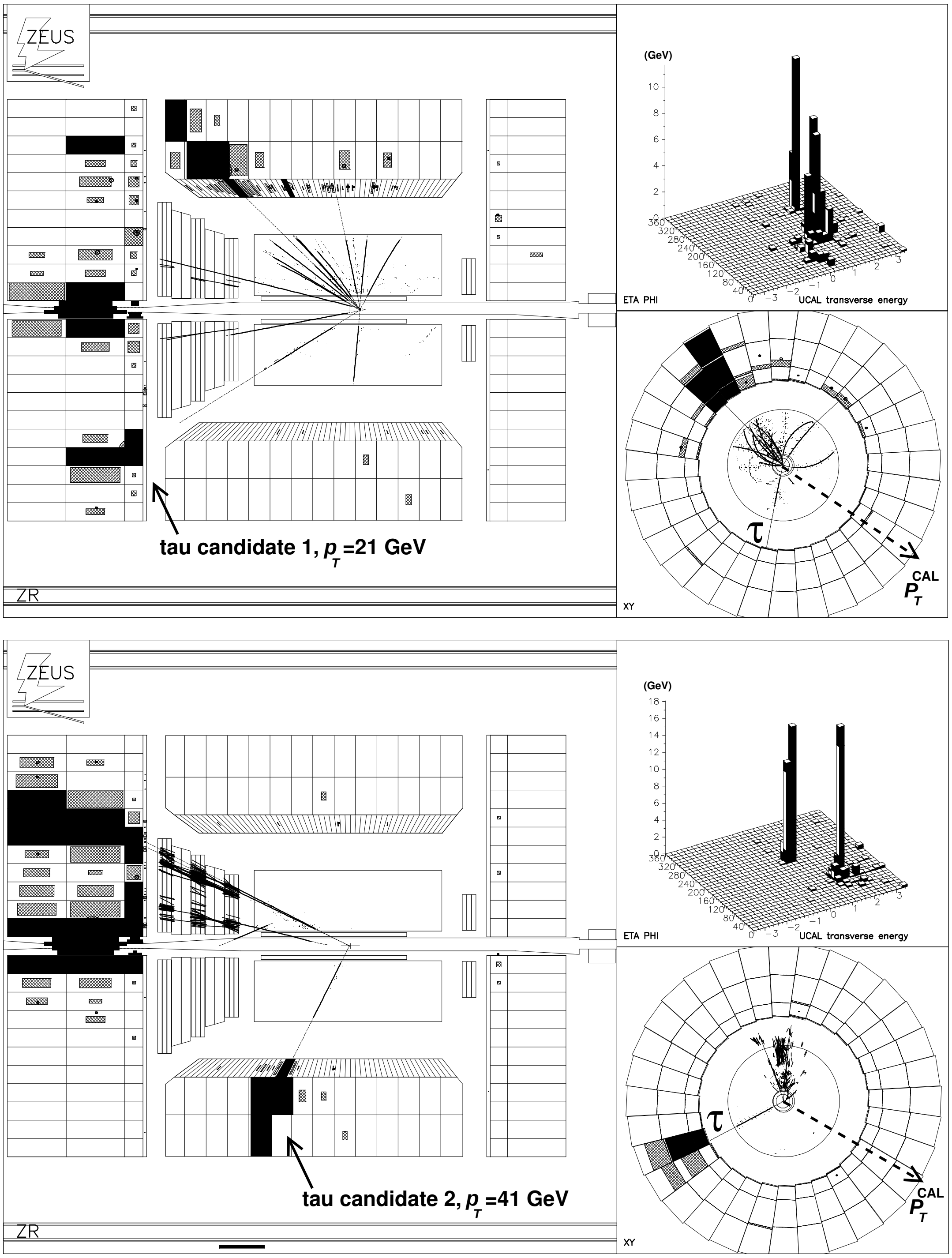


Figure 7.14: $\tau$ candidate events from $e^+p$ interactions at $\sqrt{s} = 318\ GeV$ in the ZEUS detector. The energy deposition in the CAL is proportional to the size and density of shading in the CAL cells. The lego plot shows the CAL energy deposition projected in the $(\eta, \phi)$ plane. In the $xy$ view, only the energy deposition in the barrel calorimeter is shown. The dashed arrow in the $xy$ view indicates the direction of the missing transverse momentum in the calorimeter, $p_T^{CAL}$. Selected event variables for the two candidates are given in Table 7.4.

LO MC samples [70, 68, 69] was estimated to be 15%;

- *$\tau$ decay simulation.* As a cross check, TAUOLA 2.6 [72] was used instead of JETSET for the simulation of the $\tau$ decays originating from single $W^{\pm}$ boson production. The TAUOLA program takes into account polarisation effects, whereas in JETSET the $\tau$ leptons are always decayed isotropically in their rest frame. The influence of the $\tau$ decay treatment on the jet shape observables and on the efficiency for the event selection was found to be negligible;

- *$\tau$ discriminant method.* Both the CC DIS control selection and the $\tau$ search analysis were repeated with modified sets of jet shape observables. In addition, the box size used to evaluate the signal and background densities was varied. The dependence on these parameters was negligible;

- *Calorimeter energy scale.* The uncertainty of $\pm 1\%$ on the absolute energy scale of both the electromagnetic and the hadronic parts of the CAL resulted in changes of up to $\pm 4\%$ in the SM background estimation.

In addition, the jet reconstruction using the longitudinally invariant $k_T$ cluster algorithm in the inclusive mode was repeated with another jet recombination scheme, $E$-scheme, which results in a massive final state jets. The jet shape observables used to calculate the $\tau$ discriminant were recalculated. The difference from the original jet recombination treatment, $E_T$-scheme, which results in massless final state jets was negligible.

## 7.6 Summary and discussion

A search for events containing isolated $\tau$ leptons, large missing transverse momentum and large hadronic transverse momentum, produced in $e^{\pm}p$ collisions at HERA, has been performed using 130 $pb^{-1}$ of integrated luminosity. Such a signature could be produced within the framework of many theories beyond the Standard Model. The selection required isolated tracks with associated pencil-like jets coming from hadronic $\tau$ decays and additional hadronic jet. A multi-observable discrimination technique was used, exploiting the internal jet structure to discriminate between hadronic $\tau$ decays and quark- or gluon-induced jets. Three isolated $\tau$ candidates were found, while $0.40^{+0.12}_{-0.13}$ were expected from Standard Model processes, mainly from charged current deep inelastic scattering and single $W^{\pm}$ boson production. A more restrictive selection was applied to isolate $\tau$ leptons in events with large missing transverse momentum produced together with a hadronic final state with high transverse momentum, as expected from the decay of a heavy particle. Two candidate events with a transverse momentum of the hadronic system $p_T^{had} > 25$ $GeV$ have been observed, while $0.20 \pm 0.05$ events were expected from Standard Model processes. The Poisson probability to observe two or more events, assuming only SM contribution, is 1.8%, where the uncertainty on the SM prediction was taken into account [6, 71]. Hence a statistical fluctuation cannot be excluded.

Interestingly enough, after the preselection and just before $\tau$ discriminant cut seven events remained while $2.2^{+0.39}_{-0.58}$ are expected from SM background, see Section 7.4, corresponding to an excess in observed events which is more significant than one quoted above for the final selection. However, the significance of the excess comes from the high discriminant region. For $D < 0.95$ four events were observed, expecting $1.8 \pm 0.4$, which corresponds to the Poisson probability to expect $\geq 4$ events of 12%. In addition, $\sim 75\%$ of expected events come from the CC DIS background simulation, which was able to describe well the inclusive CC DIS data selection used to establish the discriminant setup, see Fig. 7.5 and 7.6. Therefore, the agreement between data and MC expectation is acceptable for low values of the $\tau$ discriminant.

For $D > 0.95$ three events were observed while expecting $0.40^{+0.12}_{-0.13}$, which corresponds to a probability of 0.9%.

The $p_T^{had}$ distributions of the $W$ boson simulation in Fig. 7.11 and Fig. 7.13 are quite flat. As mentioned in Section 7.1.1, the total $W$ boson $p_T^{had}$ distribution should steeply decrease towards high values. However, the selection requirement of at least one hadronic jet in addition to the $\tau$ candidate jet reduces, almost completely, the resolved photoproduction of $W$ boson. The resolved photoproduction is the largest part of the total $W$ cross section and events have small $p_T^{had}$ values, typically. The distribution of the transverse mass, $M_T$, obtained from the candidate jet and the missing transverse momentum are shown in Fig. 7.11 and Fig. 7.13, as well. The single $W$ boson and single top MC contributions do not show, naively expected, Jacobian peaks arround the $W$ mass. This is caused by an additional missing transverse momentum originating from the $\tau$ decay, which adds to the missing momentum of the neutrino coming from $W \to \tau\nu_\tau$ decay. As can be seen from the pseudorapidity distributions of the selected jets that originate from simulated single top decays in Fig. 7.11 and Fig. 7.13, the decay products of a heavy particle should be boosted in the proton direction. All $\tau$ candidate jets found in the data sample have positive pseudorapidity values. Additional confirmation that discriminant cut $D > 0.95$ primary rejects background-like events can be seen from the difference between $p_T^{trk}$ and $p_T^{\tau-trk}$ distributions in Fig. 7.11 and Fig. 7.13. The discriminat

| ZEUS 1994-2000 $e^{\pm}p$ $\mathcal{L} = 130.1\ pb^{-1}$ | Electron obs./exp. ($W^{\pm}$ contribution) | Muon obs./exp. ($W^{\pm}$ contribution) | Tau obs./exp. ($W^{\pm}$ contribution) |
|---|---|---|---|
| $p_T^{had} > 25\ GeV$ | $2\ /\ 2.90\ ^{+0.59}_{-0.32}$ (45%) | $5\ /\ 2.75\ ^{+0.21}_{-0.21}$ (50%) | $2\ /\ 0.20\ ^{+0.05}_{-0.05}$ (49%) |
| $p_T^{had} > 40\ GeV$ | $0\ /\ 0.94\ ^{+0.11}_{-0.10}$ (61%) | $0\ /\ 0.95\ ^{+0.14}_{-0.10}$ (61%) | $1\ /\ 0.07\ ^{+0.02}_{-0.02}$ (71%) |

Table 7.5: Summary of the results of searches for events with isolated leptons, missing transverse momentum and large $p_T^{had}$. The number of observed events is compared to the SM prediction. The $W^{\pm}$ component is given in parentheses in percent. The statistical and systematic uncertainties added in quadrature are also indicated. The results for the electron and the muon channel were obtained from a previous search [5].

cut rejects events in which the candidate track has low $p_T^{trk}$ values, where the SM background expectation is largest.

Table 7.5 gives the result for the final selection in the $\tau$ channel as well as the results of the previous search in the electron and muon channel [5] for two different values of the cut on $p_T^{had}$.

In the electron (muon) channel, two (five) events were observed for $p_T^{had} > 25$ $GeV$, in good agreement with the SM prediction. No event was observed in either channel for $p_T^{had} > 40\ GeV$. In combination with a search in the hadronic decay channel of the $W^{\pm}$ boson, where no excess above the SM prediction was found, a limit on the cross section for single top production of $\sigma(ep \rightarrow etX, \sqrt{s} = 318$ $GeV) < 0.225\ pb^{-1}$ at 95% C.L. was obtained [5]. For the $\tau$ channel, two events were observed for $p_T^{had} > 25\ GeV$. Only hadronic $\tau$ decays were considered and very restrictive selection cuts had to be applied to suppress the large background from electrons and quark- or gluon-induced jets. Therefore, the selection efficiency for SM $W^{\pm}$ production is much smaller in the $\tau$ channel than in the electron and muon channels. The observed events would correspond to a cross section for single top production that is much higher than the excluded cross section, if the SM branching ratios for the top quark are assumed.

In addition, single top production produces positively charged leptons, and single anti-top production from protons is relatively suppressed by the parton densities. Therefore, the observed events are unlikely to be explained by the hypothesis of single top production.

When considered together with previously published results in the electron and muon channels, the two candidates are unlikely to originate from anomalous single top production or any other process where the $\tau$ lepton is produced through the decay of a $W^{\pm}$ boson.

A detailed discussion and comparison of the ZEUS results to the search for isolated electrons and muons performed by the H1 Collaboration, as well as expectations for isolated lepton searches at HERA II, can be found in [71]. Untill the date of considerations the results for isolated $\tau$ search were not included in the published results of the H1 Collaboration.

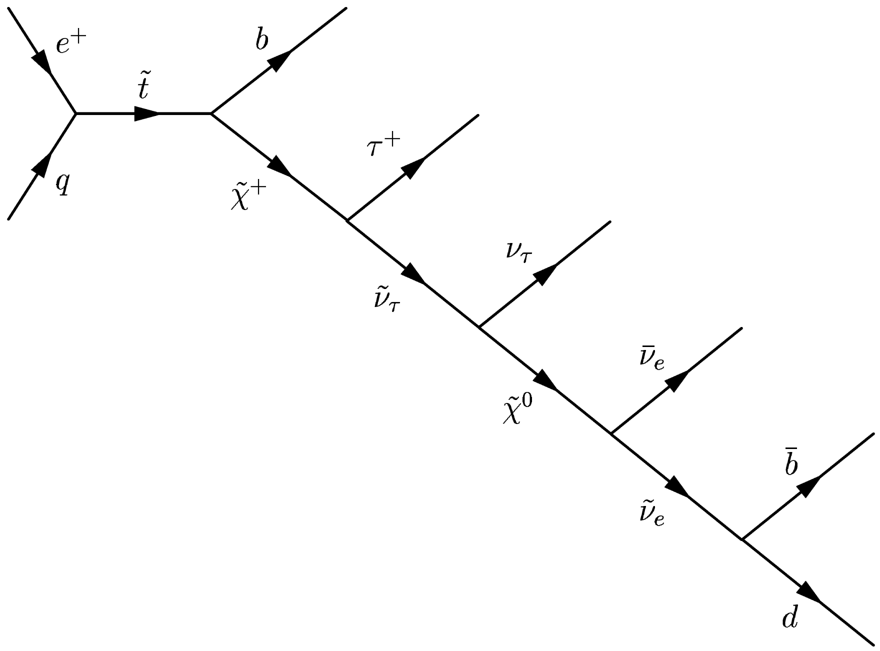


Figure 7.15: $R$-parity violating squark production in $ep$ collision with a subsequent decay scenario that leads to a $\tau$ lepton, missing transverse momentum and several jets in the final state.

$R_p$-violating SUSY models can explain enhanced $\tau$ production rates above the SM expectations. Moreover, if third generation sleptons are lighter than sleptons of the first and second generation, a corresponding enhancement for electrons and muons could be strongly suppressed. In such models, the stop quark can be directly produced at HERA via an $R_p$-violating Yukawa coupling and subsequently decay through $R_p$-violating or gauge couplings. In particular, the three-body gauge decay $\tilde{t} \to \tau\tilde{\nu_\tau}b$, $\tilde{\tau}\nu_\tau b$ with the subsequent decays $\tilde{\tau} \to \tau\tilde{\chi}^0$, $\tilde{\nu_\tau} \to \nu_\tau\tilde{\chi}^0$, see Fig.

7.15, would produce a final state with the characteristics of the observed events: a high $p_T$ $\tau$ lepton at large acoplanarity angle, missing transverse momentum and large hadronic transverse momentum. However, in this case the $\tau$ candidate has the same charge as the incoming lepton beam, which is only the case for one of the two events surviving the cuts [6].

The high luminosity of HERA II program ($\sim 1\ fb^{-1}$) and upgrades in both colliding experiments, H1 and ZEUS, will allow a continuation of the isolated lepton studies.

# CHAPTER 8
# ELECTROWEAK $\tau$ PAIR PRODUCTION AT HERA

Lepton pair production at HERA proceeds mainly via electromagnetic two-photon interactions, $\gamma\gamma \to l^+l^-$, where the photons come from the radiation of beam particles. An accurate SM prediction and clean experimental signature make the search for possible non-SM multi-lepton production mechanisms, very attractive. The non-SM production mechanisms like decay of doubly charged Higgs particles predicted within supersymmetric models or decay of vector gauge bosons with lepton number $L = 2$ predicted by a class of theories in which the electroweak $SU(2)\otimes U(1)$ gauge group is expanded [83], could lead to the similar event topology. In the di-muon channel, H1 and ZEUS results are in agreement with the SM expectation [7, 8], while in the multi-electron channel the H1 observation exceeds theory prediction [9] and the ZEUS finding is consistent with the SM [8], for the large invariant mass region ($M > 100\ GeV$).

Pair production of $\tau$ leptons, $\gamma\gamma \to \tau^+\tau^-$, is the main SM source of $\tau$ leptons at HERA, therefore an appropriate place to fully confirm identification technique developed for the isolated $\tau$ search. This chapter presents a $\tau$ pair analysis performed with the ZEUS detector. The aim was to explore the actual feasibility of tagging $\tau$ pair events at HERA which could be the basis for exciting searches. A search for the light Higgs boson where Higgs particle decays into pairs of $\tau$ leptons is described in the next chapter.

## 8.1 Production mechanisms

Refered also as “Bethe-Heitler”or $\gamma\gamma$, the dominant two-photon electroweak process is illustrated in the Feynman diagrams presented in Fig. 8.1 a) and b). Shown are an elastic $\gamma\gamma$ reaction, where the incoming proton is just recoiled, and the case of inelastic break up of the proton. Figure 8.1 c) depicts, the so called “Cabibbo-Parisi effect”, since Cabibbo and Parisi emphasised its occurrence in order to interpret some events found in the early photon-photon experiments at ADONE (Frascati) [86]. Here, a quasi-real photon generated (elastically or inelactically) by the proton creates an $e^+e^-$ pair and the positron (electron) thus produced interacts with the beam electron (positron) and gives rise to a lepton pair. The $e^+e^-$ pair via Bhabha scattering, or $\mu^+\mu^-$ ($\tau^+\tau^-$) pair via annihilation. The Drell-Yan process where the $q\bar{q}$ anihilation results in a lepton pair production is depicted in Fig. 8.1 d).

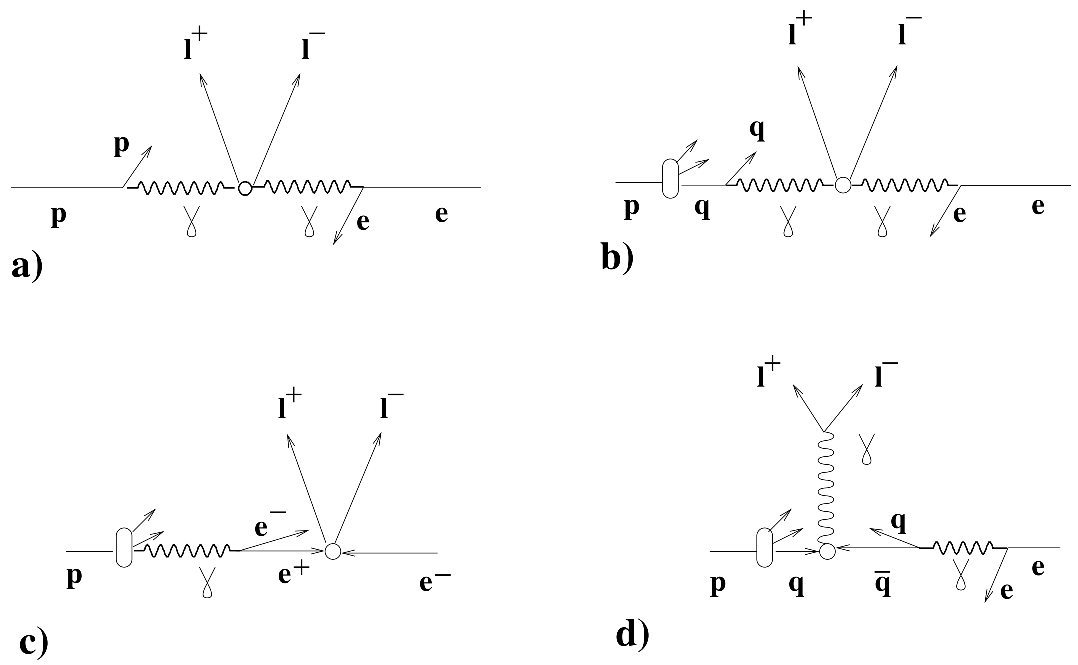


Figure 8.1: Feynman diagrams representing various contributions to the reaction $ep \to X(e)l^+l^-$: a) $\gamma\gamma$ elastic, b) $\gamma\gamma$ inelastic, c) Cabibbo-Parisi and d) Drell-Yan. In the general electroweak case, any of the photon propagators can be replaced by a $Z^0$ boson propagator.

The lepton pair production single differential cross section as a function of the transverse momentum, $p_T$, of one of the two leptons, is shown in Fig. 8.2 [84, 85]. Note that the strongly decreasing cross section is multiplied by $p_T^3$ to obtain less steep slopes.

The $\gamma\gamma$ production is the dominant process almost over the entire phase space considered. Shown are the elastic, $\gamma\gamma_{ela}$, and the inelastic, $\gamma\gamma_{ine}$, two-photon contributions, as well as the sum of these two channels, $\gamma\gamma_{tot}$. The elastic process exceeds the inelastic one at small transverse momenta $p_T$, while the inelastic channel takes over at large $p_T$. The two-photon dominance of the cross section gets weaker with increasing $p_T$. This behaviour may be explained by the $Z^0$ resonance contribution to the Cabibbo-Parisi and to the Drell-Yan process. Due to the contribution of Bhabha scattering the cross section of the Cabibbo-Parisi process is much larger in the electron channel ($CP_{ee}$) than in the muon channel ($CP_{\mu\mu}$). The Drell-Yan contribution is, up to $p_T = 40\ GeV$, always more than one order of magnitude smaller than the two-photon contribution. The curve labelled $DY_{PNT}$ shows a contribution of the point-like and $DY_{VMD}$ curve gives the resolved (Vector Meson Dominance (VDM)) contribution from the photon structure to the Drell-Yan process.

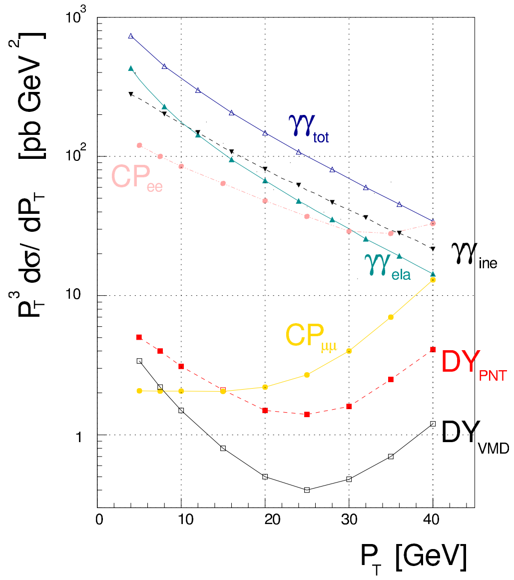


Figure 8.2: Lepton pair production single differential cross section, as a function of the transverse momentum $p_T$ of one of the two leptons [84]. $\gamma\gamma_{tot}$ denotes the total two-photon process, $\gamma\gamma_{ela}$ gives the elastic and $\gamma\gamma_{ine}$ the inelastic two-photon contributions. $CP_{ee}$ and $CP_{\mu\mu}$ are contributions from Cabibbo-Parisi process in the electron and muon channel, respectively. $DY_{PNT}$ and $DY_{VMD}$ (multiplied by 10) refer to the point-like and resolved Drell-Yan processes.

A cross section behaviour similar to the $\mu^+\mu^-$ channel could be expected for the $\tau$ pair production, at large $p_T$.

### 8.1.1 Monte Carlo simulation

The Monte Carlo event generator *GRAPE-Dilepton* [87] was used for the simulation of di-lepton production in *ep* collisions. GRAPE-Dilepton is based on the automatic Feynman graph calculation program GRACE [88]. A full set of electroweak matrix elements is calculated at tree level, with the exception of the Drell-Yan pole contribution (diagram (d) in Fig. 8.1). As mentioned, the influence from Drell-Yan processes was found to be negligibly small. The program also includes contributions due to $Z^0$ boson exchange.

The $e_{(in)}p_{(in)} \rightarrow el^+l^-X$ processes are classified into three categories using the negative momentum transfer squared at the proton vertex, $Q_p^2$, and the invariant mass of the hadronic system, $M_{had}$, defined as:

$$Q_p^2 = -\left\{p_{e(in)} - (p_e + p_{l^+} + p_{l^-})\right\}^2,$$

$$M_{had}^2 = \left\{ (p_{e(in)} + p_{p(in)}) - (p_e + p_{l^+} + p_{l^-}) \right\}^2,$$

where $p_{e(in)}$ and $p_{p(in)}$ are the 4-momenta of the incoming lepton and proton after *initial state QED radiation* (ISR). The three categories are:

- `elastic` ($M_{had} = M_p$),
- `quasi-elastic` ($Q_p^2 < Q_{min}^2$ OR $M_p + M_{\pi^0} < M_{had} < M_{cut}$),
- `deep inelastic (DIS)` ($Q_p^2 > Q_{min}^2$ AND $M_{had} > M_{cut}$),

where $M_p$ and $M_{\pi^0}$ are the masses of the proton and the neutral pion, respectively. $Q_{min}$ was set very close to 1 $GeV$ and the value for $M_{cut}$ was set to 5 $GeV$.

In the elastic region the hadronic structure is parametrised by the electromagnetic dipole form factors. In the quasi-elastic region and soft inelastic region ($M_{had} > 5$ $GeV$ and $Q_p^2 < 1$ $GeV^2$), the calculation is based on parametrisations of the proton structure functions, which are given in [89] for the nucleon resonance region ($M_{had} < 2$ $GeV$) and in [91] above the resonance region. The cross sections for $eq \to el^+l^-q$ are convoluted with the parton density functions of the proton [52] in the deep inelastic phase space region.

The GRAPE-Dilepton program is interfaced to PYTHIA [111] and SOPHIA [90] for a complete simulation of the inelastic lepton pair production processes. GRAPE-Dilepton includes QED ISR in the cross section [92]. *Final state QCD radiation* (FSR) is performed by PYTHIA using the parton shower method when the event is generated.

## 8.2 Description of the analysis

A multi-electron and muon pair study of the HERA I data sample, collected by the ZEUS detector between 1994-2000, have resulted in about 200 data events selected in a good agreement with the SM prediction [8]. One of the main selection criteria was at least one identified lepton with $p_T^{lepton} > 5$ $GeV$. A total electroweak $\tau$ pair production cross section predicted by GRAPE-Dilepton, in the same phase space region used for the electron and muon analysis, is two times smaller than muon pair and four times smaller than multi-electron production cross section. The branching ratio that both $\tau$ particles decay leptonically is 12.4% (see Section 7.2.1) and all other decay channels contain at least one hadronically decaying $\tau$ lepton. The $\tau$ identification technique described in Chapter 7 is based on properties of hadronic $\tau$ decays and was used for $\tau$ pair tagging described in this chapter.

An attempt to identify hadronically decaying $\tau$ leptons coming from $\tau$ pair production suffers from immense background. Namely, QCD jets originating from each of the processes described in Section 2.4 are sources of the background. As can be seen from Fig. 8.5, the background exceeds an expected signal by more than four orders of magnitude, which results in a signal-to-background ratio more than one order of magnitude smaller then for isolated $\tau$ search, see Fig. 7.6. Although two $\tau$ leptons are involved, the decay products balance each other and resulting missing transverse momentum in event, $p_T^{CAL}$, is typically small. Missing transverse momentum distribution for $\tau$ pair production simulated by GRAPE-Dilepton and after detector simulation was applied, is shown in Fig. 8.3.

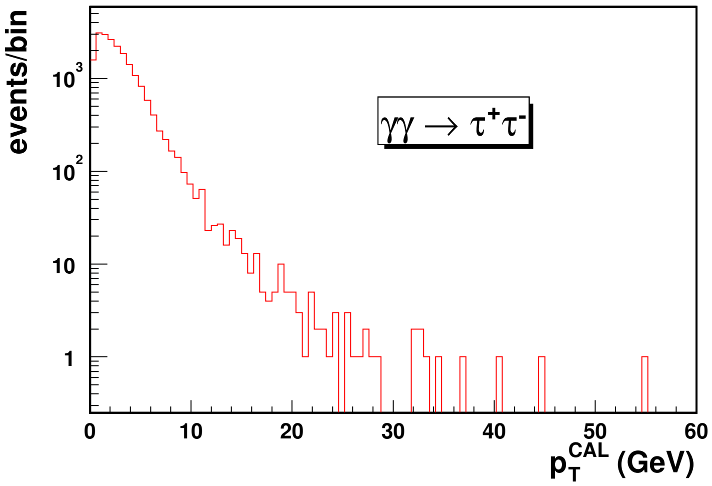


Figure 8.3: Missing transverse momentum in the calorimeter, $p_T^{CAL}$, distribution at the detector level for $\tau$ pair production simulated by GRAPE-Dilepton in the elastic channel.

The simulation was performed in the elastic channel, but very similar distributions were obtained for quasi-elastic and DIS $\tau$ pair production channels.

Therefore, interesting $\tau$ pair events should have one or two $\tau$-like jets and rather low missing transverse momentum. As mentioned, the production cross section decreases very steeply with increasing transverse momentum of produced $\tau$ leptons, see Fig 8.2. In this analysis the requirement $p_T^{jet} > 5\ GeV$, was applied. The requirement tries to keep under control the effects that come from hadronisation and soft particle emissions.

The GRAPE-Dilepton simulation gives a total $\tau$ pair production cross section of $\sigma_{GRAPE} \approx 17.7\ pb$, for 1999-2000 $e^+p$ running conditions and similar results for other running conditions of HERA. At generator level, at least one $\tau$ lepton with $p_T^\tau > 5\ GeV$ and $5^\circ < \theta_\tau < 175^\circ$ were required. If one requires at least one $\tau$ lepton with $p_T^\tau > 10\ GeV$, the cross sections drops to $\sigma_{GRAPE} \approx 1\ pb$. The number of jets in event found by longitudinally invariant $k_T$ cluster algorithm in inclusive mode after $p_T^{jet} > 5\ GeV$ cut was applied, is given in Fig. 8.4.

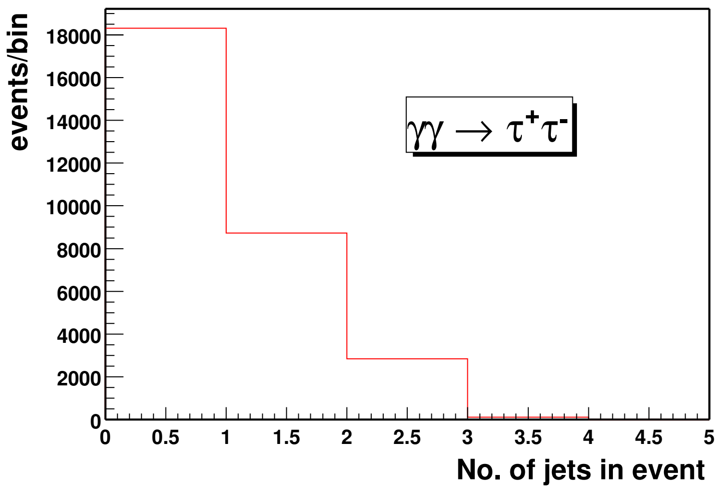


Figure 8.4: Number of jets in event found by longitudinally invariant $k_T$ cluster algorithm in inclusive mode after $p_T^{jet} > 5\ GeV$ cut was applied. The $\tau$ pair simulation was performed using GRAPE-Dilepton elastic production channel.

The algorithm was applied in the same way as described in Section 7.2.3.1 and $\tau$ pair events were simulated by GRAPE-Dilepton in the elastic production channel. Similar distributions were obtained for the quasi-elastic and DIS channels, as well.

As can be seen from the figure, a large fraction of events ($\sim 60\%$) do not contain any reconstructed jet. Although at generator level at least one $\tau$ lepton was required with $p_T^\tau > 5\ GeV$ and $5^\circ < \theta_\tau < 175^\circ$, the effect of $\tau$ decay (neutrino) lowers an outgoing transverse momentum of the hadronic decay products below the $p_T^{jet} > 5\ GeV$ threshold. Of course, the situation improves with increasing $p_T^\tau$, but at the same time the $\tau$ pair production cross section steeply decreases, as described. In addition, it has to be stressed that no rejection was made to remove jets associated to the direction of reconstructed electrons or muons.

Therefore, it is necessary to try to select $\tau$ pair events by tagging only one $\tau$ particle in order to achieve an efficiency of the signal selection required for positive outcome of the search.

Apart from the mentioned problems, i.e. huge background, low signal cross section and limited efficiency of the signal selection, the $\tau$ pair analysis suffers from severe trigger problems, as well. As explained, $\tau$ pair events are usually caracterised by small $p_T$ jet(s) and by low missing transverse momentum. There is no trigger specially designed for these type of events, because of the large background in that "soft" phase space region. The inclusive ZEUS 1-jet trigger has a threshold at $p_T^{jet} > 10\ GeV$ which is high for $\tau$ pair study. The ZEUS inclusive 2-jet trigger has a threshold at $p_T^{jet} > 4$ or $4.5\ GeV$ , depending on the running period of HERA, which results in a low signal efficiency, see Fig. 8.4.

The aim of the study presented in this chapter was to explore actual feasibility of tagging $\tau$ pair events at HERA and to test $\tau$ identification technique with a "$\tau$-sample". For this purpose, a combination of various ZEUS trigger bits, each of them with all ZEUS trigger levels included, was used to achieve an optimal signal efficiency. The optimal trigger combination was the basis for the subsequent analysis.

The list below contains the trigger selection applied to obtain good signal efficiency.

- `ZEUS DST bit 15.` The diffractive trigger requires the pseudorapidity of the most forward going energy flow object (combined calorimeter and tracking information) with an energy measured of more than 400 $MeV$ to be less than 3, $\eta_{max} < 3$. This trigger bit fired also if the *Leading Proton Spectrometer* (LPS), i.e. very forward proton tagger, had recorded an event.

- `ZEUS DST bit 43.` Hotline exotic trigger bit. The trigger is a logical OR of these different requirements: good NC-like event, good CC-like event, at least one muon in event, high $E_T$ event, at least two electrons, Compton scattering like event.

- `ZEUS DST bit 77.` The di-jet trigger requires at least two jets with $E_T^{jet} > 4.5$ $GeV$.

- `ZEUS DST bit 79.` The prompt photon trigger requires at least one good track and electron candidate with $E_T > 3.5\ GeV$ in the pseudorapidity range $-2 < \eta < 2$.

- `ZEUS DST bit 111.` The CC diffractive trigger requires $p_T^{CAL} > 4\ GeV$ and energy deposition in the innermost FCAL ring to be smaller than 1 $GeV$.

- `ZEUS DST bit 115.` The di-lepton trigger requires at least two muons or electrons found in event.

The trigger chain used was a logical OR of the trigger bits given above. The signal efficiencies obtained for this trigger chain were 80%, 73% and 45% for elastic, quasi-elastic and deep inelastic GRAPE-Dilepton $\tau$ pair production channel, respectively.

### 8.2.1 Di-$\tau$ discriminant setup

The only difference from the isolated $\tau$ discriminant setup described in Section 7.2.3 was the choice of signal and background reference jets used to calculate the discriminant value $D$. Namely, jets originated from hadronically decaying $\tau$ leptons from di-$\tau$ simulation were used as signal jets, while photoproduction jets (resolved and direct) were used as background reference jets. Photoproduction is the main source of the QCD jets for this analysis.

#### 8.2.1.1 Control selection used to establish di-$\tau$ discriminant

To obtain sufficient signal and background reference samples, a control analysis largely independent of the actual di-$\tau$ selection was performed.

GRAPE-Dilepton di-$\tau$ simulation was used as the signal, while resolved and direct photoproduction MC simulations (described in Chapter 5) were used as the background sample. The data sample selected to check the quality of the simulation was based on the $e^+p$ data taking period from 1999 to 2000 with integrated luminosity of $\mathcal{L}_{int} = 65\ pb^{-1}$. The main selection requirements were the jet quality and non-$ep$ background rejection. The list below contains the selection criteria applied to obtain the required reference samples.

- `Trigger selection`. The di-jet trigger bit DST 77 selecting events with at least two jets with $p_T^{jet} > 4.5\ GeV$, was required.

- `Non-ep background rejection.`
  - calorimeter timing veto (applied for data only)

- $|z_{vtx}| < 40\ cm$
- $\sqrt{x_{vtx}^2 + y_{vtx}^2} < 0.5\ cm$
- $N_{tracks}^{good} > 0.2 \cdot N_{tracks} - 20$
- additional cosmic event rejection (3-dim opening angle between two tracks $< 178°$)
- beam halo rejection (the energy deposited in the electromagnetic part of the BCAL and RCAL was required to exceed a 10% of the total energy deposited in those parts of the calorimeter, if the total energy exceeded a threshold of 5 $GeV$.

- `Holes in the calorimeter.` See Section 7.3.1.
- `Jet requirements.` Only well reconstructed jets inside the CTD acceptance were selected. Remaining electrons were rejected using the jet electromagnetic energy fraction and the jet energy fraction carried by the most energetic track in the jet. Only events with at least one jet which fulfills these requirements were considered:
  - $p_T^{jet} > 5\ GeV$
  - $15° < \theta_{jet} < 164°$
  - $ltf > 0$
  - $ltf + emfrac < 1.6$
  - $0.1 < emfrac < 0.95$
  - For the signal jets ($\gamma\gamma \rightarrow \tau\tau$ MC simulation) the reconstructed jet had to be matched with a direction of $\tau$ lepton that decayed hadronically (the distance in the $(\eta, \phi)$ plane had to be smaller than one unit), to ensure signal sample of good quality.
- `Number of tracks.` The number of any tracks in event was required to be less than 18. The role of the cut was just to reduce the size of the background sample and to select photoproduction events with not so many tracks, i.e. in the more signal-like region where the background problem is more severe.

The jet observables used to evaluate the discriminant $D$, see Section 7.2.3.1, for a control selection described above are presented in Fig. 8.5. For each event only the jet with largest transverse momentum, $p_T^{jet}$, enters.

The data are fairly described by the photoproduction simulation. Different $\gamma\gamma \rightarrow \tau\tau$ signal and photoproduction background shapes for each of the six variables

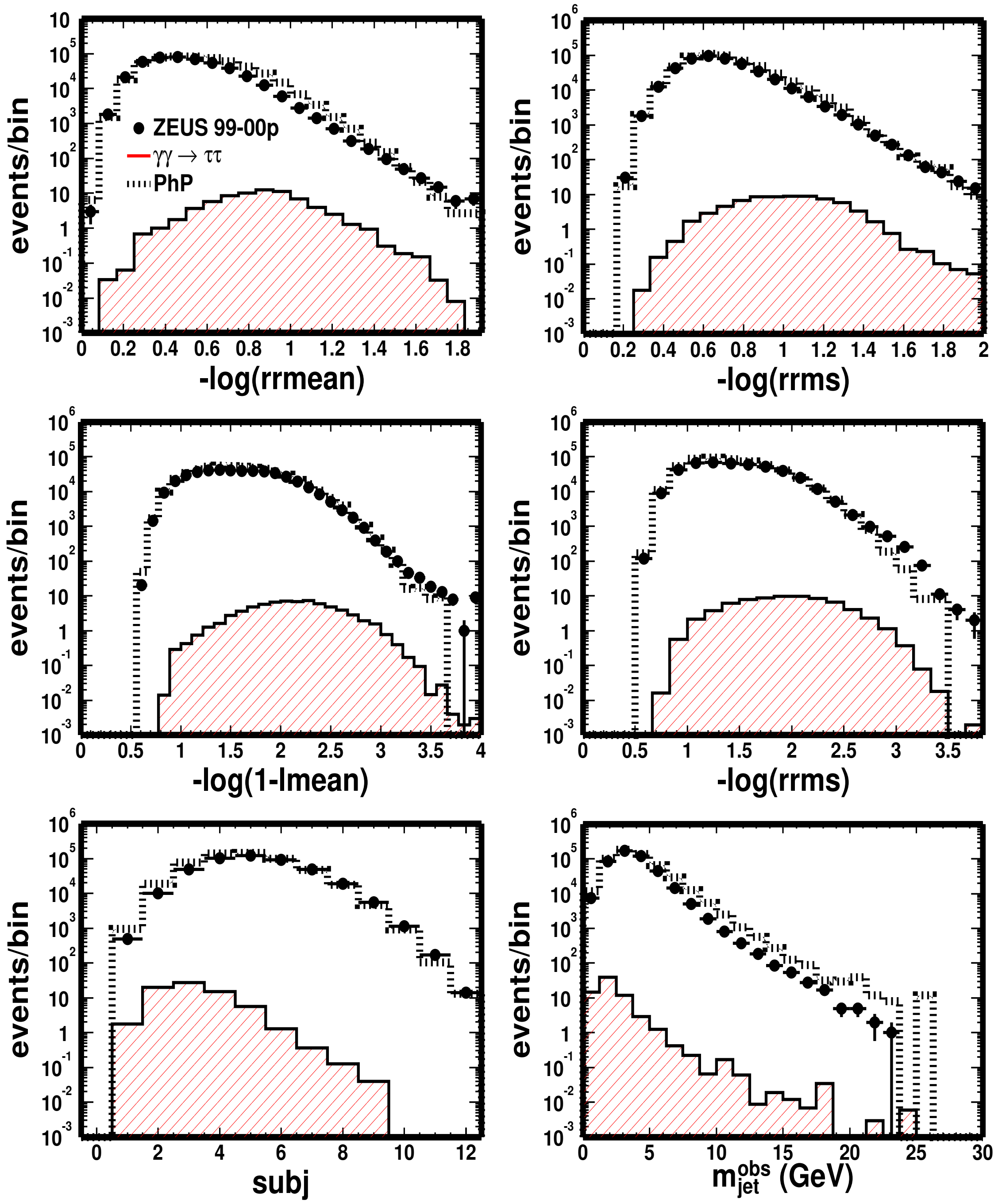


Figure 8.5: Observables characterising the internal jet structure for a control selection described in the text. Shown are the 1999-2000 $e^+p$ data (dots), the simulation of photoproduction events, resolved and direct, (open histograms) and the $\gamma\gamma \to \tau\tau$ MC simulation where $\tau$ decays hadronically (hatched histograms). For each event, only a jet with largest transverse momentum enters.

were obtained and used by the multi-observable discrimination technique to achieve optimal signal-to-background separation. The simulated signal is far below the data.

### 8.2.2 Di-$\tau$ event selection

As mentioned, an attempt to identify hadronically decaying $\tau$ leptons coming from $\tau$ pair production suffers from large background. To cope with the problem, the selection according to the energy deposition in the innermost part of the forward calorimeter was applied. Namely, the typical QCD background, photoproduction and DIS (NC and CC) processes, have substantial "proton remnant" activity which results in significant energy depositions in the inner parts of FCAL. On the other side, GRAPE-Dilepton predicts the biggest contribution for the elastic di-$\tau$ production channel. A combination of GRAPE-Dilepton elastic and quasi-elastic production channels results, largely, in di-$\tau$ events produced without transverse energy recorded in the inner part of the FCAL. Therefore, the veto on the transverse energy deposition in the innermost ring of the FCAL was applied to obtain more background-free sample suitable for an efficient di-$\tau$ tagging.

The GRAPE-Dilepton process was used to simulate the signal di-$\tau$ and the background coming from di-muons and multi-electrons. The generator level requirements were at least one lepton with $p_T^{lepton} > 5\ GeV$ and $5° < \theta_\tau < 175°$. The resolved and direct photoproduction background were simulated as described in Chapter 5 with the generator level cut on the total transverse energy $E_T(had) > 10\ GeV$. The NC DIS and CC DIS MC simulations were performed as in Chapter 5 with the main requirement $Q^2 > 100\ GeV^2$.

The data used in this analysis were collected with the ZEUS detector and correspond to an integrated luminosity of $65.5 \pm 1.5\ pb^{-1}$ for $e^+p$ collisions taken during 1999-2000.

The main di-$\tau$ event selection criteria were the non-$ep$ rejection, veto on the transverse energy deposition in the innermost ring of FCAL, strong $ep$ background rejection and jet quality requirements. Unless otherwise stated, the selection requirements were applied to both data and Monte Carlo simulation events. The list below contains the di-$\tau$ selection criteria applied.

- `Trigger selection.` The trigger chain explained in Section 8.2 was required. Each of the trigger bits had the selection criteria applied at all three levels of the ZEUS trigger chain.

- `Non-ep background rejection.`

- calorimeter timing veto (applied for data only)
- $|z_{vtx}| < 40\ cm$
- $\sqrt{x_{vtx}^2 + y_{vtx}^2} < 0.5\ cm$
- $N_{tracks}^{good} > 0.2 \cdot N_{tracks} - 20$ (good track $p_T$ threshold was 100 $MeV$)
- Additional cosmic event rejection. Events were not considered if they had only two tracks fitted to the primary vertex with $p_T^{track} > 200\ MeV$ and if the tracks had 3-dim opening angle greater than 175°.
- beam halo rejection. The energy deposited in the electromagnetic part of the BCAL and RCAL was required to exceed a 10% of the total energy deposited in those parts of the calorimeter, if the total energy exceeded a threshold of 5 $GeV$.

- `Holes in the calorimeter.` See Section 7.3.1.
- `FCAL` $E_T$ `veto.` No transverse energy deposition in the first inner ring of the forward calorimeter was required.
- `NC DIS rejection.` Only events outside the range 40 $GeV < E - p_z <$ 65 $GeV$ were considered.
- `Track requirements.` Number of good tracks (a track fitted to the primary vertex with $p_T^{track} > 200\ MeV$) and number of any tracks in event had to be two.
- `Number of jets in event.` Number of jets found in event had to be one or two. Only events with one track in an each jet (the $(\eta, \phi)$ distance between a track and jet axis smaller than one unit) were selected.
- `Additional background rejection.` The total energy in the jets subtracted from the sum of uncorrected BCAL and RCAL energies had to be smaller than 2 $GeV$ (c.f. details in the text below).
- `Jet requirements.` The electrons were rejected using standard electron finders, see Chapter 6, and additionally rejected using jet electromagnetic energy fraction and the jet energy fraction carried by the most energetic track in the jet. The moun finder described in Chapter 6 was used to rejet jets associated to the muon direction. Only events with at least one jet which fulfilled these requirements were considered:

- Only jets not associated to the muons and electrons found by muon and electron finders were considered. The $(\eta, \phi)$ distance between muon (electron) and jet axis had to be greater than one unit.
- One track in each jet
- $p_T^{jet} > 5\ GeV$
- $6^\circ < \theta_{jet} < 174^\circ$
- $ltf > 0$
- $ltf + emfrac < 1.6$
- $0.1 < emfrac < 0.95$

The effect of additional background rejection cut, mentioned above, can be seen in Fig. 8.6.

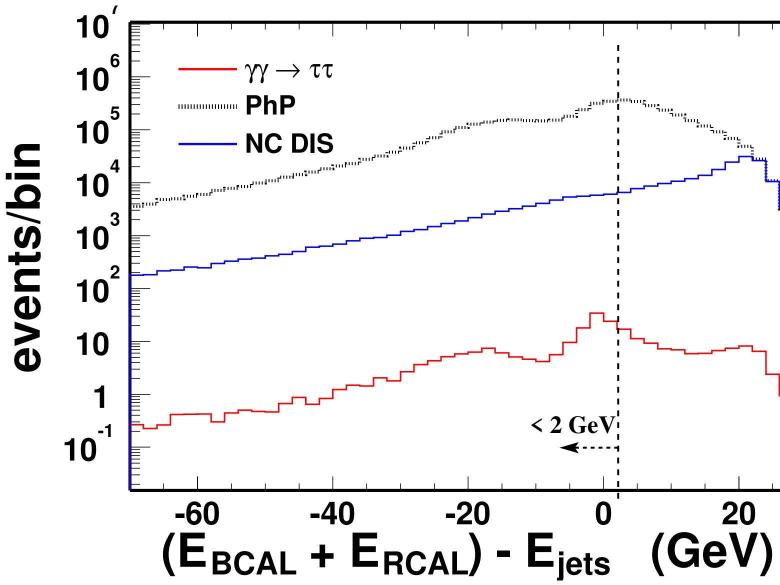


Figure 8.6: Additional *ep* background rejection cut. The distributions obtained by subtraction of the total energy contained in hadronic jets from the sum of uncorrected energy depositions in the BCAL and RCAL, are shown. The photoproduction background (black dotted histogram), NC DIS background (blue dark histogram) and $\gamma\gamma \to \tau\tau$ signal (red light histogram) are shown. The histograms were normalised to the data luminosity. The signal is far below considered background. The analysis requirement was $[(E_{BCAL} + E_{RCAL}) - E_{jets}] < 2\ GeV$.

A good event vertex and jet quality cuts from above were required to obtain Fig. 8.6, i.e. to contribute to the summed jet energy each jet had to fulfill quality cuts described. For the elastic $\tau$ pair production there is no “proton-remnant” activity and, usually, beam electron is not detected in the calorimeter. Therefore, one can expect that significant part of the total energy will be associated to the hadronic jets, considering branching ratios of the $\tau$ lepton. On the other hand, for the photoproduction and NC(CC) DIS processes a large "proton-remnant" activity is expected in the forward region of the detector. In adition, significant "photon-remnant" activity occurs in the rear region for resolved photoproduction process and for NC DIS an electron is measured in the rear part of the detector. In other words, large non-jet energy depositions can be expected in the rear detector region from QCD background processes. Therefore, if the total energy contained in the hadronic jets is subtracted from the sum of energy depositions in the BCAL and RCAL, the shape of resulted distributions for the signal should be different from the QCD background, as can be seen in Fig. 8.6.

### 8.2.3 Results

The $\tau$ discriminant calculated after the requirements described in the previous section were applied, is shown in Fig. 8.7. For each event, the jet with the largest value of the discriminant enters.

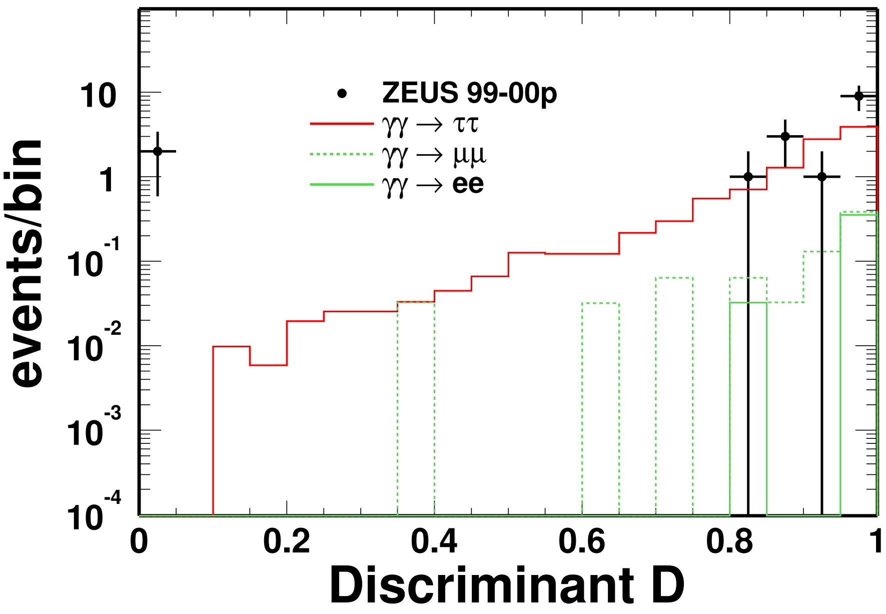


Figure 8.7: Distribution of the $\tau$ discriminant, $D$, for elastic di-$\tau$ selection for data events (dots), di-$\tau$ MC simulation of the signal (red (dark) histogram), the $\gamma\gamma \to ee$ (green (light) histogram) and the $\gamma\gamma \to \mu\mu$ (green (light dashed) histogram) background simulations . The contributions from considered photoproduction, NC DIS and CC DIS simulated samples, were reduced completely. For each event, the jet with the largest value of the discriminant enters.

The data are well described by the di-$\tau$ GRAPE-Dilepton simulation. The QCD background contribution from photoproduction, NC DIS and CC DIS, was rejected completely. Two non-*ep* events coming from the beam halo muons that passed the selection criteria are nicely separated from selected *ep* events at, very small values of the discriminat. The total number of selected data events (without two halo events) is 14 while an expected number of di-$\tau$ signal events is $10.38 \pm 0.13$ and $1.12 \pm 0.85$ is the expectation from multi-electron and di-muon background. The uncertainties quoted are statistical ones. The percentage of unclassified signal di-$\tau$ MC events were 0.4%, while there were no unclassified data and background events. The discriminant strongly peaks at large values as it is expected for the signal events.

Event properties for the di-$\tau$ selection, two halo events were removed, are presented in Fig. 8.8.

The data are well descibed by the di-$\tau$ signal simulation. For jet properties given, each event is represented by the jet with largest value of the transverse momentum, $p_T^{jet}$.

The invariant mass distributions calculated from jet properties (if a track was associated to the reconstructed jet), or from the track properties (if a track could not be associated to the reconstructed jet), are shown in Fig. 8.9.

The GRAPE-Dilepton MC simulation of the $\tau$ pair signal process describes the data well.

Event displays [114] of two di-$\tau$ candidate events are given in Fig. 8.10.

The first $\tau$ pair candidate event contains two hadronically decaying $\tau$ leptons, while the second event contains one muonic and one hadronic $\tau$ decay.

Event properties of all selected data events are presented in Table 8.1.

## 8.3 Summary and discussion

The di-$\tau$ study was performed using an integrated luminosity of $\mathcal{L}_{int} = 65 \pm 1.5$ $pb^{-1}$ collected from 1999 to 2000 $e^+p$ running. The event selection was applied to isolate the elastic di-$\tau$ data sample suitable for the study of $\tau$ identification technique and to explore the actual feasibility of tagging $\tau$ pair events at HERA.

14 data events were selected while the expected number of di-$\tau$ signal events was $10.38 \pm 0.13$ and $1.12 \pm 0.85$ was the expectation from multi-electron and di-muon background. The considered QCD background from photoproduction, NC

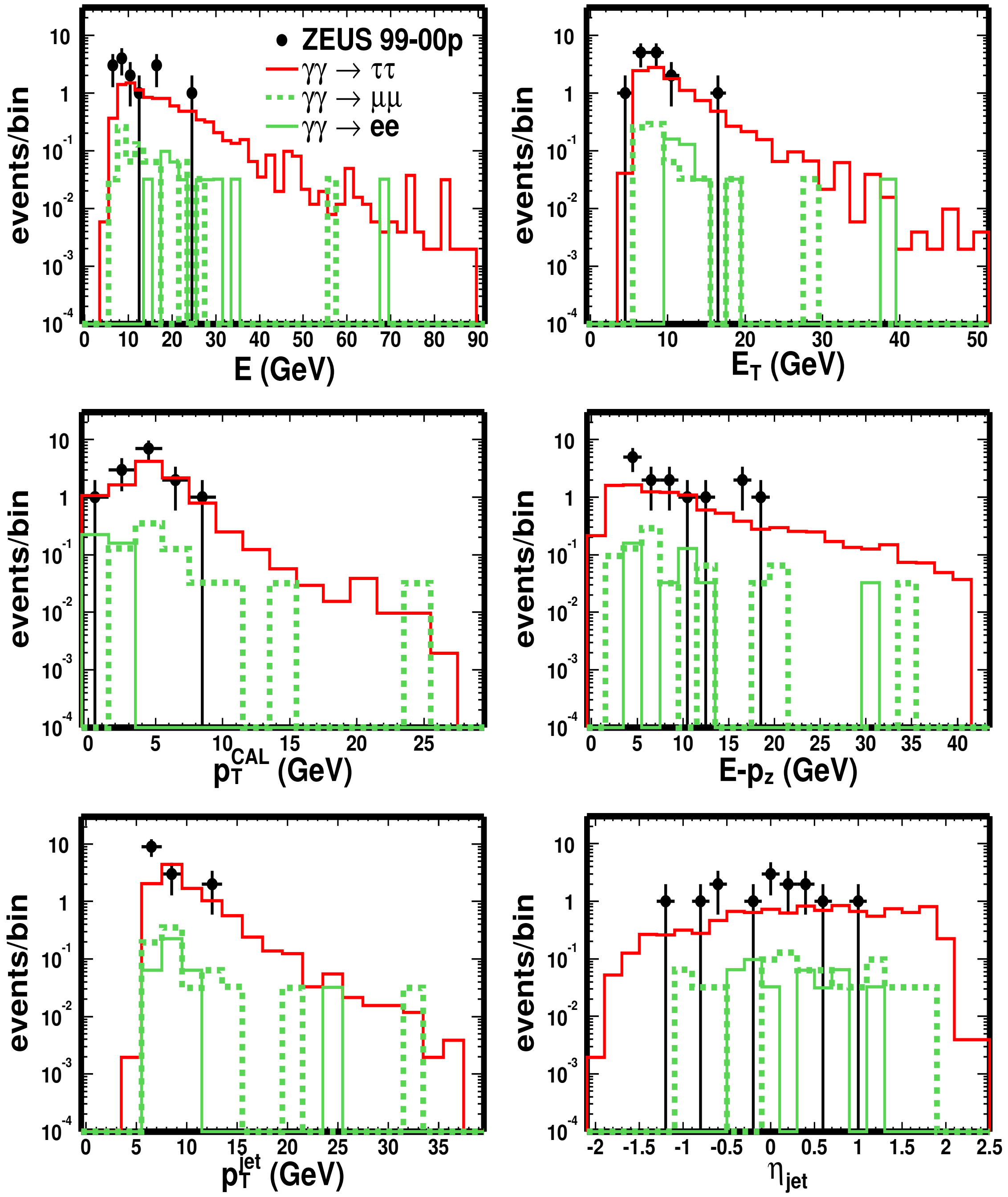


Figure 8.8: Event properties for the di-$\tau$ selection, the 1999-2000 $e^+p$ data (dots), the $\gamma\gamma \to \tau\tau$ signal (red (dark) histogram), the $\gamma\gamma \to ee$ (green (light) histogram) and the $\gamma\gamma \to \mu\mu$ (green (light dashed) histogram) background simulations. Given are: the total energy, the transverse energy, the missing transverse momentum, $E - p_z$, the transverse momentum and pseudorapidity of a jet. If there were two jets, for each event the jet with higher transverse momentum entered. The contributions from considered photoproduction, NC DIS and CC DIS samples, were reduced completely.

| run/event number | No. of jets in event | jet discriminant | $M_{\tau\tau}$ $(GeV)$ |
|---|---|---|---|
| 34226/56472 | 1 | 0.97 | 0.5 |
| 34287/91187 | 1 | 0.96 | 0.24 |
| 35373/50232 | 1 | 0.90 | 13.5 |
| 35450/51840 | 2 | 0.95 | 30.7 |
| | | 0.93 | |
| 35775/106413 | 1 | 0.98 | 0.6 |
| 35814/18072 | 1 | 0.96 | 0.6 |
| 36052/5532 | 1 | 0.84 | 0.7 |
| 36413/59018 | 1 | 0.95 | 1.0 |
| 36556/44871 | 1 | 0.98 | 0.7 |
| 36674/11135 | 1 | 0.96 | 1.4 |
| 36879/99713 | 1 | 0.88 | 0.31 |
| 36952/6795 | 2 | 0.95 | 18.3 |
| | | 0.95 | |
| 36998/3690 | 1 | 0.95 | 0.4 |
| 37435/61549 | 1 | 0.89 | 0.8 |

Table 8.1: Properties of the di-$\tau$ candidate events. For events with two reconstructed jets, the discriminat values are given for both jets.

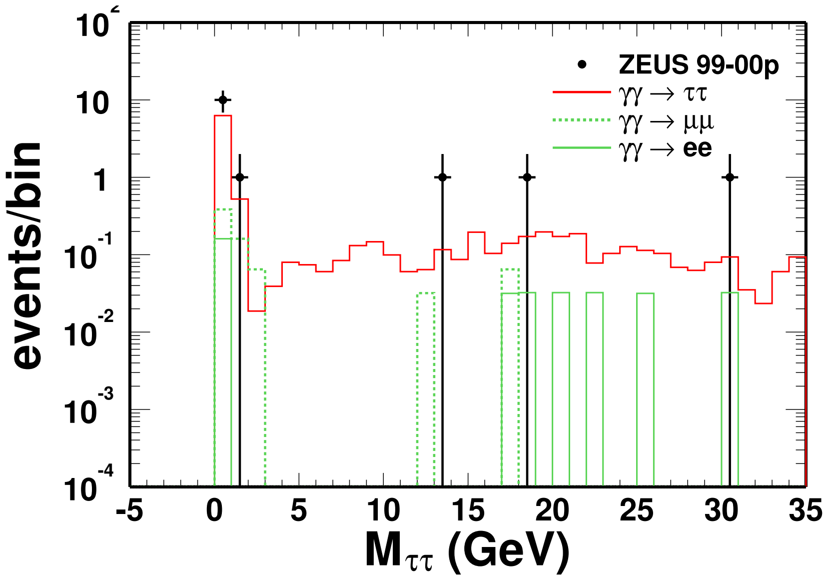


Figure 8.9: An invariant mass distributions for di-$\tau$ selection, the 1999-2000 $e^+p$ data (dots), the $\gamma\gamma \to \tau\tau$ signal (red (dark) histogram), the $\gamma\gamma \to ee$ (green (light) histogram) and the $\gamma\gamma \to \mu\mu$ (green (light dashed) histogram) background simulations. The calculation was performed using jet properties, if the track was associated to the reconstructed jet, or from the track properties, if the track could not be associated to the reconstructed jet. The contributions from photoproduction, NC DIS and CC DIS samples, were reduced completely.

DIS and CC DIS processes was reduced completely.

All selected events have at least one jet with large $\tau$ disriminant, $D > 0.80$, value associated to hadronically decaying $\tau$ leptons in agreement with the di-$\tau$ MC simulation. Based on the number of events in the data and di-$\tau$ MC simulation, and on the shape of distributions shown in Fig. 8.8, it can be concluded that the $\tau$ identification technique is applicable at low $p_T^\tau$ region. In addition, the actual feasibility of tagging $\tau$ pair events at HERA has been shown.

As mentioned, the main aims of the study were a confirmation of the $\tau$ method and di-$\tau$ tagging accessibility. Hence, the di-$\tau$ discriminant obtained was presented as the result of analysis. However, this valuable information could be used as a preselection requirement for possible future studies, which could allow to relax stringent requirements applied for this analysis and to increase the statistics. That would give more possibilities to study an inelastic di-$\tau$ production (without veto on transverse energy depositions in the inner parts of FCAL) where the background problem is more severe.

Hadronic $\tau$ lepton decays into three charged particles (3-prong decays) were not included in the analysis for the large background reasons and missmeasurement

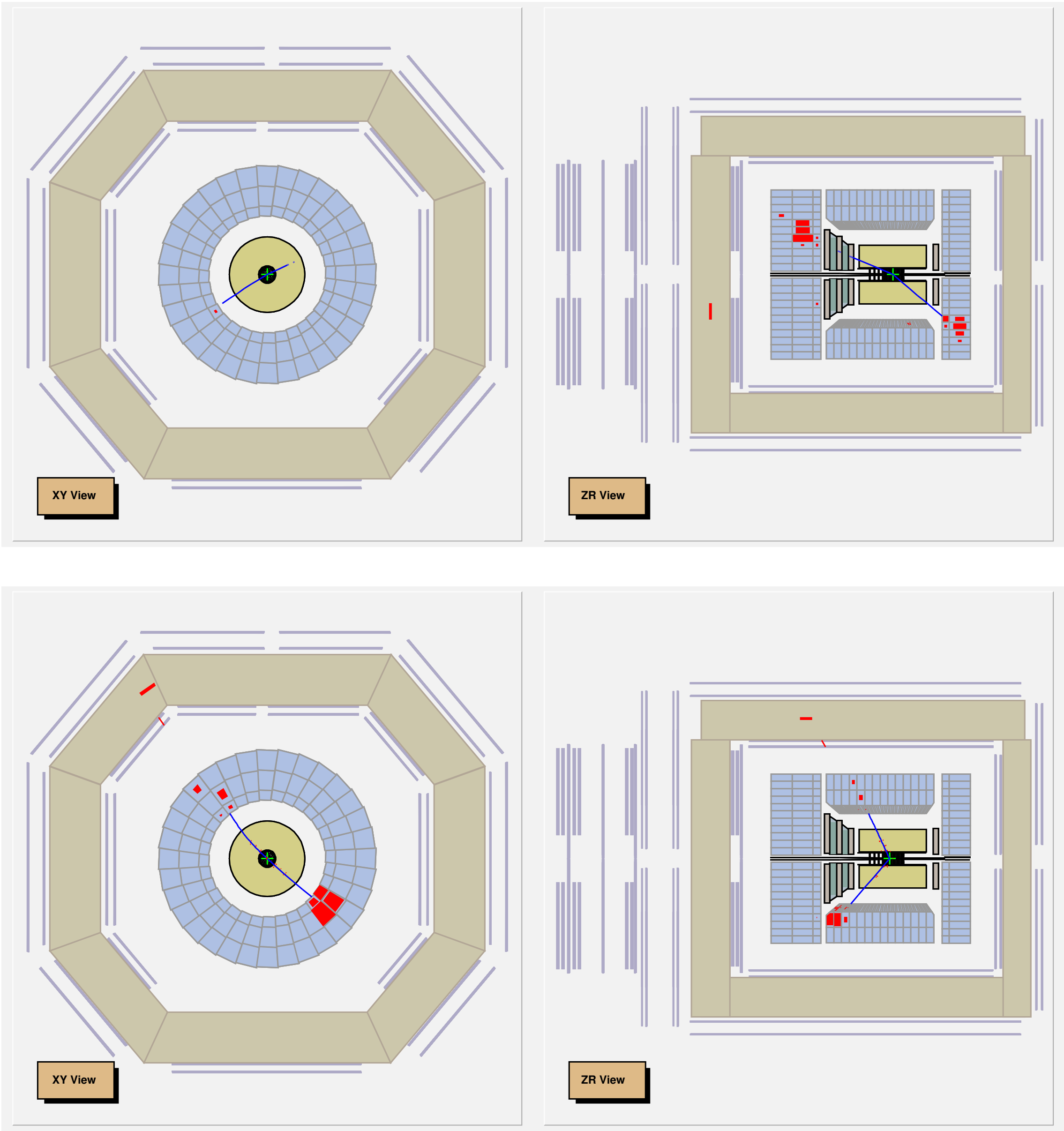


Figure 8.10: Di-$\tau$ candidate events from $e^+p$ interactions at $\sqrt{s} = 318\ GeV$ in the ZEUS detector. The energy deposition in the CAL is proportional to the size of shading in the CAL cells. In the $xy$ view, only the energy deposition in the barrel calorimeter is shown. The first event contains two hadronically decaying $\tau$ leptons, while the second event contains one muonic and one hadronic $\tau$ decay. Selected event variables for the two candidates are given in Table 8.1. The most inner part shown in black is, newly installed (2001), silicon microvertex detector not used for this analysis.

probabilities are more prominent for this channel than for 1-prong decays. Namely, tracks can be too close to be separated by the fitting procedure, or some of tracks can be out of the acceptance required, or can have too small $p_T$, or a QCD jet can be close by the $\tau$ jet, etc.

In adition, the leptonic di-$\tau$ tagging, specially the decay into one electron and one muon, should be explored in order to have complete picture of $\tau$ pair production at HERA. The branching ratios for leptonic $\tau$ decays are considerably lower than hadronic ones, but much more background free.

# CHAPTER 9
# SEARCH FOR NON-SM LIGHT HIGGS BOSON AT HERA

The only fundamental particle not yet discovered of the Standard Model is the Higgs particle, which is connected to the origin of mass. The future of high energy physics is intimately connected to an outcome of the search for this particle. Whether and what kind of Higgs boson will be found, i.e. the nature of particle masses, are hotly pursued questions in particle physics today.

This chapter describes a study of search perspectives for non-SM Higgs particle at HERA.

## 9.1 Introduction and search motivations

In this section, a short description of the Higgs mechanism and SM Higgs predictions are presented, as well as a detailed introduction to expectations in the Higgs sector beyond the SM.

### 9.1.1 The Higgs mechanism and SM Higgs boson

One of the most profound insights in theoretical physics is that interactions are governed by symmetry principles. This powerful statement has been repeatedly exploited to obtain the most fundamental knowledge in all branches of physics. The reason why the symmetry principles are so efficient can be best seen in Lagrangian Field Theory where symmetries (invariance of a system under some transformation) are directly connected to particular conservation laws (such as conservation of electric charge, momentum, energy, etc.). The present belief is that all interactions may be dictated by so called *local gauge symmetries*. In summary, the electromagnetic and strong interactions come as a product of local phase (gauge) invariance of the Lagrangian, and local means that the phase is a space and time dependent quantity. Moreover, the local gauge invariance dictates that both photons and gluons should be massless. How can we apply such symmetry to the weak interactions which are mediated by massive $W^{\pm}$ and $Z^0$ particles? Just to ignore symmetry principles and to put by hand the mass terms in the Lagrangian leads nowhere, because the theory becomes incalculable. Fortunately, there is a way how to preserve local gauge invariance and introduce masses for the weak force quanta, at the same time. The answer is the so called *Spontaneous Symmetry Breaking*, see Fig. 9.1.

To respect the structure of the Standard Model a doublet of complex scalar

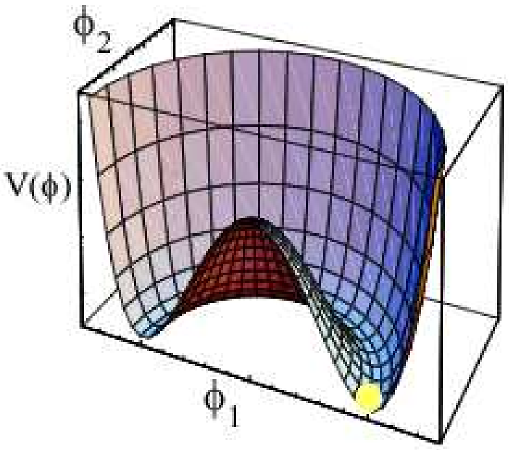


Figure 9.1: A particular choice of ground state of the potential $V(\phi)$ breaks the symmetry.

fields with a quartic potential is introduced. The only new thing which is introduced by symmetry breaking is that a particular ground state (or stable vacuum) of scalar fields is chosen. The SU(2) symmetry of the (previously symmetrical) Lagrangian has been broken by the choice of the ground state, illustrated by the choice of yellow point in Fig. 9.1. This symmetry breaking may look totally artificial, but it is not. Other physical systems are known in which the ground state does not possess the symmetry of the Lagrangian, such as superconductors, crystal lattices or the famous buckling of a compressed needle. Moreover, our knowledge in particle physics come from perturbation theory in which the fluctuations arround the stable minimum point are calculated. It seems that nature made a choice, as well, cause different choice would lead to different physical realities.

The strict application of this idea to the proper group representation of the Standard Model results in massive gauge bosons we looked for to be associated with the $W^{\pm}$ and $Z^0$ particles. This mechanism of mass generation is called *the Higgs mechanism*. There are other "miracles" of the Higgs mechanism. The full theory is again calculable (renormalisable) and the same symmetry breaking mechanism which generates $W^{\pm}$ and $Z^0$ masses is also sufficient to give masses to the leptons and quarks. The minimal configuration which results in the desired features of the theory and respects the SM group structure is one Higgs doublet configuration and there should exist an extra particle called *Higgs boson* associated to the breaking mechanism. It is interesting to mention that masses of the particles are not a result of emission and absorption of quanta of the scalar field, but come as a result of the interaction with the "classical" part of the scalar field, which extends over all space

[110].

However, despite all success, the Higgs sector of the SM is the least satisfactory one and least well-determined aspect of electroweak gauge theory. The masses of the fermions and Higgs particle itself are just parameters and are not predicted by the theory. However, the theory predicts that the Higgs coupling to the fermions is proportional to their masses. This prediction could be examined when, and if, the Higgs boson is actually observed.

There are theoretical arguments why the SM Higgs boson should be neither very light ($M_{h(SM)} \geq 10\ GeV$) nor very heavy ($M_{h(SM)}$ should be smaller than a few hundred $GeV$).

The most dedicated search for the Higgs particle, so far, has been performed at the LEP collider at CERN. The combined LEP results have excluded the SM Higgs boson with a mass below 114.4 $GeV$ at 95% confidence level [10]. This limit makes searches for the SM Higgs boson at the *ep* HERA collider hopeless, because of very low production rates and large backgrounds (at HERA the expected cross section is well below 0.01 *pb* for the mass range mentioned [93]).

### 9.1.2 Two Higgs Doublets Model (2HDM)

It is not at all obvious whether the source of mass lies within the Standard Model. It could be that it requires a wider scenario. The Higgs boson search perspectives at the HERA collider change drastically if the minimal extension of the Standard model in the Higgs sector is considered. This minimal extension of the Higgs sector is to include a second Higgs doublet to the symmetry breaking mechanism:

$$\mathbf{\Phi_1} = \begin{pmatrix} \phi_1^+ \\ \phi_1^0 \end{pmatrix}, \quad \mathbf{\Phi_2} = \begin{pmatrix} \phi_2^+ \\ \phi_2^0 \end{pmatrix}.$$

After spontaneous symmetry breaking two vacuum expectation values (ground states) appear:

$$\langle \mathbf{\Phi_1} \rangle = \begin{pmatrix} 0 \\ \frac{v_1}{\sqrt{2}} \end{pmatrix}, \quad \langle \mathbf{\Phi_2} \rangle = \begin{pmatrix} 0 \\ \frac{v_2}{\sqrt{2}} \end{pmatrix}.$$

One constraint for extended Higgs sector is the experimental observation that

| couples to | type I | type II | type III | type IV |
|---|---|---|---|---|
| down-type leptons | $\mathbf{\Phi_2}$ | $\mathbf{\Phi_1}$ | $\mathbf{\Phi_2}$ | $\mathbf{\Phi_1}$ |
| up-type quarks | $\mathbf{\Phi_2}$ | $\mathbf{\Phi_2}$ | $\mathbf{\Phi_2}$ | $\mathbf{\Phi_2}$ |
| down-type quarks | $\mathbf{\Phi_2}$ | $\mathbf{\Phi_1}$ | $\mathbf{\Phi_1}$ | $\mathbf{\Phi_2}$ |

Table 9.1: The couplings of the Higgs fields to fermions according to the four types of 2HDMs.

the value of $\rho = M^2_{W^\pm}/(M^2_Z cos^2\theta_W) \approx 1$, where $\rho$ parametrises the relative strength between Charged Current and Neutral Current weak interactions. The condition of $\rho \approx 1$ is automatically met by models with only Higgs doublets, while for the other possible Higgs multiplets is not the case.

There are several possibilities how new fields may couple to fermions. Four types of 2HDMs are considered in order to avoid introduction of flavour changing neutral currents (FCNC) [94]. The four types differ in the way the new Higgs fields couple to fermions, see Table 9.1.

In this study the CP-conserving 2HDM type II is considered where $\mathbf{\Phi_1}$ couples to the down quarks and charged leptons and the $\mathbf{\Phi_2}$ couples to the up quarks. The Higgs sector of the *Minimal Supersymmetric Standard Model* (MSSM) has a structure of 2HDM type II.

The general 2HDM type II has six free physical parameters [94] and can be parametrised by the masses $M_h, M_H, M_A, M_{H^\pm}$ and two dimensionless parameters $\alpha$ and $tan\beta$, $\alpha$ being the mixing parameter in the neutral Higgs sector, and $tan\beta = v_2/v_1$ being the ratio of the two vacuum expectation values $v_2$ and $v_1$.

The 2HDM has five Higgs particles: two neutral Higgs scalars $h$ and $H$, one neutral pseudoscalar $A$, and a pair of charged Higgs bosons $H^\pm$.

The Higgs sector in the MSSM is a special case of a 2HDM type II model. Due to relations imposed by supersymmetry only two free parameters remain, $\alpha$ and $tan\beta$, at so called tree level. Direct searches at LEP in the MSSM scenario have set limits on the Higgs masses and parameter space. In a parameter scan where the parameter combination was chosen to give a maximal predicted mass $M_h$, the masses $M_h$ and $M_A$ (two lightest Higgses) smaller than 88.4 $GeV$ for $tan\beta > 0.4$ have been excluded at 95% confidence level [95]. Therefore, light neutral and charged Higgs bosons are well excluded in the MSSM and if there exists light Higgs particle it is very unlikely that it comes from the MSSM.

Many searches for a light Higgs particle in the general 2HDM type II were performed at various energies and machines. The most systematic studies have been performed at LEP. There are three main processes for Higgs production within the LEP energy range, *Higgsstrahlung, associated production* and *Yukawa* process depicted in Fig. 9.2, of which only the first process plays an important role in the Standard Model. The Standard Model couplings are modified by additional factors $sin^2(\beta - \alpha)$ and $cos^2(\beta - \alpha)$ for Higgsstrahlung and associated production, see Fig. 9.2.

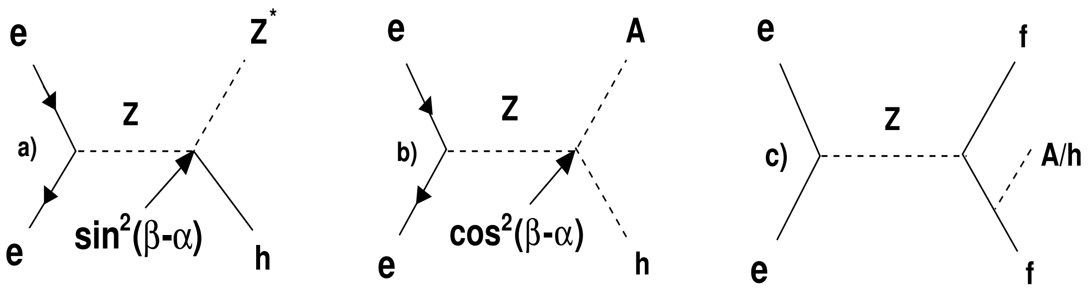


Figure 9.2: The three dominant Higgs production processes in a 2HDM at LEP: a) The Higgsstrahlung, b) associated production and c) the Yukawa process.

The HERA collider cannot compete with results of LEP and other experiments' for the majority of parameter space, but for an attractive phase space region where the LEP and other experiments are suppressed HERA could contribute significantly. Namely, if $sin^2(\beta - \alpha) \sim 0$ the Higgsstrahlung process is suppressed and the neutral Higgs boson pair production (associated process) can be suppressed kinematically, if $M_h + M_A > M_Z$. In that case, LEP is sensitive only via the Yukawa process and present constraints allow the existence of *one* neutral light Higgs boson.

The current constraints are shown in Fig. 9.3, where the limits from LEP, Tevatron and other lower energy experiments are presented for h (scalar) and A (pseudoscalar) Higgs bosons in the "HERA favourable" phase space region, where $\beta - \alpha = 0$. The $\beta - \alpha = 0$ assumption leads to equality in the strength in the coupling of fermions to scalars and pseudoscalars [96]. The 95% CL current constraints presented in Fig. 9.3 come from an analysis of $(g-2)_\mu$ data [12, 97] (allowed region is between thick dashed lines) together with the upper limit from LEP, from the Yukawa process [98], and the lower limits from the $Z \rightarrow h(A)\gamma$ [99]. In adition, the upper 90% CL limits from $\Upsilon$ decay (lines marked K [100], N [101] and L [102], with K results rescaled by a factor 2, as discusses in [103]) and from Tevatron collider

[104], are shown as well.

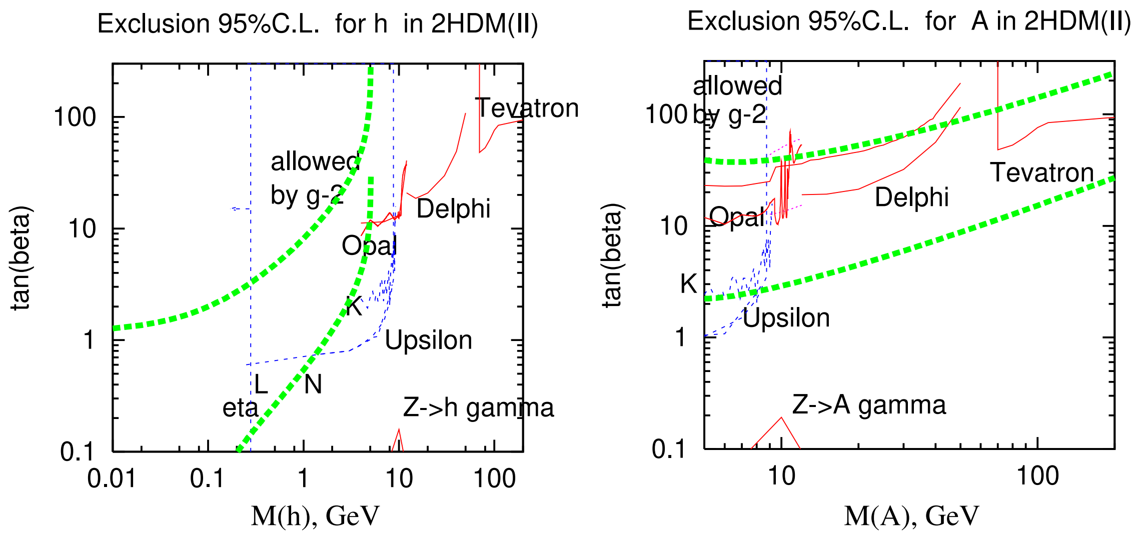


Figure 9.3: Current 95% CL constraints for h (left) and for A (right) Higgs, requiring $\beta - \alpha = 0$. The $(g-2)_\mu$ data give the allowed region between thick dashed lines. Also the upper limits from LEP Collaborations (ALEPH, DELPHI, OPAL), Tevatron, as well as constraints from the $\Upsilon$ decay into $h(A)\gamma$ and the $\eta$ decay (for $h$ only) are presented. The lower limits from LEP measurements of $Z \to h(A)\gamma$ are shown as well. More details in the text.

The combined constraints allow for the exsistence of a 2HDM type II pseudoscalar Higgs boson $A$ with masses $M_A \geq 8\ GeV$ and $tan\beta$ between $\sim 2$ and 100. For a light scalar $h$ the combined constraints are more severe. If the old limits from $\Upsilon$ decay data are taken into account, the allowed area disappears.

As will be described in the next section, there is a significant potential for HERA collider to explore the unconstrained region.

Finally, in the 2HDM there is an important lower limit on the mass of $H^+$, coming from the NLO analysis of the $b \to s\gamma$, $M_{H^+} \geq 500\ GeV$ at 95% CL [108]. In adition, in the MSSM one expects $M_{H^\pm} > M_W$ [96].

## 9.2 Predictions for the Light Higgs productions at HERA

The possibilities of Higgs searches at the HERA collider have been considered during the HERA Workshop in 1987 [105]. Specially, non-minimal (non-SM) Higgs boson production at HERA has been considered, and investigated in more details in other publications [106, 107, 96].

The parameter space was chosen according to the existing limits from other experiments. Namely, the $\alpha = \beta$ assumption which leads to $sin^2(\alpha - \beta) = 0$ is a direct consequence of the LEP finding that $sin^2(\alpha - \beta) < 0.1$ [109]. In addition, only one $h$ or $A$ Higgs particle can be really light to explore the phase space above the LEP kinematic limit ($M_h + M_A > M_Z$). As mentioned in the previous section, $\alpha = \beta$ assumption leads to equality in the strengths in the coupling of fermions to scalars and pseudoscalars[1]. The scenario with large $tan\beta \sim \mathcal{O}(m_t/m_b)$ has been considered which implies large enhancement in the coupling of both $h$ and $A$ bosons to the down-type quarks and leptons, while the couplings to up-type quarks are suppressed by the same factor. The large $tan\beta$ scenario therefore explains a large ratio between top and bottom quark masses by a large ratio of the vacuum expectation values ($tan\beta = v_2/v_1$).

At the HERA accelerator the production of light neutral 2HDM Higgs boson $h$ (or $A$) is expected to proceed via two main photoproduction channels: *bremsstrahlung of the Higgs boson*, $\gamma g \rightarrow b\bar{b}h(A)$, as sketched in Fig. 9.4, and *gluon-gluon fusion via a quark loop*, $gg \rightarrow h(A)$, shown in Fig. 9.5. The $ZZ$ and $WW$ fusions are not relevant since the pseudoscalar, $A$, does not couple to weak gauge bosons, and the scalar couplings are put to zero by the assumption $\alpha = \beta$.

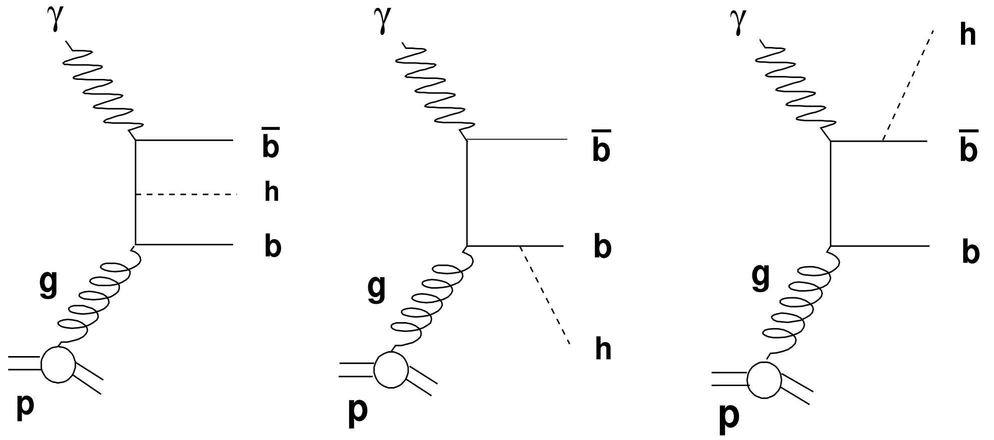


Figure 9.4: The $\gamma g \rightarrow b\bar{b}h$ in $\gamma p$ scattering at HERA.

These processes have been studied in detail [106, 13] and the cross sections have been calculated using the assumptions mentioned above. For the specific value of $tan\beta = 30$ the calculated cross sections are plotted in Fig. 9.6 versus the Higgs

[1]In 2HDM fermions couple to the pseudoscalar proportionally to $(tan\beta)^{\pm 1}$ whereas the coupling of the fermions to the scalar $h$ goes as $(sin\alpha/cos\beta)^{\pm 1}$. Here the sign $\pm$ coresponds to isospin $\mp 1/2$ components

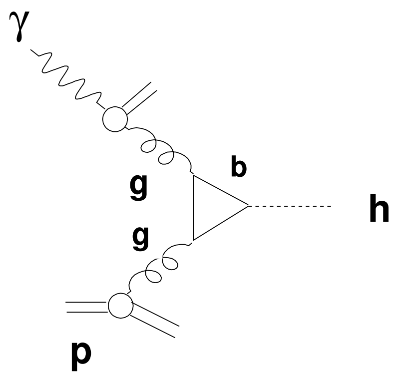


Figure 9.5: The $gg \rightarrow h$ in $\gamma p$ scattering at HERA.

mass $M_h$, where the $\gamma g \rightarrow b\bar{b}h$ process is denoted by $''\gamma g''$ and $gg \rightarrow h$ process is denoted by $''gg''$. The $\gamma p$ centre of mass energy considered was $\sqrt{S_{\gamma p}} \simeq 170$ $GeV$ ($E_\gamma = 9$ $GeV$ and $E_p = 820$ $GeV$) and photon and proton PDFs used were GRV(LO) and MRSD'$_-$, respectively. The choice of alternative photon and proton parametrisation does not change the cross sections significantly. The similar results also hold for the pseudoscalar particle $A$ within the same mass range. A comparison of $gg$ fusion with $\gamma g$ shows that $gg$ process clearly dominates for masses below $\sim 45$ $GeV$ where the cross section is significant. For smaller values of $tan\beta$ the production cross section decreases, but the $gg$ fusion dominates even in that region.

The results of the total cross section calculation indicate that for $tan\beta \simeq 30$ there is a chance to observe the Higgs boson at HERA for $M_{h(A)} \leq 30$ $GeV$. Assuming 200 $pb^{-1}$ of HERA $ep$ luminosity the prediction is approximately 900 events produced for $M_{h(A)} = 5$ $GeV$ and about 10 events for $M_h = 30$ $GeV$ at $\sqrt{S_{\gamma p}} = 170$ $GeV$ [13]. The number of predicted events does not change significantly for different running conditions of the HERA accelerator.

The $gg$ fusion clearly dominates the cross section for an interesting phase space region and an independent analysis of the expected background has been performed [13]. Only $gg$ Higgs production process will be considered here.

The Higgs decay channels $h(A) \rightarrow \tau^+\tau^-$ or $\bar{b}b$ are most important since in 2HDM type II with large $tan\beta$, $h$ and $A$ decay mainly to the heaviest available "down-type" fermions. The study performed predicts that for the $\bar{b}b$ final state the background is too large, therefore the decay into $\tau$ pairs is the most promising

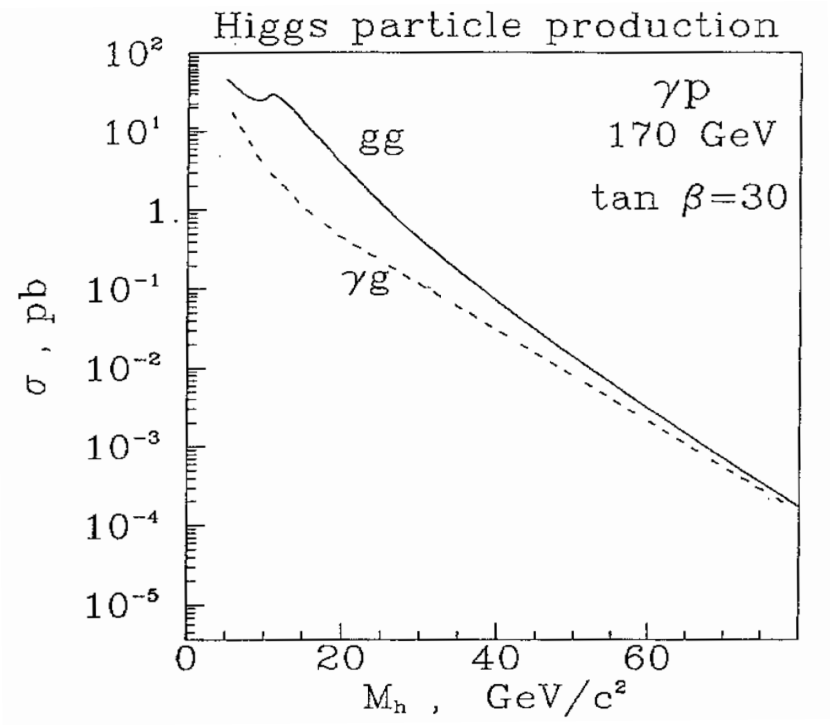


Figure 9.6: Cross sections for the 2HDM neutral Higgs scalar h production (similar results for pseudoscalar $A$) in $\gamma p$ scattering at $\sqrt{S_{\gamma p}} = 170\ GeV$ via gluon-gluon fusion and $\gamma g$ channel as function of $M_h$ [13]. The details can be found in the text.

channel to search for. In the mass range below the $\bar{b}b$ threshold and above the $\tau^+\tau^-$ the branching ratio of the Higgs particle decay to $\tau^+\tau^-$ pair is almost one, and above the $\bar{b}b$ threshold (i.e. above 10 $GeV$) it is of the order of 1/10.

One of the largest expected backgrounds to $h(A) \to \tau^+\tau^-$ search comes from the process described in Chapter 8, $\gamma\gamma \to \tau^+\tau^-$. To distinguish between two processes a more detailed information about a final state topology is needed. It is useful to analyse the rapidity distribution, $y$, in the $\gamma p$ centre of mass system of the Higgs boson and of the $\tau$ pair produced in $\gamma\gamma \to \tau^+\tau^-$ process. For $gg$ fusion into $h$ the transverse momentum of $h$ is negligible and therefore the rapidity represents the longitudinal motion of the Higgs boson along the direction of initial particles (the same is valid for $\tau$ pairs from $\gamma\gamma \to \tau^+\tau^-$ reaction). The rapidity can be written as

$$y = -\frac{1}{2} log \frac{E_h - p_h}{E_h + p_h} = -\frac{1}{2} log \frac{x_\gamma}{x_p}.$$

The $x_\gamma$ variable gives the fraction of the photon momentum participating in the hard scattering. The $y$ distribution of the 2HDM neutral Higgs $h$ in $\gamma p$ scattering at $\sqrt{S_{\gamma p}} = 170\ GeV$ via gluon-gluon fusion and the $y$ distribution of $\tau$ pairs from

$\gamma\gamma \to \tau^+\tau^-$ background are shown in Fig. 9.7 [13].

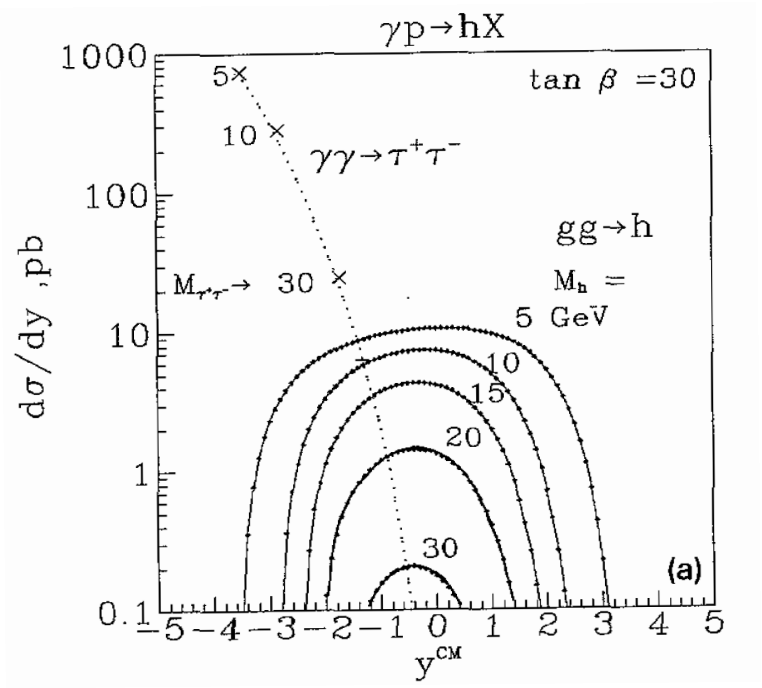


Figure 9.7: The rapidity distribution of the 2HDM neutral Higgs scalar $h$ production in $\gamma p$ scattering at $\sqrt{S_{\gamma p}} = 170\ GeV$ via gluon-gluon fusion (solid curves) and $\gamma\gamma \to \tau^+\tau^-$ (dashed line) for different masses of the Higgs scalar $M_h$ (in $GeV$) and $M_{\tau^+\tau^-}$ of $5, 10, 15, 20$ and $30\ GeV$ [13].

The calculation is done in the $\gamma p$ centre of mass system with positive $y$ in the proton direction. One can see that for the light Higgs case the cross sections are largest around $y \sim 0$, which corresponds to gluon scattering with $x_\gamma \simeq x_p$. This is explained by the fact that the gluon distributions in the photon and in the proton decrease rapidly with increasing $x$ and the smallest $x$ from both sides are preferred. On the other hand, the background due to $\gamma\gamma \to \tau^+\tau^-$ has always negative rapidities. The positive rapidity region is not allowed kinematically for this process. Here, the photon interacts directly with a fixed energy, $x_\gamma = 1$, and therefore $y_{\tau^+\tau^-} = -\frac{1}{2} log \frac{1}{x_p} \leq 0$. It is obvious from the Fig. 9.7 that the rapidity distribution in the $\gamma p$ centre of mass frame can be very useful to reject the $\gamma\gamma \to \tau^+\tau^-$ background.

The other sources of $\tau$ background like $q\bar{q} \to \tau^+\tau^-$ processes contribute to both positive and negative rapidity distributions with flat and relatively low cross sections (below 0.5 $pb^{-1}$) in the central region ($y \sim 0$).

To summarise, the size and shape of the expected signal for the Higgs decay mode $h(A) \to \tau^+\tau^-$ should help to tag interesting events in the $\tau^+\tau^-$ channel.

## 9.3 Description of the analysis

The study presented in the previous section predicts considerable discovery and exclusion potential for non-minimal (2HDM) Higgs boson at the HERA accelerator.

However, to explore search perspectives further more it is necessary to analyse full detector response to the underlying Higgs production mechanism and get more realistic insight of the tagging possibilities. The section presents MC simulations used to exploit Higgs search perspectives in more details, as well as results obtained.

### 9.3.1 Event simulation

Light Higgs $gg \to h \to \tau^+\tau^-$ process in $ep$ collisions were simulated using the PYTHIA program [111]. Events were generated in the LO resolved photoproduction mode, proton PDFs involved were GRV94 LO and photon PDFs were SaS2D. The cross section used for $gg \to h$ process simulation has been obtained from [112] with a possibility to steer parameters for non-minimal Higgs production. The 2HDM Higgs parameters were chosen according to the study described above, $tan\beta = 30$, $M_h + M_A > M_Z$ ($M_A = 90\ GeV$) and equal strength in the coupling of fermions to scalars and pseudoscalars ($\beta - \alpha = 0$). The mass of the light scalar $h$ has been varied between 5 and 30 $GeV$ and the Higgs particle was forced to decay into $\tau^+\tau^-$ pairs to explore this channel in more details. The QCD radiation was simulated within PYTHIA using a combination of the matrix element and parton shower approaches. The Lund string model was chosen as fragmentation scheme.

Although the generated mass range of the Higgs particle $h$ was between 5 and 30 $GeV$, it is sufficient to look at the particular value of $M_h = 20\ GeV$. The strategy is, once again, to try to tag final state $\tau$ leptons using $\tau$ identification technique presented in Chapters 7 and 8. Here, for the light Higgs search, one can expect the same difficulty as in the $\gamma\gamma \to \tau^+\tau^-$ case, namely low transverse momenta of jets associated to the $\tau$ hadronic decays. Because the Higgs boson is produced with very low transverse momentum and it is light, outgoing $\tau$ leptons have low transverse momenta and their hadronic-decay jets even lower (neutrino effect, once more). The final effect would be that large fraction of the potential $\tau$ jets do not pass the $p_T^{jet} > 5\ GeV$ cut which makes the $\tau$ ID method useless. Therefore, it is instructive to use $M_h = 20\ GeV$ where these problems should be suppressed because of the larger Higgs mass. A fact that the Higgs production cross section goes signifficantly down with Higgs mass could be explored, subsequently.

Transverse momenta and pseudorapidities of two $\tau$ leptons comming from decays of $M_h = 20\ GeV$ Higgs boson $h$ calculated at the generator level (before detector unfolding) are shown in Fig. 9.8.

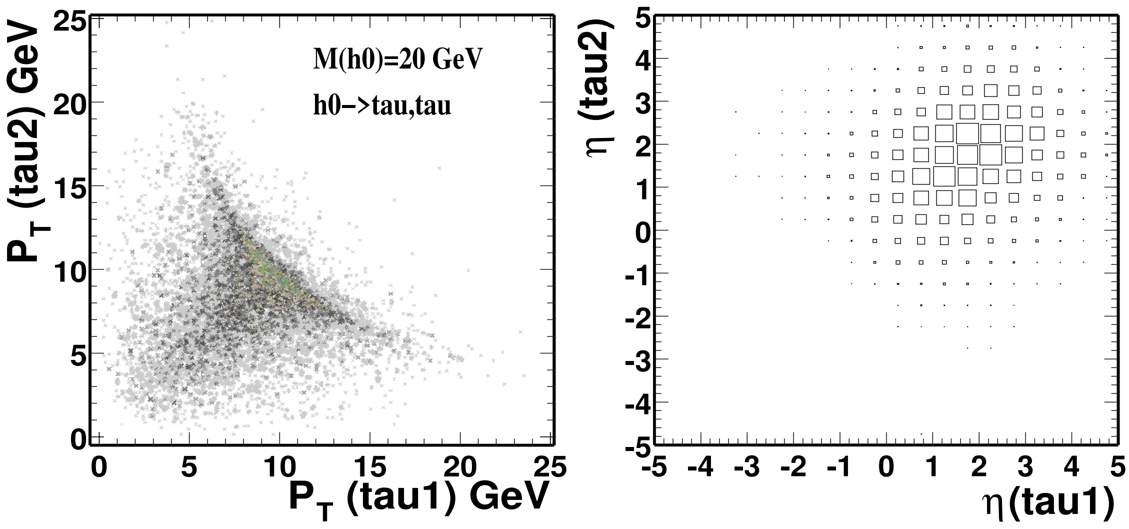


Figure 9.8: The transverse momenta and pseudorapidities of the $\tau^+$ and $\tau^-$ leptons comming from the decay of the $M_h = 20\ GeV$ Higgs particle $h$ obtained from the MC generator before unfolding of the detector effects.

The majority of $\tau$ leptons have transverse momentum $p_T$ well above $5\ GeV$ and they are mostly inside the detector acceptance ($|\eta(\tau)| < 3.0$). After the full detector simulation has been applied the longitudinally invariant $k_T$-clustering algorithm [115, 116] was used to combine the energy depositions in the CAL to particular jets.

Out of the total number of jets found in a considered sample, 68% can be associated to the direction of the MC $\tau$ lepton (distance in $(\eta, \phi)$ plane between jet axis and generated $\tau$ lepton smaller than one unit) and 59% of total number of jets can be associated to hadronically decaying $\tau$ lepton. Assuming Particle Data Group [113] decaying branching ratios of the $\tau$ lepton, 56% of the total number of hadronically decaying $\tau$ leptons can be associated to a corresponding jet and the main source of inefficiency is, again, the $p_T^{jet} > 5\ GeV$ threshold, see Fig. 9.8, combined with the side effects of neutrino presence.

Therefore, as expected, the majority of jets found do come from $\tau$ lepton decays and the remaining number is mostly associated to the activities of the proton remnant. As can be seen in the Fig. 9.9, where $p_T$ and $\eta$ correlations between jet and associated hadronically decaying $\tau$ lepton is shown, the effect of neutrino presence smears the $p_T$ correlations, while the $\eta$ correlation is stronger.

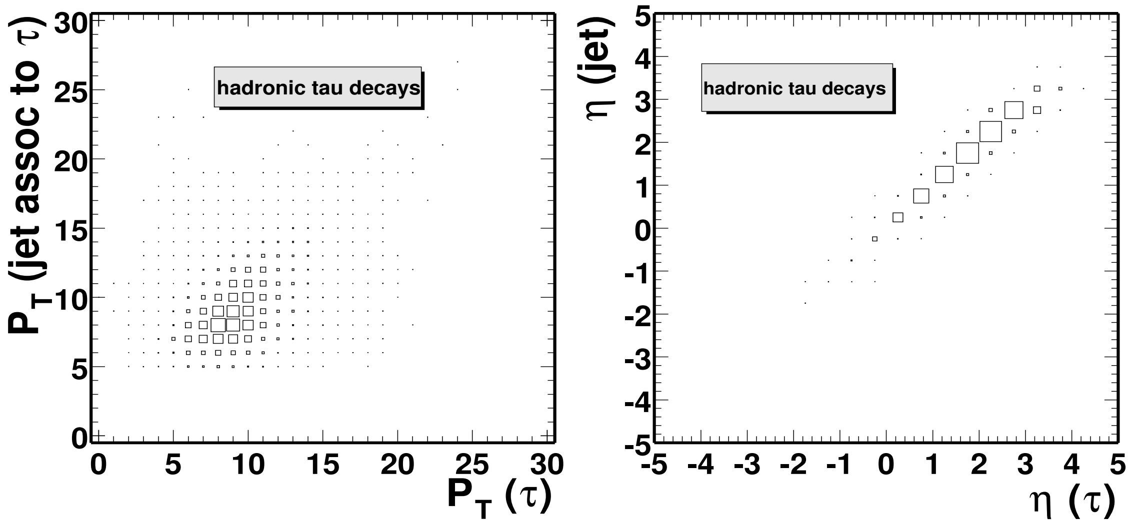


Figure 9.9: $p_T$ and $\eta$ correlations between jet and associated hadronically decaying $\tau$ lepton from $gg \to h \to \tau^+\tau^-$ process ($M_h = 20\ GeV$).

The event topologies considered suggest that the MC simulation was correctly performed. The fact that majority of jets can be attributed to the hadronic decays of $\tau$ particle could be a good basis to use $\tau$ identification method developed for isolated $\tau$ and di-$\tau$ studies.

### 9.3.2 Findings

At the first glance it seems that the $gg \to h \to \tau^+\tau^-$ event topology should not be so different from deep inelastic $\gamma\gamma \to \tau^+\tau^-$. As described in Section 9.2, it could be a signifficant problem to distinguish between these two processes. Therefore, the $\gamma p$ centre of mass rapidity of the $\tau$ lepton pair, $y$, was considered and turned out to be useful differentiating quantity.

However, simulation studies performed point out much bigger and unwanted topological differences between $gg \to h \to \tau^+\tau^-$ and $\gamma\gamma \to \tau^+\tau^-$ processes. In fact, most of the event properties like calorimeter energy and calorimeter transverse energy, $E - p_z$, etc. have fully different shapes. The most showing example is the number of tracks per event for $\gamma\gamma \to \tau^+\tau^-$ and $gg \to h \to \tau^+\tau^-$ shown in Fig. 9.10.

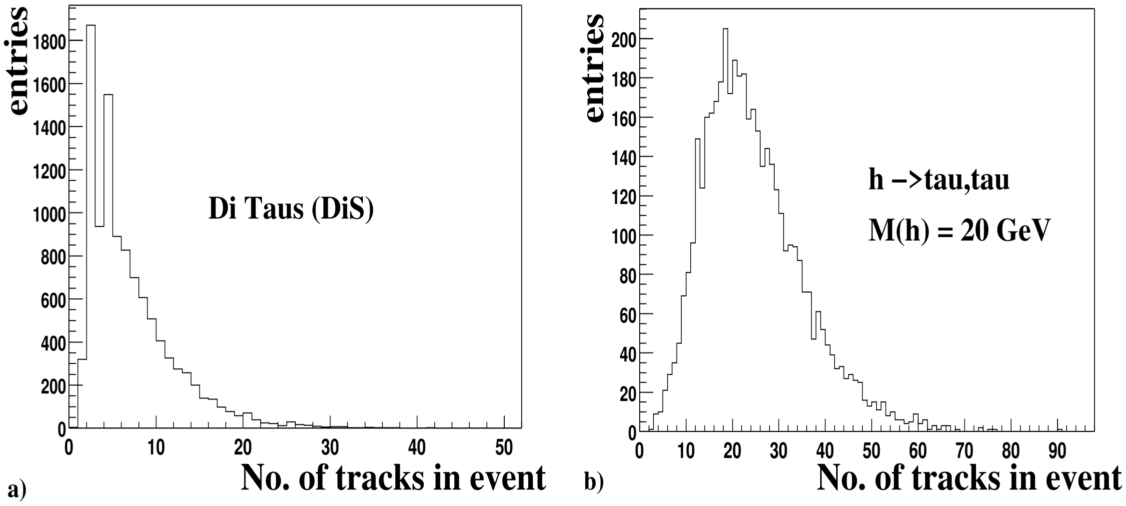


Figure 9.10: Number of tracks per event for a) di-$\tau$ MC (DIS) and b) for light Higgs MC simulation ($M_h = 20\ GeV$).

The plotted shapes are incompatible and it seems that the different physical nature of these type of events plays an important role. Namely, $\gamma\gamma \to \tau^+\tau^-$ is a QED process and the number of tracks per event have clear peaks at 2 and 4 corresponding to the preferred $\tau$ decays into 1 or 3 charged particles. However, $gg \to h \to \tau^+\tau^-$ production is a QCD process which involves a large photon, as well as proton, remnant activity and has all characteristics of, so called, resolved photoproduction processes.

The fact that event topologies are so different in di-$\tau$ and light Higgs cases could be a wanted feature, if $\tau$ jet properties in the light Higgs process would be such that the $\tau$ identification technique can be efficiently applied. Basic jet properties for $gg \to h \to \tau^+\tau^-$ ($M_h = 20\ GeV$) and $\gamma\gamma \to \tau^+\tau^-$ simulated processes are presented in Fig. 9.11. In the light Higgs case only events with two jets were considered and those jets had to be associated with hadronic decays of $\tau$ lepton, i.e. the best possible reconstruction scenario for the $\tau$ discriminant calculation. A track was assigned to a jet, if the distance in $(\eta, \phi)$ plane between track and jet axis was smaller than one unit. The variable -log(rrmean) is a jet-shape variable used for calculation of the discriminant, D, described in Chapter 7.

It is obvious that $\tau$ jet properties of the two processes are completely different. For the light Higgs case jets associated to hadronic $\tau$ decays acquire, ultimately

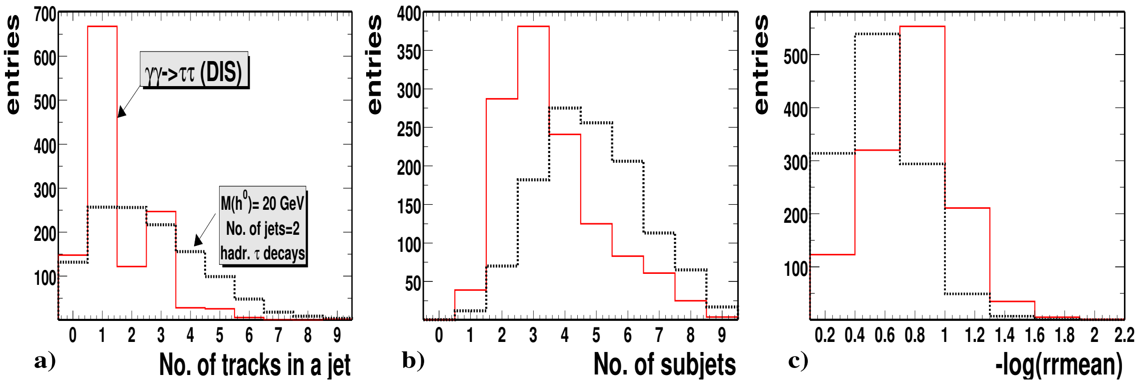


Figure 9.11: Jet properties for $gg \to h \to \tau^+\tau^-$, $M_h = 20$ $GeV$, (dashed line) and for $\gamma\gamma \to \tau^+\tau^-$ process (solid line): a) the number of tracks in a jet, b) the number of subjets and c) discriminant jet-shape variable -log(rrmean). The histogram normalisation was not applied.

unwanted features of standard QCD jets, i.e. they became "background-like" as far as the $\tau$ identification method is concerned.

The discriminant, D, calculated for the process $gg \to h \to \tau^+\tau^-$, $M_h = 20$ $GeV$, $\gamma\gamma \to \tau^+\tau^-$ and photoproduction, is plotted in Fig. 9.12. The discriminat was trained as in the $\gamma\gamma \to \tau^+\tau^-$ study. Signal jets were hadronic $\tau$ decays from di-$\tau$ simulation and photoproduction jets were used as a background sample.

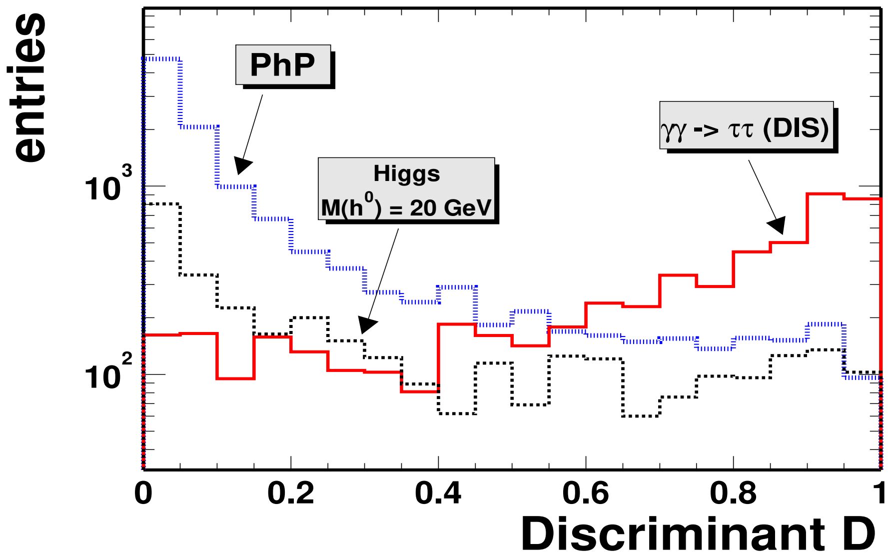


Figure 9.12: The $\tau$ discriminant, D, obtained for the process $gg \to h \to \tau^+\tau^-$, $M_h = 20$ $GeV$, (dashed line), $\gamma\gamma \to \tau^+\tau^-$ (solid line) and photoproduction (dotted line). The histogram normalisation was not applied.

The outcome is extremly unfortunate. The light Higgs discriminant peaks at zero where huge QCD background sits, although the jets considered were matched with simulated $\tau$ lepton direction. The original $\tau$ identification method turned out to be inapplicable for the light Higgs tagging!

An event display [114] of a typical $gg \to h \to \tau^+\tau^-$ simulated event is shown in Fig. 9.13.

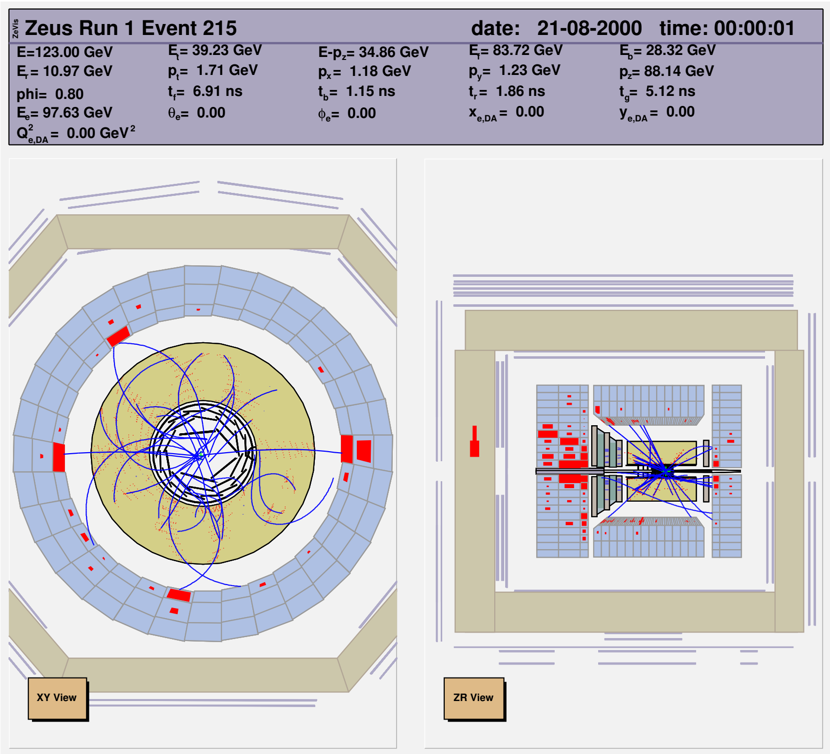


Figure 9.13: Event display of a typical event for $gg \to h \to \tau^+\tau^-$ ($M_h = 20\ GeV$). The energy deposition in the CAL is proportional to the size of shading in the CAL cells. In the $xy$ view, only the energy deposition in the barrel calorimeter is shown. The $xy$ perspective is shown in the so called “fish eye” view, where the most inner parts, i.e. tracking system, is blown up. The most inner part shown in black is, newly installed (2001), the silicon microvertex detector.

In the $xy$ view it is possible to distinguish two horizontal higher transverse momentum tracks associated with the direction of $\tau$ leptons, but there is very strong additional activity which does not come from the decay of Higgs boson. This additional activity comes from the QCD nature of the light Higgs production mechanism. Gluons which fuse into $b$-quark loop, see Fig. 9.5, “repaint” the photon and proton remnants. The only way to preserve final state colour neutrality is that these remnants “talk” to each other via colour flow. The ultimate effect is that this colour cross talk introduces a very large soft final state activity which spoils nominal $\tau$ jet properties and makes $\tau$ identification technique inapplicable.

The $\tau$ ID method, as it was set up for the study presented in this thesis, distinguishes between $\tau$ induced jets and QCD induced jets by exploiting calorimeter energy depositions associated to the jet. This elegant setup works very well when the $\tau$ environment is clean, i.e. for the isolated $\tau$ and di-$\tau$ analysis. However, when the surrounding is not so clean, like in the light Higgs case, the $\tau$ ID setup based just on the jet-shape observables encounters problems. It should be possible to improve the situation by sacrificing elegance for efficiency by including additional event properties in the $\tau$ discriminant calculation, but for the light Higgs case the situation is extremely difficult. Even if it would be possible to have $\tau$ identification efficiencies as in the isolated $\tau$ and di-$\tau$ case, there is still an enormous background problem left. As presented in Chapter 8, even for such a clean process like $\gamma\gamma \rightarrow \tau^+\tau^-$ where both $\tau$ lepton decays contain only one charged hadron, i.e. one track, it is very difficult to suppress the QCD background unless one insists on elastic production mechanism. The light Higgs events considered are not nearly clean as di-$\tau$ ones and they are never produced via an elastic channel, therefore the background problem for hadronic $\tau$ tagging looks prohibiting.

It should be stressed that for the Large Hadron Collider (LHC) the situation could be quite different concerning applicability of the original setup of the $\tau$ identification method. At the LHC, accessible Higgs masses are much larger, hence transverse momenta of an outgoing $\tau^+\tau^-$ pair as well. If the Higgs particle is actually heavy enough, the naive expectation is that larger transverse momenta of outgoing $\tau$ leptons could restore the original power of the $\tau$ ID technique and could make the problem of soft radiation less prominent. It would be very interesting to apply this discrimination technique at LHC surroundings where one expects exactly the conditions for which the technique has been developed.

The situation for possible $\tau$ lepton tagging using leptonic $\tau$ decays for the light Higgs at HERA (again $gg \rightarrow h \rightarrow \tau^+\tau^-$ channel) is hardly any better than the hadronic case described above. A branching ratio that both $\tau$ leptons decay leptonically is 12% and in this case one can expect additional background from semi-leptonic quark decays, meson production and $\gamma\gamma \rightarrow l^+l^-$ processes.

## 9.4 Summary

A study of the perspectives for light Higgs boson search at HERA has been performed using MC simulations. Search perspectives for the channel $gg \rightarrow h \rightarrow \tau^+\tau^-$ are not very promising. The other dominant light Higgs production channel at HERA, Higgs strahlung from the fermion line $\gamma g \rightarrow b\bar{b}h(A)$ is predicted to suffer even more from severe background [13].

An apealing diffractive Higgs production, see Fig. 9.14, would lead to the final state without soft QCD activity and therefore much easier tagging. But, at the HERA accelerator, in contrast to the expectations for LHC, the predicted production cross section is too low to be considered seriously.

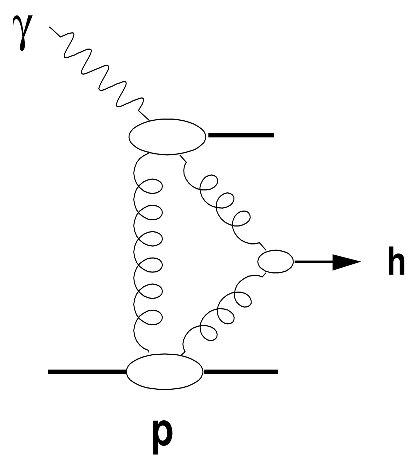


Figure 9.14: Sketch of diffractive Higgs production at HERA.

In adition to the difficulties mentioned above there is an expected problem of triggering light Higgs events, which was not checked in this analysis. Namely, the small mass of the Higgs boson leads to low transverse momentum $\tau$ leptons and therefore predominantly to low $p_T$ final state jets. In fact, the predicted transverse momenta of the final state jets lay in the phase space region where the triggering is difficult and background is large.

Despite obvious obstacles, a search for light Higgs particle at HERA should be more thoroughly examined and studied. As mentioned, as far as theoretical predictions and limitations from other experiments are concerned, search perspectives are substantial and a possible signal would be a reward worth of any effort.

# CHAPTER 10
# SUMMARY

The thesis has presented a generic search for events containing $\tau$ leptons in $e^{\pm}p$ collisions at HERA using the ZEUS detector. A multi-observable discrimination technique was used, exploiting the internal jet structure to discriminate between pencil-like jets coming from hadronic $\tau$ decays and quark- or gluon-induced jets.

A search for events containing isolated $\tau$ leptons, large missing transverse momentum and large hadronic transverse momentum, has been performed using 130 $pb^{-1}$ of integrated luminosity. The search was motivated by results of previous studies in the electron and muon channels performed by the H1 and ZEUS Collaborations. The H1 electron and muon results show an excess in number of observed events comparing to the Standard Model prediction [3], while the ZEUS finding is in agreement with the SM expectation [5]. Three isolated $\tau$ candidates were found, while $0.40^{+0.12}_{-0.13}$ were expected from Standard Model processes, mainly from charged current deep inelastic scattering and single $W^{\pm}$ boson production. A more restrictive selection was applied to isolate $\tau$ leptons in events with large missing transverse momentum produced together with a hadronic final state with high transverse momentum, as expected from the decay of a heavy particle. Two candidate events with transverse momentum of the hadronic system $p_T^{had} > 25\ GeV$ have been observed, while $0.20 \pm 0.05$ events were expected from Standard Model processes. The Poisson probability to observe two or more events, assuming only SM contribution, is 1.8%. Hence a statistical fluctuation cannot be excluded.

Table 10.1 gives the result for the final selection in the $\tau$ channel as well as the results of the previous ZEUS search in the electron and muon channel [5] for two different values of the cut on $p_T^{had}$.

The di-$\tau$ study was performed using an integrated luminosity of 65 $pb^{-1}$ collected in the 1999 to 2000 $e^{+}p$ running period. The results of previous di-muon analyses performed by the H1 and ZEUS Collaborations are in agreement with the SM expectation [7, 8]. In contrast, an H1 analysis of the multi-electron channels showed an excess of events in the large invariant mass region ($M > 100\ GeV$), whereas the ZEUS finding is consistent with the SM [8]. Due to severe background conditions, for the $\tau$ case presented here, the event selection was applied only to isolate elastic di-$\tau$ events suitable for the study of the $\tau$ identification technique and to explore

| ZEUS 1994-2000 $e^{\pm}p$ $\mathcal{L} = 130.1\ pb^{-1}$ | Electron obs./exp. ($W^{\pm}$ contribution) | Muon obs./exp. ($W^{\pm}$ contribution) | Tau obs./exp. ($W^{\pm}$ contribution) |
|---|---|---|---|
| $p_T^{had} > 25\ GeV$ | $2\ /\ 2.90\ ^{+0.59}_{-0.32}$ (45%) | $5\ /\ 2.75\ ^{+0.21}_{-0.21}$ (50%) | $2\ /\ 0.20\ ^{+0.05}_{-0.05}$ (49%) |
| $p_T^{had} > 40\ GeV$ | $0\ /\ 0.94\ ^{+0.11}_{-0.10}$ (61%) | $0\ /\ 0.95\ ^{+0.14}_{-0.10}$ (61%) | $1\ /\ 0.07\ ^{+0.02}_{-0.02}$ (71%) |

Table 10.1: Summary of the results of searches for events with isolated leptons, missing transverse momentum and large $p_T^{had}$. The number of observed events is compared to the SM prediction. The $W^{\pm}$ component is given in parentheses in percent. The statistical and systematic uncertainties added in quadrature are also indicated. The results for the electron and the muon channel were obtained from a previous search [5].

the actual feasibility of tagging $\tau$ pair events at HERA. In a preselection, 14 data events were selected while expected number of di-$\tau$ signal events was $10.38 \pm 0.13$ for an expectation of $1.12 \pm 0.85$ from multi-electron and di-muon production. All selected data events have at least one jet with large $\tau$ disriminant value, $D > 0.80$, associated to the $\tau$ lepton candidate and they are compatible with the $\tau$ hypothesis.

A study of the perspectives for light Higgs boson search at HERA has been performed using MC simulations. The perspectives for a search in the channel $gg \to h \to \tau^+\tau^-$ was found to be not very promising. The original $\tau$ identification method turned out to be inapplicable for the light Higgs tagging, because the QCD nature of the light Higgs $gg \to h \to \tau^+\tau^-$ production mechanism introduces final state activity which spoils the nominal $\tau$ jet properties.

## REFERENCES

[1] Y. Fukuda et al., Phys. Rev. Lett. **81**, 1562 (1998).

[2] Q. R Ahmad et al., Phys. Rev. Lett. **89**, 011301 (2002).

[3] H1 Coll., C. Adloff et al., Eur. Phys. J. **C5**, 575 (1998);

H1 Coll., Paper 824 submitted to the International Europhysics Conference on High Energy Physics, Budapest, Hungary, July 12-18, 2001;

H1 Coll., Paper 1022 submitted to the XXXI International Conference on High Energy Physics, Amsterdam, The Netherlands, July 24-31, 2002;

H1 Coll., Paper 1024 submitted to the XXXI International Conference on High Energy Physics, Amsterdam, The Netherlands, July 24-31, 2002;

H1 Coll., V. Andreev et al., Phys. Lett. **B561**, 241 (2003).

[4] ZEUS Coll., J. Breitweg et al., Phys. Lett. **B471**, 411 (2000).

[5] ZEUS Coll., S. Chekanov et al., Phys. Lett. **B559**, 153 (2003).

[6] ZEUS Coll., S. Chekanov et al., Phys. Lett. **B583**, 41 (2004).

[7] H1 Coll., A. Aktas et al., Phys. Lett. **B583**, 28 (2004).

[8] A. Parenti on behalf of H1 and ZEUS Coll., *Talk given at XI International Workshop on Deep Inelastic Scattering* (Working Group B), St. Petersburg, Russia, April 23-27, 2003., available on `http://www.desy.de/dis03/wgb.html`;

A. Parenti, *Search for Multi-Lepton Events wiht the ZEUS Detector at HERA and VCMVD: An Algorithm for MVD Tracking at TLT*, PhD Thesis, Univ. Degli Stud. di Padova, Padova (Italy), Report DESY-THESIS-2003-038, 2003.

[9] H1 Coll., A. Aktas et al., Eur. Phys. J. **C31**, 17 (2003).

[10] L3, OPAL, ALEPH, DELPHI Coll. and LEP Working Group for Higgs Boson Searches, *Search for the Standard Model Higgs Boson at LEP*, LHWG Note/2002-01, CERN, Geneva, Switzerland, July 2001.

[11] H. E. Haber, G. L. Kane, and T. Sterling, Nucl. Phys. **B161**, 493 (1979);

N. G. Deshpande and E. Ma, Phys. Rev. **D18**, 2574 (1978);

H. Georgi, Hadronic J. **1**, 155 (1978);

J. F. Donoghue and L.-F. Li, Phys. Rev. **D19**, 945 (1979);

L. F. Abbott, P. Sikivie, and M. B. Wise, Phys. Rev. **D21**, 1393 (1980);

B. McWilliams, and L.-F. Li, Nucl. Phys. **B179**, 62 (1981);

J. F. Gunion and H. E. Haber, Nucl. Phys. **B272**, 1 (1986).

[12] M. Krawczyk, Acta Phys. Polon. **B33**, 2621 (2002).

[13] A. C. Bawa and M. Krawczyk, Phys. Lett. **B357**, 637 (1995).

[14] Yu. Dokshitzer, *DGLAP - das unbekannte Wesen. QCD partons and their evolution-basics and subleties. Nonperturbative power corrections* (lectures given at DESY)
`http://www.desy.de/∼acatrain`

[15] J. Nyiri (ed.), *The Gribov Theory of Quark Confinement*, World Scientific, 2001.

[16] H. Abramowicz and A. Caldwell, *HERA Collider Physics*,
Preprint DESY-98-192, 1998.

[17] ZEUS Coll., S. Chekanov et al., Eur. Phys. J. **C27**, 531 (2003);

H1 Coll., C. Adloff et al., Eur. Phys. J. **C14**, 255 (2000).

[18] ZEUS Coll., S. Chekanov et al., Phys. Rev.. **D67**, 012007 (2003).

[19] V. N. Gribov and L. N. Lipatov, Sov. J. Nucl. Phys. **15**, 438 (1972);

G. Altarelli and G. Parisi, Nucl. Phys. **B126**, 298 (1977);

Yu. L. Dokshitzer, Sov. Phys. JETP **46**, 641 (1977).

[20] Y. Balitzki and L. N. Lipatov, Phys. Rev. Lett. **28**, 822 (1978);

E. A. Kuraev, L. N. Lipatov and V. S. Fadin, Phys. Rev. Lett. **44**, 443 (1976); Phys. Rev. Lett. **45**, 199 (1977).

[21] ZEUS Structure Functions and Electroweak Physics working group, Combined H1 and ZEUS results on NC and CC cross sections (unpublished), 2003, available on
`http://www-zeus.desy.de/physics/sfew/PUBLIC/sfew_results/preliminary/eps03/`

[22] ZEUS Coll., S. Chekanov et al., Preprint DESY-03-214, 2003.

[23] ZEUS Coll., U. Holm (ed.), *The ZEUS Detector*. Status Report (unpublished), DESY (1993), available on *http://www-zeus.desy.de/bluebook/bluebook.html*

[24] J. A. Blissett et al., *Development of a tapered cell drift chamber II: Operation of high magnetic fields and different gas pressures*, Nucl. Instr. and Meth. **A245**, 291 (1986).

[25] R. Hall-Wilton et al., *The CTD tracking resolution* (unpublished). ZEUS-99-024, Internal ZEUS-note, 1999.

[26] L. A. T. Bauerdick et al., Nucl. Inst. Meth. **A501**, 340 (2003).

[27] E. Maddox, *A Kalman filter trackfit for the ZEUS microvertex detector* (unpublished) ZEUS-02-001, Internal ZEUS-note, 2002.

[28] J. R. Morais Silva Gonçalo, *Measurement of the High-$Q^2$ Neutral Current Deep Inelastic Scattering Cross Section with the ZEUS Detector at HERA*, PhD Thesis, Univ. of London, London (Great Britain), Report DESY-THESIS-2003-022, 2003.

[29] W. R. Leo, *Techniques for Nuclear and Particle Physics Experiments*, Spring-Verlag, New York, 1997.

[30] D. H. Perkins, *Introduction to High Energy Physics*, Addison-Wesley, 1982.

[31] T. Woeniger, *Influence of Calorimeter Calibration Errors on the Measurements of Deep Inelastic Scattering*, PhD Thesis, Univ. of Hamburg, Hamburg (Germany), 1991;

I. Bohnet, *Investigations on Uniformity, Radiation Resistance and Calibration of ZEUS Calorimeter Components at HERA*, PhD Thesis, Univ. of Hamburg, Hamburg (Germany), Report DESY-THESIS-1999-041, 1999.

[32] C. N. Booth, *Nuclear and Particle Detectors*, available on `http://www.shef.ac.uk/physics/teaching/phy311/`

[33] C. W. Fabjan et al., Nucl. Instr. Meth **141**, 61 (1977);

H. Brückman, U. Behrens and B. Anders, *Hadron Sampling Calorimetry - A Puzzle of Physics*, Preprint DESY-86-155, 1986.

[34] K. Olkiewicz and A. Eskreys, *Off-line Luminosity Calculation in the ZEUS Experiment in 1997, 1998 and 1999* (unpublished).
ZEUS-99-044, Internal ZEUS-note, 1999.

[35] ZEUS Luminosity Group, *Luminosity Measurement in the ZEUS Experiment* (unpublished).
ZEUS-01-004 (rev.), Internal ZEUS-note, 2001.

[36] W. H. Smith et al., Nucl. Instr. Meth. **A335**, 278 (1995).

[37] J. A. Crittenden et al., *The C5 Upgrade* (unpublished).
ZEUS-01-002, Internal ZEUS-note, 2001.

[38] J. A. Crittenden et al., *Results of Analysis of the C5 Detector Time Distributions for the Fall 1992 Running Period* (unpublished).
ZEUS-93-041, Internal ZEUS-note, 1993.

[39] J. A. Crittenden et al., *Analysis of C5 Detector Time Distributions for the 1993 Running Period* (unpublished).
ZEUS-94-041, Internal ZEUS-note, 1994.

[40] G. Gustafson and U. Pettersson, Nucl. Phys. **B306**, 746 (1988).

[41] B. Anderson et al., Phys. Rep. **97**, 31 (1983).

[42] T. Sjöstrand, Comp. Phys. Comm. **39**, 347 (1986);
T. Sjöstrand and M. Bengtsson, Comp. Phys. Comm. **43**, 367 (1987);
T. Sjöstrand, Comp. Phys. Comm. **82**, 74 (1994).

[43] B. R. Webber, Nucl. Phys. **B238**, 492 (1984).

[44] D. Amati and G. Veneziano, Phys. Lett. **B83**, 87 (1979);
A. Bassetto, M. Ciafaloni and G. Marchesini, Phys. Lett. **B83** 207 (1979);
G. Marchesini, L. Trentadue and G. Veneziano, Nucl. Phys. **B181** 335 (1980).

[45] R. D. Field and S. Wolfram, Nucl. Phys. **B213**, 65 (1983).

[46] G. Marchesini et al., Comp. Phys. Comm. **67**, 465 (1992).

[47] H. L. Lai et al., Phys. Rev. **D55**, 1280 (1997).

[48] M. Glück, E. Reya and A. Vogt, Phys. Rev. **D46**, 1973 (1992).

[49] G. A. Schuler and H. Spiesberger, *Proc. Workshop on Physics at HERA*, W. Buchmüller and G. Ingelman (eds.), Vol. 3, p. 1419, DESY, Hamburg, Germany, (1991).

[50] A. Kwiatkowski, H. Spiesberger and H.-J. Möhring, Comp. Phys. Comm. **69**, 155 (1992).

[51] G. Ingelman, A. Edin and J. Rathsman, Comp. Phys. Comm. **101**, 108 (1997).

[52] CTEQ Coll., H. L. Lai et al., Eur. Phys. J. **C12**, 375 (2000).

[53] L. Lönnblad, Comp. Phys. Comm. **71**, 15 (1992).

[54] M. Goosens et al., GEANT 3.21, CERN, Geneva, Switzerland, (1994).

[55] G. F. Hartner, *VCTRAK Briefing: Program and Math* (unpublished). ZEUS-98-058, Internal ZEUS-note, 1998.

[56] ZEUS Coll., J. Breitweg et al., Z. Phys. **C74**, 207 (1997).

[57] H. Abramowicz et al., Nucl. Instr. and Meth. **A365**, 508, (1995); R. Sinkus et al., Nucl. Instr. and Meth. **A391**, 360, (1997);

[58] O. Gonzalez, *Precise Determinations of the Strong Coupling Constant at HERA.*, PhD Thesis, Univ. of Madrid, Madrid (Spain), Report DESY-THESIS-2002-020, 2002.

[59] O. Gonzalez, H. Raach and J. Terron, *Measurements of the inclusive jet cross sections in NC DIS in the Breit Frame* (unpublished). ZEUS-02-007, Internal ZEUS-note, 2002.

[60] M. L. Vazquez Acosta, *Jet Production in Charged Current Deep Inelastic Scattering at HERA*, PhD Thesis, Univ. of Madrid, Madrid (Spain), Report DESY-THESIS-2003-006, 2003.

[61] T. Han, R. D. Peccei and X. Zhang, Nucl. Phys. **B454**, 527 (1995); V. F. Obraztsov, S. R. Slabospitsky and O. P. Yushchenko, Phys. Lett. **B426**, 393 (1998); T. Han et al., Phys. Rev. **B426**, 073008 (1998);

T. Han and J. L. Hewett, Phys. Rev. **D60**, 074015 (1999);

H. Fritzsch and D. Holtmannspotter, Phys. Lett. **B457**, 186 (1999).

[62] H. J. Kim and S. Kartik, Preprint LSUHE-145-1993, 1993.

[63] K. Hagiwara, S. Komamiya and D. Zeppenfeld, Z. Phys. **C29**, 115 (1985)

[64] J. Butterworth and H. Dreiner, Nucl. Phys. **B397**, 3 (1993);

T. Kon and T. Kobayashi, Phys. Lett. **B270**, 81 (1991);

W. Porod, Phys. Rev. **D59**, 095009 (1999).

[65] U. Baur, J. A. M. Vermaseren and D. Zeppenfeld, Nucl. Phys. **B375**, 3 (1992).

[66] C. Diaconu, *Isolated Lepton Production at Colliders*, Preprint DESY-04-006, 2004.

[67] C. Diaconu, *Parton showers effects for W production at HERA*, Prepared for Workshop on Monte Carlo Generators for HERA Physics, DESY, Hamburg, Germany, (1998).

[68] K.-P. O. Diener, C. Schwanenberger and M. Spira, Eur. Phys. J. **C25**, 405 (2002).

[69] K.-P. O. Diener, C. Schwanenberger and M. Spira, *Photoproduction of W bosons at HERA: reweighting method for implementing QCD corrections in Monte Carlo programs*; Preprint hep-ex/0302040, 2003.

[70] P. Nason, R. Rückl and M. Spira, J. Phys. **G25**, 1434 (1999);

M. Spira, Preprint DESY-99-060 (hep-ph/9905469), 1999.

[71] D. Dannheim, *Search for events with isolated leptons and large missing transverse momentum in ep collisions at HERA*, PhD Thesis, Univ. of Hamburg, Hamburg (Germany), Report DESY-THESIS-2003-025, 2003.

[72] S. Jadach, Z. Was and J. H. Kuehn, Comp. Phys. Comm. **64**, 275 (1991).

[73] G. Schuler, Nucl. Phys. **B299**, 21 (1988);

U. Baur and J. J. van der Bij, Nucl. Phys. **B304**, 451 (1988);

J. J. van der Bij and G. J. van Oldenborgh, Z. Phys. **C51**, 477 (1991).

[74] T. Stelzer, Z. Sullivan and S. Willenbrock, Phys. Rev. **D56**, 5919 (1997);

S. Moretti and K. Odagiri, Phys. Rev. **D57**, 3040 (1998).

[75] M. L. Pearl et al., Phys. Lett. **B63**, 466 (1976);

M. L. Pearl et al., Phys. Rev. Lett. **35**, 1489 (1985);

[76] T. Carli and B. Koblitz, Adv. Comp. Analysis Techniques in Phys. Research (Batavia, USA, 2000), P. Bath and M. Kasemann, Eds., pp 110, also in hep-ph/0011224, 2000;

T. Carli and B. Koblitz, Nucl. Inst. Meth. **A501**, 576 (2003), also in hep-ex/0211019, 2002.

[77] C. N. Nguyen, Diploma Thesis, *Identification of $\tau$ Leptons from Single $W \rightarrow \tau\nu_\tau$ Production with the ZEUS Detector*, Universität Hamburg, Hamburg (Germany), Report DESY-THESIS-2002-024, 2002.

[78] B. Koblitz, *Search for Instanton-Induced Processes with the H1 Detector in Deep-Inelastic-Scattering Electron-Proton Collisions at HERA*, PhD Thesis, Universität Hamburg, Hamburg (Germany), Report DESY-THESIS-2002-015, 2002.

[79] ZEUS Coll., S. Chekanov et al., Phys. Lett. **B539**, 197 (2002).

[80] J. Edmonds, J. Grosse-Knetter and A. Quadt, *Neutral Current Cross Section at High $Q^2$* (unpublished).
ZEUS-99-016, Internal ZEUS-note, 1999.

[81] M. Moritz., Ph.D. Thesis, *Measurement of the High $Q^2$ Neutral Current DIS Cross Section at HERA*, Universität Hamburg, Hamburg (Germany), Report DESY-THESIS-2002-009, 2002.

[82] ZEUS Coll., J. Breitweg et al., Eur. Phys. J. **C11**, 427 (1999).

[83] J. Agrawal, P. H. Frampton and D. Ng, Nucl. Phys. **B386**, 267 (1992);

E. Accomando and S. Petrarca, Phys. Lett. **B323**, 212 (1994);

E. Accomando, M. Iori and M. Mattioli, Preprint hep-ph/9505274, 1995.

[84] N. Arteaga-Romero, C. Carimalo and P. Kessler, Z. Phys. **C52**, 289 (1991);

[85] B. Leisner., Ph.D. Thesis, *Muon Pair Production in Electron-Proton Collisions*, I. Phys. Institut RWTH Aachen, Aachen (Germany), Report DESY-THESIS-2002-049, 2002.

[86] G. Barbiellini et al., Phys. Rev. Lett. **32**, 385 (1974).

[87] T. Abe, Comp. Phys. Comm. **136**, 126 (2001); Preprint hep-ph/0012029, 2000.

[88] T. Ishikawa, T. Kaneko, K. Kato, S. Kawabata, Y. Shimizu and H. Tanaka, KEK Report 92-19, 1993.

[89] F. W. Brasse et al., Nucl. Phys. **B110**, 413 (1976).

[90] A. Mücke, R. Engel, J. P. Rachen, R. J. Protheroe and T. Stanev, Comp. Phys. Comm. **124**, 290 (2000).

[91] H. Abramowicz, A. Levy, Preprint hep-ph/9712415, 1997.

[92] J. Fujimoto, M. Igarashi, M. Nakazawa, Y. Shimizu and K. Tobimatsu, Prog. Theor. Phys. Suppl. **100**, 285 (1990).

[93] K. J. F. Gaemers, R. M. Godbole and M. van der Horst, *Proc. Workshop on Physics at HERA*, DESY, Hamburg, Germany, (1987).

[94] J. F. Gunion et al., *Higgs Hunter's Guide*, Addison-Wesley Publ. Comp., 1990.

[95] ALEPH, DELPHI, L3, OPAL Collaborations and the LEP working group for Higgs boson searches, CERN-EP/2000-055, 28 (2000).

[96] A. C. Bawa and M. Krawczyk, Phys. Lett. **B357**, 637 (1995).

[97] Muon g-2 Coll., G. W. Bennett et al., Phys. Rev. Lett. **89**, 101804 (2002); Erratum-ibid. **89**, 129903 (2002).

[98] OPAL Coll., G. Abbiendi, Eur. Phys. J. **C23**, 397 (2002);

DELPHI Coll., DELPHI 2002-037-CONF-571, submitted to ICHEP02 (preliminary), (2002);

ALEPH Coll., PA13-027, submitted to ICHEP96 (preliminary), (1996).

[99] M. Krawczyk et al., Eur. Phys. J. **C8**, 495 (1999);

P. H. Chankowski et al., Eur. Phys. J. **C11**, 661 (1999);

P. H. Chankowski et al., Phys. Lett. **B496**, 195 (2000).

[100] S. M. Keh, *Tau physics with the Crystal Ball Detector*, DESY F31-86-6, (1986).

[101] M. Narain, *Inclusive Photon Spektra from* $\Upsilon$ *Decays*, PhD Thesis, Report UMI-92-05244, 1991.

[102] J. Lee-Franzini, Proc. of ICHEP88, 1432, 1988.

[103] M. Krawczyk and J. Żochowski, Phys. Rev. **D55**, 6968 (1997).

[104] M. Roco (CDF and D0 Coll.), FERMILAB-CONF-00-203-E (2000).

[105] K. J. F. Gaemers et al., in Proc. of the HERA Workshop, R. D. Peccei (ed.), **Vol. 2**, 739, Hamburg, Germany, October 1987.

[106] B. Grządkowski et al., Phys. Lett. **B272**, 174 (1991).

[107] A. C. Bawa and M. Krawczyk, Warsaw University IFT preprints 16/91 (and erratum) and 16/92, (1992);

A. C. Bawa and M. Krawczyk, in Proc. of XVI Kazimierz Meeting, 83, Poland, May 1993.

[108] P. Gambino and M. Misiak, Nucl. Phys. **B611**, 338 (2001).

[109] ALEPH Coll., D. Buskulic et al., Z. Phys. **C62**, 539 (1994);

DELPHI Coll., P. Abreu et al., Nucl. Phys. **B418**, 403 (1994);

L3 Coll., M. Acciarri et al., Z. Phys. **C62**, 551 (1994);

OPAL Coll., R. Akers et al., Z. Phys. **C61**, 19 (1994).

[110] A. I. Vainstein et al., Sov. Phys. Usp., **23**, 429 (1980).

[111] T. Sjöstrand, Comp. Phys. Comm. **135**, 238 (2001).

[112] E. Eichten, I. Hinchliffe, K. Lane and C. Quigg, Rev. Mod. Phys **56**, 579 (1984); Rev. Mod. Phys **58**, 1065 (1985)

[113] Particle Data Group, D. E. Groom et al., Eur. Phys. J. **C15**, (2000).

[114] O. Kind et al., Talk given at 2003 Conference for Computing in High-Energy and Nuclear Physics (CHEP 03), La Jolla, California, March 24-28, 2003; Preprint hep-ex/0305095, 2003.

[115] S. Catani et al., Nucl. Phys. **B406**, 187 (1993).

[116] S. D. Ellis and D. E. Soper, Phys. Rev. **D48**, 3160 (1993).

[117] J. E. Huth et al., *Research Directions for the Decade. Proceedings of Summer Study on High Energy Physics*, 1990, E. L. Berger (ed.), pp 134, World Scientific (1992).
Also in preprint FERMILAB-CONF-90-249-E.

[118] J. R. Forshaw and M. H. Seymour, JHEP **9909**, 009 (1999).

[119] M. H. Seymour, Nucl. Phys. **B 421**, 545 (1994).

[120] ZEUS Coll., S. Chekanov et al., Phys. Lett. **B558**, 41 (2003).